Title
Multiscale Raman Spectroscopy for Liquid Biopsy Cancer Diagnostics

Permalink
https://escholarship.org/uc/item/04m5g8jf

Author
Koster, Hanna J.

Publication Date
2022

Peer reviewed|Thesis/dissertation

Multiscale Raman Spectroscopy for Liquid Biopsy Cancer Diagnostics

By

HANNA KOSTER
DISSERTATION

Submitted in partial satisfaction of the requirements for the degree of

DOCTOR OF PHILOSOPHY

in

Biomedical Engineering

in the

OFFICE OF GRADUATE STUDIES

of the

UNIVERSITY OF CALIFORNIA

DAVIS

Approved:

_____

Randy P. Carney, Chair

_____

Erkin Şeker

_____

Sanjeevi Sivasankar

_____

Maria Navas-Moreno

Committee in Charge

2022

i

Acknowledgments

I would like to first thank my committee members for their continuous support as I progressed through my work these past four years. I appreciate your guidance and am grateful to be surrounded by such inspiring and impactful scientists. I would additionally like to say thank you to the BME department as a whole, I immediately felt welcomed and at home when I started the program and have made so many memories during my time here.

I would like to give a huge shout-out to my parents, without you both I truly would not be where I am today. Mom, thank you for teaching me to pursue what I want and not let anyone—especially men—tell me I can't do it. That advice has been instrumental in my successes and will continue to help me promote myself in the future. Dad, thank you for teaching me to always be willing to help those in need. Often times people are more than happy to return the favor! The worst part of my program has been being so far away from both of you, but I feel your love all the way out here.

Thank you to my friends for having countless adventures with me and always being my support system. Grad school is challenging but it's definitely easier when you have good people in your corner. Hannah O., Rachel, Victor, Tatu, Neona, and Bryan, thank you for making our lab an incredibly happy and fun place to spend time. Not everyone gets to experience liking their lab mates as much as I do, and I consider myself very fortunate to have all of you. Leora, Abby, Zoe, and Hannah J., you are some of the best people I know, and I can't wait to keep celebrating all our accomplishments as we continue to grow!

To Elliot, not a day goes by where I don't think about you. No one can get my ugly laugh out as easy as you did. You were truly one of my best friends and I miss you dearly. Sometimes when I have a bad day, I think about all the fun times we had together, and my day seems to get much brighter. I will see you again one day, and I can't wait to catch up with you.

Joshua, you deserve your own page of acknowledgments, but I'll keep it short and sweet. Thank you for being my rock, my best friend, and my partner in crime. Thank you for always reminding me how capable I am and making me laugh whenever I start overthinking (which is like, every day). I can't imagine my life without, nor do I care to find out what it would be like.

Lastly, I want to say thank you to Randy. Thank you for taking a chance on me, even after I wrote my personal statement to grad school about wanting to be a lumberjack. Thank you for trusting me to help get the lab up and running and allowing me to develop skills not many graduate students get to. Thank you for always being willing to meet and give me feedback, even if it was while passing each other in the hallway. You are an incredible mentor and I feel very fortunate to be your mentee. With your support I was able to accomplish some hefty goals during my time at Davis, and it is the foundation on which I will build the rest of my professional life. You are more than an advisor to me; you are a true friend.

Table of Contents

List of Figures

Abstract

For more effective early-stage cancer diagnostics, there is a need to develop sensitive and specific, non- or minimally invasive, and cost-effective methods for identifying circulating tumor-associated biomolecules, including extracellular vesicles (EVs). As a rapid, label-free, non-destructive analytical measurement requiring little to no sample preparation, Raman spectroscopy shows great promise for liquid biopsy cancer detection and diagnosis. While many studies have demonstrated the promise of Raman spectroscopy to provide value for clinical diagnostics, the sensitivity and specificity of such platforms typically drops when applied to larger patient cohorts. Additionally, Raman can suffer from low signal due to the number of inelastically scattered photons (~1 in a million) produced after a sample is interrogated with a laser. Surface enhanced Raman scattering (SERS) is a powerful extension of this technique, providing orders of magnitude increase in chemical sensitivity compared to spontaneous Raman scattering. Yet it remains a challenge to synthesize robust, uniform SERS substrates quickly and easily. Raman technology has not been successfully moved into the clinic and is hindered by the need to develop more miniaturized and automated systems that are integrated with inexpensive and useful SERS materials. Thus, the objective of this dissertation work is three-fold: 1) to carry out experiments on large clinical datasets to validate Raman and SERS diagnostics; 2) to examine the value of spectroscopic analysis of EVs; and 3) to develop novel SERS materials that are robust, biocompatible, and inexpensive.

To address these objectives, we carried out Raman analysis of plasma, serum, and saliva from hundreds of cancer patients and benign controls (from patients undergoing similar procedures or screenings without cancer), including patients diagnosed with head and neck, ovarian, and endometrial cancers. Several notable findings were reported arising from this analysis, ranging from optimization of Raman data collection and data analysis, discovery and application of new plasmonic materials, and applied clinical testing of EVs.

First, we showed that a simple data augmentation routine of fusing plasma and saliva spectra provided significantly higher clinical value than either biofluid alone, pushing forward the potential of clinical translation of Raman spectroscopy for liquid biopsy cancer diagnostics.

Next, we reported the utilization of a simple plasmonic scaffold composed of a microscale biosilicate substrate embedded with silver nanoparticles for SERS analysis of ovarian and endometrial cancer EVs. We observed a major loss of sensitivity for ovarian and endometrial cancer following enzymatic cleavage of EVs' extraluminal domain, suggesting its critical significance for diagnostic platforms. Using SERS, we also confirmed that three common EV isolation methods (differential ultracentrifugation, density gradient ultracentrifugation, and size exclusion chromatography) yield variable lipoprotein content. However, in combining SERS analysis with machine learning assisted classification, we showed that the disease state is the main driver of distinction between EV samples, and largely unaffected by choice of isolation.

Finally, we demonstrated the synthesis and characterization of a new homogeneous gold nanofoam (AuNF) substrate produced by a rapid, one-pot, four-ingredient synthetic approach. These novel AuNFs were rapidly nucleated with macroscale porosity and then chemically roughened to produce nanoscale features that confer homogeneous and high signal enhancement ($\sim 10^{9}$) across large areas, a comparable performance to lithographically produced substrates, with high utility for application in low-resource settings

The work presented below comprehensively shows the promise of Raman as a clinical diagnostic tool and takes measured steps toward validating the technology in the context of cancer disease states. The technique has high disease discrimination in whole biofluids and isolated EV populations, and the addition of novel nanomaterials increases the sensitivity and specificity to reach clinically necessary levels. This work is foundational in promoting the continued emphasis on translating Raman to be a clinically relevant diagnostic tool.

Chapter 1: Background and Significance

1.1 Current methods of cancer diagnostics are lagging and could be significantly improved

There is a strong correlation between the stage at diagnosis and patient outcomes. For example, in head and neck cancers (HNC) 60-70% of cases are diagnosed in stage III or IV with 5-year overall survival rates of <50%.[1] Further, these late-stage diagnoses are associated with distant metastasis and a high risk of recurrence.[2] Cases caught in stage I and II are typically treatable with surgery or radiotherapy alone, increasing survival rates to 70-90%.[1] Typical HNC diagnostic methods rely on presentation of physical symptoms such as lumps in the neck, sores in the mouth and throat that are slow to heal, and difficulty swallowing which hinders the ability to catch the cancer in the early stages.[3]

An even more urgent case for development of early-stage cancer diagnostic techniques is ovarian cancer (OvCa). Early-stage diagnosis of OvCa amounts to a 5-year survival rate of over 90%; however this rate decreases dramatically to 29% for those with a late stage diagnosis.[4,5] Typical signs of the disease include symptoms of pelvic or abdominal pain, frequent urination, indigestion, and vaginal bleeding,[5] all of which are symptoms associated with less severe female ailments as well, making them easier to overlook. The lack of specific indicators leads to poor early-stage detection and subsequent poor prognosis outlooks. These two cancer groups highlight the urgent need to develop a highly sensitive method of detecting the presence of cancer at an early stage, leading to better patient outcomes and reduced financial burden.

Typical diagnostic methods include a multitude of approaches employed by physicians. The first and most straightforward of these is a physical examination in which a doctor would look for lumps or visual abnormalities. Some cancers, such as leukemia or prostate cancer, have a common blood test that patients can submit to for confirmation of the disease presence.[6] Imaging methods

such as computerized tomography (CT), magnetic resonance imaging (MRI) and positron emission tomography (PET) are commonly used tools but have their own disadvantages. The equipment requires a large physical footprint, the tests and equipment are expensive, and the patient often must remain in a confined area for a long amount of time. Further, specialized training on the instruments is necessary for proper diagnostic readout. Lastly, a biopsy or fine needle aspirate combined with histopathological staining is perhaps the most common and conclusive way to diagnosis cancer.[7] These methods are time consuming, invasive, often suffer inter-reader error, and require a high level of specialized training to determine the disease presence and staging. To overcome these issues, an ideal diagnostic test would be fast, non-invasive, highly sensitive, minimally or wholly non-invasive, and easy to readout.

Of particular interest is the development of a liquid biopsy diagnostic test that can be performed using patient biofluids such as plasma or saliva. This would immensely reduce the invasiveness of the procedure and lessen the associated complications. Much work has been done in the realm of biomarker discovery and diagnostic association using patient biofluids. For example, enzyme-linked immunosorbent assays (ELISAs) have been developed to test for specific cancer markers, even in the context of OvCa in which clinicians can order an ELISA to analyze the level of carbohydrate antigen 125 (CA125) present in the bloodstream.[8] Although ELISA methods can be highly sensitive, they require a long run time, need specific antibodies for accurate result readout, and have a high possibility of false positives or negatives.[9] Other options for biomarker testing include Western Blot (WB) and mass spectrometry (MS), but these approaches are expensive, slow, complex, and low throughput making them hard to scale for clinically relevant cancer detection. Genomic cell free DNA testing can also be utilized for multi-cancer testing abilities and although it produces promising results, the DNA is found in very low levels and degrades quickly, meaning tests must be performed within hours of isolation.[10]

Optical techniques show great promise to address some of these weaknesses. They are fast, non-destructive, can probe a wide variety of biomolecules, and do not require physical contact with the sample. They are also highly compatible to use in the context of liquid biopsies. Optical equipment can be integrated to form and develop probing platforms to aid in the identification and subsequent readout of chemical signatures. These signatures can be used to inform physicians of the disease state, providing useful information while remaining non-invasive and requiring only small amount of patient biofluid.

1.2 Raman spectroscopy is an attractive option as a liquid biopsy tool

Vibrational spectroscopy is a group of optical techniques that non-specifically interrogate complex molecular systems, providing a chemical fingerprint related to the rotational and vibrational modes of the probed molecules. There are two main vibrational spectroscopy techniques, infrared (IR) spectroscopy and Raman spectroscopy. While IR spectroscopy is much more common, and yields robust chemical fingerprinting, it is largely not amenable to biological systems, due to the strong absorption in the IR by water. Instead, Raman spectroscopy provides strong value to chemically fingerprint biological systems.

This inelastic scattering phenomenon was discovered in 1928 by Indian scientist C.V. Raman and labelled as a type of secondary radiation.[11] While the majority of photons that interact with a sample are Rayleigh or elastically scattered, there is occasionally (~1 in 10^6 or fewer) photons that are Raman, or inelastically, scattered, meaning it has a net gain or net loss of energy compared to incident frequency. This energy change occurs in the vibrational levels of a molecule and produces a Stokes (lower energy) or anti-Stokes (higher energy) shift that can be translated and read as a Raman spectrum with discrete peaks (**Figure 1.1**). In each case, one quantum of energy is gained or lost, and the Stokes and anti-Stokes lines are equally shifted from the Rayleigh line (i.e. the wavelength of the interrogation laser).[12] However, the Stokes lines have higher intensity due to more molecules residing in the

ground state than in excited vibrational states and thus the majority of Raman measurements specifically examine the Stoke shifts.[12]
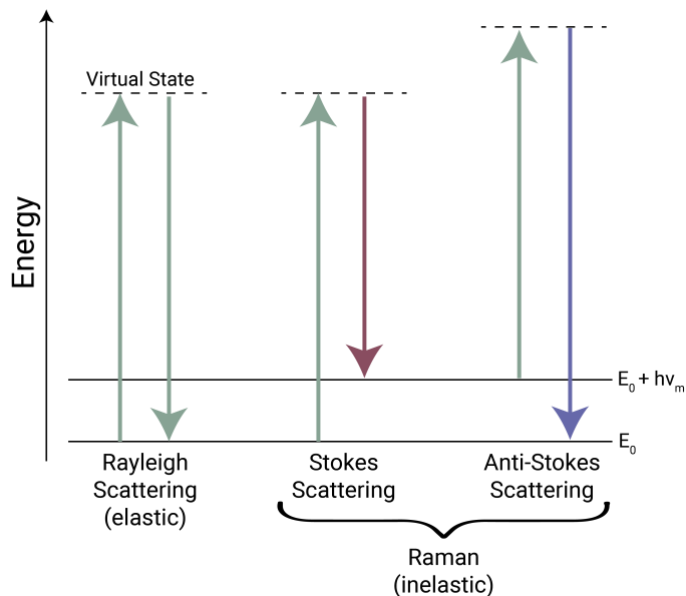
Figure 1.1: Jablonski diagram for elastic (Rayleigh) and inelastic (Raman) photons after they interact with a sample. Both Stokes scattering and anti-Stokes processes are highlighted in the Raman section, showing the two distinct vibrational shifts that can occur.

Molecules are determined to be Raman active based on their polarizability that in turn is dependent on the molecular geometry. When molecules undergo an electron cloud deformation, electrons are pulled away from nuclei, inducing a dipole moment and producing a Raman scattered photon. Not all vibrational modes within a molecule are Raman active; for example, the symmetric stretching mode in carbon dioxide (CO_2) results in a polarization, as the molecule stretches and compresses, making it Raman active. Conversely, the asymmetric stretching and bending modes result in no net polarizability change during the stretch/bend and are thus not Raman active (**Figure 1.2**). Capture and detection of the inelastically scattered Raman photons can provide a spectral readout of functional groups and a compositional overview of the sample being probed. The distinct peaks in the Raman spectrum are ubiquitous (i.e. a peak at 1450 cm^{-1} always corresponds to the same thing) and

can be analyzed to determine different macromolecules including proteins, lipids, nucleic acids, and carbohydrates present.
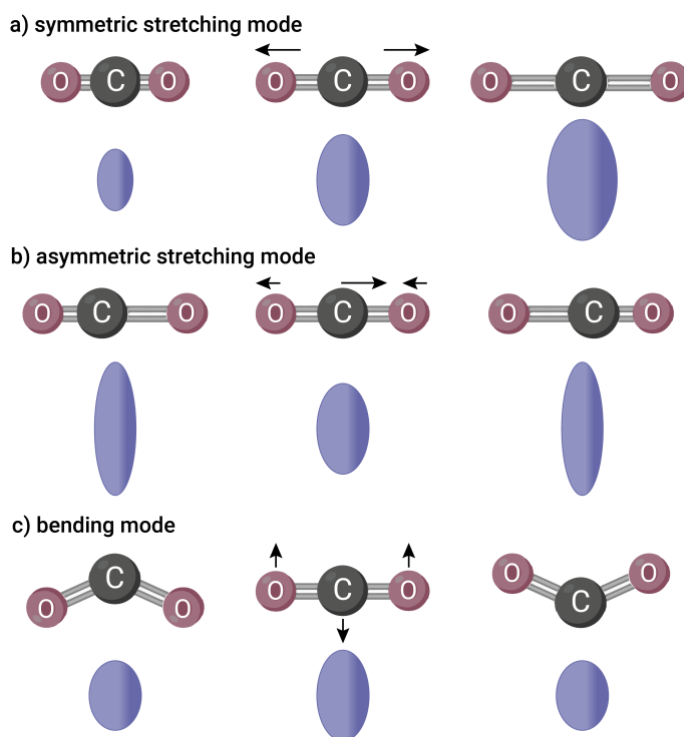
Figure 2.2: Changes in the polarizability of carbon dioxide during its vibrations. a) The symmetric stretching mode produces a net polarizability change, making it Raman active. b) The asymmetric stretching mode results in the same shape and both ends of the movement, making it not Raman active. c) The bending mode results in the same shape and both ends of the movement, making it not Raman active.

Raman spectroscopy is high in specificity and sensitivity, non-destructive, label free, suitable for aqueous measurements, and requires minimal sample preparation and volumes.[13] These advantages highlight the potential for Raman in clinical use, replacing the time consuming, expensive, and low-throughput technologies currently used. The biggest disadvantage of Raman stems from the inherent low volume of inelastically scattered photons. This can be mitigated via longer optical acquisition times but this in turn can reduce the viability of the technique for clinical translation. Another way of overcoming this inherent weakness is by integrating nanosized metallic components, an extension of the technique that is called surface-enhanced Raman scattering.

1.3 Surface-enhanced Raman scattering can overcome associated technique weakness

Surface-enhanced Raman scattering (SERS) is a powerful phenomenon discovered by M. Fleischmann in 1974 while he was conducting experiments of pyridine adsorption on a silver electrode.[14] They reported an incredible million-fold enhancement of the Raman signal which they attributed to the increase in surface area from roughing the silver electrode.[14] A study produced by Jeanmaire and Van Duyne in 1977 realized that the increased surface area was not the key reason for the intense signal enhancement.[15] Both groups continued to independently work on the topic and SERS is now universally accepted as a surface analytical technique that can reach even single molecule sensitivity.

The mechanism by which SERS produces this highly enhanced signal is still under debate, but there are two well-accepted theories that may both play a part. The dominant contributor to this process comes from electromagnetic enhancement resulting from localized surface plasmon resonances (LSPRs) as the light interacting with the molecules is amplified.[16] In this theory, as the
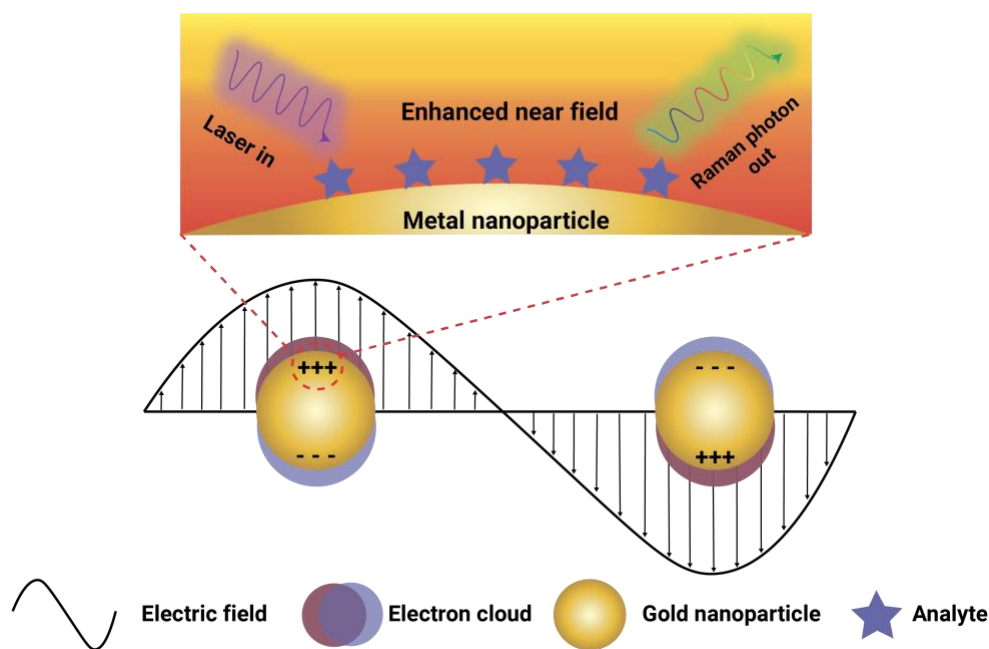
Figure 3.3: Schematic of the electromagnetic enhancement effect giving rise to SERS enhancement. As light hits the metal nanoparticles, the conduction electrons oscillate and create a strong local electronic field. Analytes within a short distance (~10nm) of the metal surface are enhanced and their chemical fingerprint can be collected and readout.

light propagates along the surface of the metal, the conduction electrons start to oscillate and in turn generate a surface plasmon that amplifies the incident laser field and enhances the Raman signal (**Figure 1.3**).[17] A high concentration of this enhancement happens in small distances between nanoscale plasmonic materials, typically in the location of gaps or sharp features.

Coinage metals including gold, silver, and copper are commonly used as plasmonic materials and are outfitted with a wide range of nanoscale features where the electromagnetic enhancement can occur.[18] These types of noble metals are ideal to use as SERS materials due to their optical and electronic properties as well as their ability to produce LSPR bands in both the ultraviolet and visible region of the electromagnetic spectrum.[16] Of the coinage metals, both silver (Ag) and gold (Au) have been applied widely to SERS-based biological studies.[19–23] Typical lab setups employ laser wavelengths that fall within the near infrared (NIR) region, making the metals essentially interchangeable as they exhibit similar behavior, which can be shown by assessing their dielectric functions.[16] Ag and Au have similar electronic densities as visualized by the real parts of their dielectric functions in **Figure 1.4**. Although the behavior of these two metals is highly comparable, there are some advantages of using Au over Ag for biological applications. Au surfaces tend to have greater chemical stability as well as increased biocompatibility with many molecules of interest.[16] In
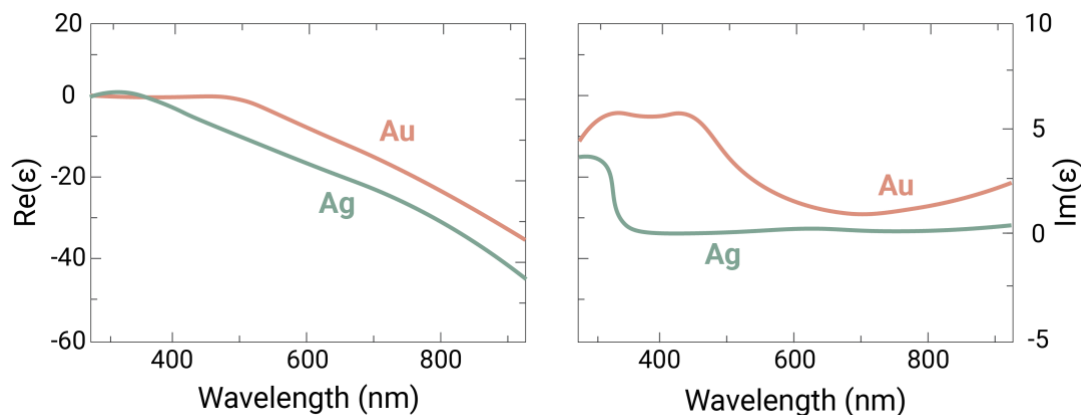
Figure 4.4: Dielectric functions of gold (Au) and silver (Ag) for both the real (left graph) and imaginary (right graph) parts. Both metals behave similarly in the NIR region, making them attractive materials for SERS applications.

addition, oxidation occurs faster at Ag surfaces, hindering their shelf life and usefulness in clinical settings.[23]

The size and shape of the nanoscale metallic components play a large role in the level of enhancement generated. Ideal features fall in the range of 30-100 nm (i.e., about 10-fold smaller than the wavelength of interrogating light); anything larger creates resonance issues and strong dampening of LSP resonances as the result of increased radiation losses.[24] Many studies have conducted detailed testing of various shapes, geometries, and layouts of SERS-active materials, showing the various influences this parameter has on overall enhancement.[25–27] In general, nanoparticles assembled within a few nanometers of each other, or ones that exhibit sharp points, can create a stronger SERS effect compared to single free-floating particles.[24] The generation of these electromagnetic "hot spots" arise from coupled resonances in the gaps between the metallic nanostructures. An example of the spatial distribution of the enhancement zone between different nanoparticle shapes can be seen in **Figure 1.5**.
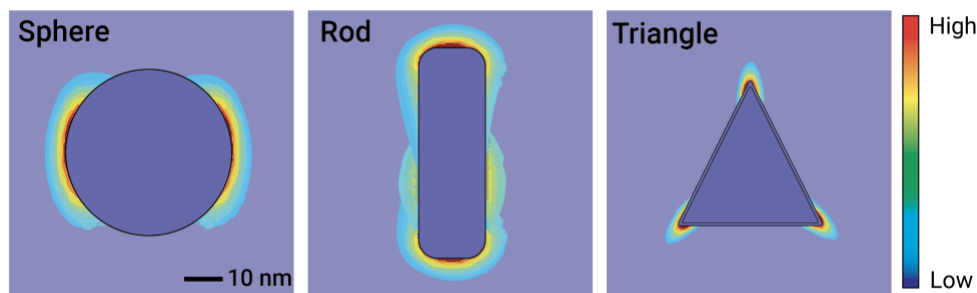
Figure 5.5: Local enhancement zones for metal nanoparticles vary based on their shape. Edges and sharp peaks tend to have a higher level of enhancement that decrease exponentially with the distance away from the surface.

Besides the electromagnetic enhancement discussed above, an additional SERS mechanism can be noted by the chemical enhancement theory. This theory includes several different processes but, in this case, it is best to consider what happens specifically with a metal substrate. In this situation, there is a charge transfer between the highest occupied molecular orbital (HOMO) of the molecule and the Fermi level of the metal onto which it is adsorbed.[24,28] The light-induced charge transfer

could affect the electronic or geometrical structure of these adsorbed molecules, which leads to intensity changes and some observable spectral shifts.[29] Although this is important to consider for the detailed nuances of the SERS mechanism, it only results in modest an order of magnitude signal increase, therefore is much less significant than the electromagnetic enhancement, which can increase the Raman readout by up to 10^{12} in some cases, and more commonly by 10^6-10^8.[24]

The development of robust and effective SERS materials is a highly active area of research.[30–32] There are essentially two types of materials: synthesized nanoparticles in solution and planar substrates of micropatterned nanostructures. Several commercially available SERS substrates exist and can be purchased from companies such as Hamamatsu, Silmeco, and Ocean Insight. They are highly uniform and provide robust SERS signal, but these substrates are often single-use and more expensive than developing materials in-house. Alternatively, SERS materials can be synthesized or fabricated in house although each comes with challenges. For planar or micropatterned substrates there is a need for strict nanofeature spacing that often requires expensive electron beam lithography equipment and specialized training, but these materials tend to be more consistent with their SERS signal and provide high enhancement factors.[33–35] Another popular option is nanoparticle synthesis methods that allow for nanofeature tuning, such as sharpening, templating, or and size selection. Although these methods tend to be faster and less expensive, they are harder to accurately control and often involve dangerous precursors such as concentrated nitric acid and dimethylformamide.[36,37] Regardless of the method employed, the goal is to develop a highly sensitive SERS material that produces robust signal with a high enhancement factor.

1.4 Application of Raman/SERS for biological applications

To date, Raman and SERS have been applied to a wide range of biological and medical applications as both a diagnostic and analytical tool. Raman analysis of biological materials can give insight into information about structure, composition, interactions, and dynamics.[38] Similarly,

pathological conditions are often connected to molecular composition and structural changes in the affected tissues or cells which can be reflected in the Raman spectra of the samples, making it a useful tool to gain detailed insight into multiple simultaneous changes.[39] Although detailed and highly sensitive information can be extracted from Raman measurements, there has been no true clinical adaption of the technique (i.e., no FDA-approved platform is based on Raman). This is partly due to lagging of more usable instrumentation and the need for easy-to-make and inexpensive SERS materials. Nonetheless, Raman and SERS remain a viable and attractive option for biomedical applications.

Common applications of Raman and SERS include drug identification and detection,[40,41] in-line monitoring of wastewater,[42,43] environmental toxin and pollutant testing,[44,45] as well as preclinical diagnostic applications to diabetes,[46,47] cardiovascular diseases,[48,49] neurodegenerative diseases,[50–52] and cancer.[53–58] Of all the categories listed, diagnostic applications (specifically in cancers) are one of the most common to utilize the power of Raman. Cancers that lack robust early-stage biomarkers (such as HNC and OvCa) could stand to immensely benefit from Raman and SERS. It is highly unlikely that a single biomarker will be found that reports on the disease presence and staging of these cancers. Instead, a comprehensive spectral fingerprint— such as those provided by Raman and SERS—can provide more detailed chemical analysis of a sample and allow for robust data analysis to show trends or relevant ratios that may provide a better diagnostic measure.

1.5 History of liquid biopsy as a diagnostic method

Replacement of current invasive biopsy techniques with liquid biopsy tests would be a highly impactful clinical goal. Use of liquid biopsy-based methods are currently being studied with Raman and SERS as an interrogation tool[59–61] and there are many different possible levels of testing that can be done. Analysis of whole blood may provide the most comprehensive information but also

might be overwhelming in terms of sample complexity and correlating the chemical readout to specific factors. Use of plasma and serum reduces this complexity by a measure while still maintaining biomolecules from many different systems, but also has the potential to be too complex to make meaningful parallels. Other biofluids that are of interest include saliva, especially in the context of HNC where the tumors occur in the mouth and throat, because it may be enriched in cancer-specific metabolites and factors that can give important details.

Within these biofluids are molecules of potential interest. Liquid biopsy was first developed around 2013 and was initially used to assess circulating tumor cells (CTCs) that have dethatched from the metastatic lesion and traveled through the bloodstream to other parts of the body.[62] Since the advent of this detection method additional cell-free tumor related components such as DNA, mRNA, micro-RNA, and tumor-educated platelets (TEPs) have also been analyzed to give insight into the
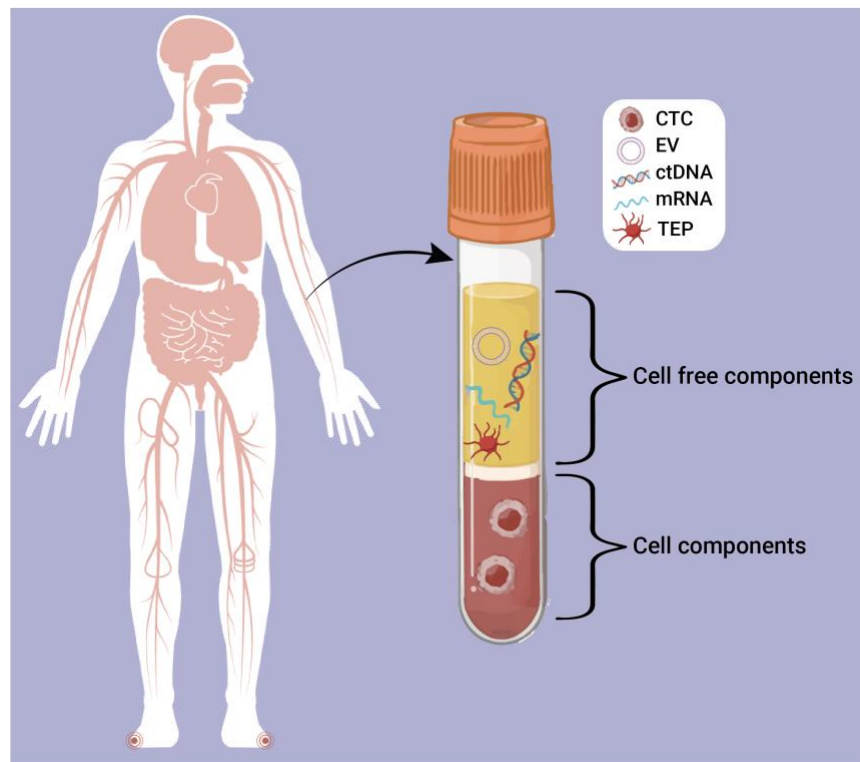
Figure 6.6: Overview of liquid biopsy methods. A blood draw taken from a patient contains many biomolecules of interest. Circulating Tumor Cells (CTCs) can be found in the red blood cell fraction. Cell free components such as extracellular vesicles (EVs), ctDNA, mRNA, and tumor-educated platelets (TEPs) can be found in the plasma or serum fraction.

disease state of a patient (**Figure 1.6**).[63] Unfortunately, these factors occur at very low concentrations in the peripheral blood (<10 molecules/mL)[63] which poses a significant challenge for adequate detection and analysis.

Another interesting source for promising liquid biopsy material are extracellular vesicles (EVs). EVs are nanoscale particles made of a lipid bilayer that are released from all cell types and typically range in size from 30-150 nm.[64] The field's understanding of EVs is continuously evolving but it is well-accepted that they are a highly diverse and complex group of nanoparticles that contribute to many biological functions in both local and distant body environments.[65] Associations between EVs and many pathophysiological processes have been identified, including cell proliferation and viability, bone formation, promotion and suppression of angiogenesis, and immunosuppression.[66]

1.6 Extracellular Vesicles as disease mediators and their diagnostic potential

EVs have been implicated as mediators of a host of different diseases, ranging from cardiovascular and metabolic diseases,[67–69] neurological disorders,[70,71] inflammatory diseases,[72,73] and cancer.[74–80] Specifically in the context of cancer, EVs play an active role in pre-metastatic niche formation by organotrophic targeting through integrin-mediated processes.[81] Cancer cells will release their own EVs to travel to initiate metastatic locations, clear populations of immune cells,[82] stimulate angiogenesis,[83] remodel the matrix,[84] and promote tumorigenesis.[85] EVs are an attractive option as diagnostic material because they are highly abundant, can be readily isolated from biofluid sources (blood, saliva, urine, etc.)[86], and exhibit surface expression reflective of their parent cell[65], meaning they are likely to house characteristics specific to the cancer host cells. However, EVs are inherently heterogeneous with size being a major driver of this diversity, a factor that can complicate the analysis of specific populations.[87]

Assessment of EVs follows isolation from a biofluid source. There are three commonly applied isolation techniques: ultracentrifugation (UC), density gradient (DG), and size exclusion chromatography (SEC). UC and DG are density-based methods that utilize centrifugation steps to concentrate EVs in a specific location within the tube.[88,89] SEC is a size-based method that sends samples through a gel matrix with larger molecules eluting faster as smaller molecules get trapped in pores within the columns.[90] For EV detection and characterization there are standard techniques recommended for use to ensure proper isolation has taken place.[86] Western Blot and BCA assays are used to quantify average composition and levels of proteins in bulk EV preps. Concentration and size distribution can be attained from Nanoparticle tracking analysis (NTA) that analyzes the Brownian motion of the particles as they move through a microfluidic device. More recently developed instruments like Exoview can also provide size and concentration measurements with additional surface protein characterization through fluorescently labeled sandwich antibody spots.
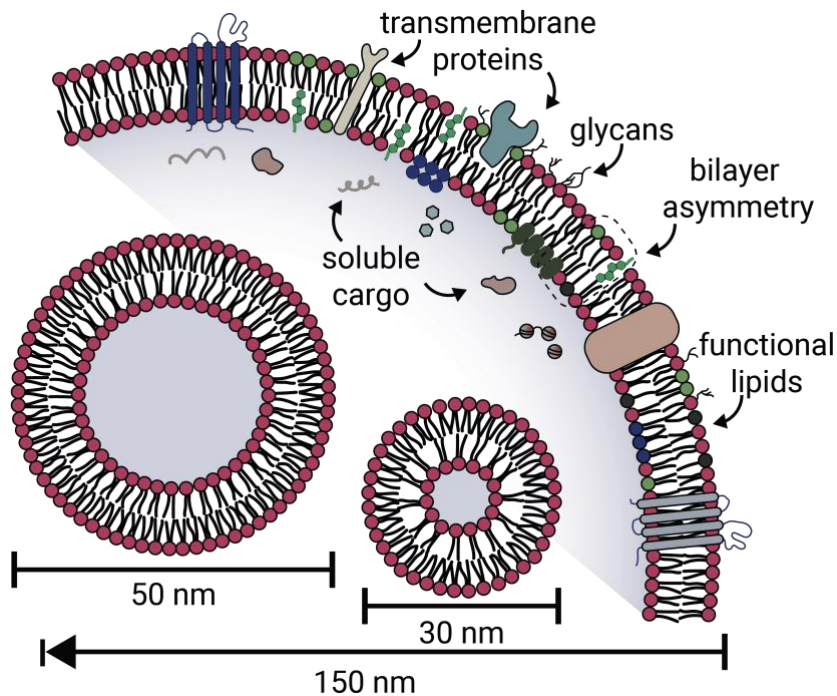
Figure 7.7: To-scale schematic of biomolecular makeup of EVs across heterogenous length scales. The characteristic double lipid bilayer is present in all sizes of vesicles, with soluble cargo located internally. Surface expression of different molecules include functional lipids, glycans, and transmembrane proteins. An immense difference in intraluminal volume, surface area, and thus biomolecular content is found across the sizes of 30 − 150

EVs consist of distinct biomolecular classes including lipids, nucleic acids, proteins and other peptides, carbohydrates, growth factors, structural components like actin and fibronectin, and even hormones (**Figure 1.7**).[65] The rich diversity of these biomolecules make them an attractive source for diagnostic information specifically in the context of Raman and SERS analysis. There have been numerous studies using both Raman and SERS as sensitive readouts for isolated EV samples. This work has been applied to cancer in the way of detection and diagnostics,[91–97] response to treatment,[98–100] and recurrence.[101–103] The unique characteristics of EVs mentioned above support the notion that they are an attractive source of biomaterials that can give unique snapshots into a patient's disease state. This, coupled with the high sensitivity and speed of Raman, could help develop a highly impactful liquid biopsy diagnostic platform to be implemented in clinical cancer detection pipelines. Despite this initial promising work, there is still much to uncover and optimize regarding spectroscopic readout of the heterogenous EVs present in patient biofluids in the context of translational diagnostic platforms.

1.7 Dissertation Objectives

To accomplish clinical implementation, liquid biopsy methods must be quick, reliable, highly sensitive, and economical. Neither Raman nor the extension of SERS is currently used in an impactful clinical capacity, but the advantages of the technique make it attractive to develop into such a tool. Furthermore, there are multiple biofluid sources ranging from blood plasma to EVs that can provide important chemical spectral fingerprints to aid in cancer detection and monitoring. With these various levels of materials and information, it is vital to try and find some cohesiveness to develop a robust liquid biopsy pipeline. Success of such an accomplishment would easily fit into the standard clinical care routine of cancer patients but improve health outcomes and reduce the financial burden of the individual. There is high merit in placing emphasis on the development of a Raman/SERS based platform that can detect cancerous signals from various biofluid sources. Therefore, the objectives of

this dissertation are three-fold. 1) To assess the viability and validity of Raman to uncover chemical signals correlated to a disease state. 2) To understand the applicability of EVs as diagnostic materials. 3) To develop new SERS materials that are inexpensive, robust, and compatible for clinical use in order to produce a more sensitive diagnostic readout.

Chapter 2: Materials and Methods

2.1 Antibodies, reagents, and chemicals

Analytical standards of chylomicrons, very low-density lipoprotein (VLDL), low-density lipoprotein (LDL), and high-density lipoprotein (HDL) isolated from human plasma were obtained as lyophilized powders from Millipore Sigma. Gold (III) chloride trihydrate (HAuCl4), trisodium citrate dihydrate, adenine, 4-mercaptobenzoic acid (4-MBA), poly (vinylpyrrolidone), MW = 10,000, (PVP-10), melamine, ethanol (EtOH), *N,N*-dimethylformamide (DMF), cysteamine, and phosphate buffered solution (PBS) were purchased from Sigma Aldrich (St. Louis, MO) and used without any further modifications. Pierce BCA Protein Assay Kit was purchased from ThermoFisher Scientific (Waltham, MA) and used according to the manufacturer's instructions. Glutaraldehyde and osmium tetroxide were provided by the Biological Electron Microscopy Facility for electron microscopy sample preparation. Silicon wafer chips for nanoparticle deposition were purchased from Ted Pella, INC. (Redding, CA). Paraformaldehyde, glutaraldehyde, uranyl-oxalate, and methyl cellulose were purchased from Electron Microscopy Sciences (Hatfield, PA). Transmission electron microscopy formvar carbon grids were purchased from VWR (Radnor, PA). SKOV-3 and HEC-A-1 cells were bought from ATCC (Manassas, VA). T-75 flasks, Gibco McCoy's 5A medium, fetal bovine serum (FBS), Gibco Exosome-Depleted FBS, and penicillin−streptomycin were acquired from ThermoFisher Scientific (Waltham, MA). CELLine 1000 AD bioreactor flasks were purchased from DWK Life Sciences (Millville, NJ). Size exclusion chromatography columns of 35 and 70 nm size were obtained from Izon Science (Medord, MA). Eppendorf tubes for EV collection were purchased from Eppendorf (Enfield, CT). Commercial SERS substrates were bought from Ocean Insight (Orlando, FL), Hamamatsu (Japan), and Silmeco (Copenhagen, Denmark). The biosilica/AgNP composite substrates used in this study were prepared and provided by Dr. Wachsmann-Hogiu at McGill University.

2.2 Cell Culture

Two cell lines were cultured to model OvCa and EnCa: SKOV-3 and HEC-A-1 cells, respectively. Cells were first cultured in T-75 flasks with Gibco McCoy's 5A medium and 10% (v/v) FBS and 100 units/mL penicillin−streptomycin. From here, 25×106 cells were used to seed high-yield EV collection CELLine 1000 AD bioreactor flasks.[34] The bioreactor's upper compartment was supplied with 950 mL of Gibco McCoy's 5A medium complemented with 10% (v/v) FBS and 100 units/mL penicillin−streptomycin. The bioreactor's cell compartment was supplied with 15 mL of Gibco McCoy's 5A medium with 10% (v/v) Gibco Exosome-Depleted FBS and 100 units/mL penicillin−streptomycin. The T-75 flask and bioreactor cell cultures were propagated and cultured at 37 °C, 95% relative humidity, and 5% CO_2 atmosphere. For EV isolation, the cell compartment medium (15 mL) was collected once a week from the bioreactor, and 15 mL of fresh medium was added. Concurrently, the upper compartment medium (950 mL) was discarded and replaced with the same amount of fresh medium.

2.3 Clinical biofluid collection and processing

2.3.1 OvCa samples

The EVs studied in this work were isolated from clinical serum samples provided by the UC Davis Comprehensive Cancer Center (UCDCCC) Pathology Biorepository Resource (IRB ID: 1314848-1). Patient serum samples were obtained as deidentified remnants following a clinician ordered CA125 assay. Histopathology analysis by trained clinicians identified sample types as either endometrial cancer (EnCa), ovarian cancer (OvCa), or benign (control). Therefore, some patients are not diagnosed with cancer even after the CA125 assay; thus, negative control samples can be obtained. Approximately 1 mL of serum was obtained per patient, from which EVs were isolated.

2.3.2 HNC samples

Patients were consented to blood draws and saliva collection during scheduled head and neck cancer surgeries in the University of California, Davis Department of Otolaryngology and all methods were performed in accordance with the relevant guidelines and regulations. Saliva was aliquoted into Eppendorf tubes with a volume ranging from 200-1000 µL and frozen at -80ºC until retrieval. Blood draws were isolated to plasma and serum and aliquoted into four tubes each with volumes ranging from 200-500 µL and frozen at -80ºC until retrieval. Saliva was thawed in an ice bath and further aliquoted into smaller storage volumes if the original sample volume allowed.

2.4 Gas chromatography and mass spectrometry conditions

Metabolomics data was collected for primary and polar metabolites using gas chromatography–time of flight mass spectrometry.[104] Briefly, 30 µL of either plasma or saliva was extracted at -20ºC with 1 mL degassed isopropanol/acetonitrile/water (3/3/2). Extracts were dried down, cleaned from triacylglycerides using acetonitrile/water (1/1), and derivatized with methoxyamine and trimethylsilylation. Samples (0.5 µL) were injected at 250ºC to a 30m rtx5-SilMS column, ramped from 50-300ºC at 15ºC/min, and analyzed by -70 eV electron ionization at 17 spectra/s. Raw data were deconvoluted and processed using ChromaTOF vs. 4.1 and uploaded to the UC Davis BinBase database[105] for data curation and compound identification.[106] Resultant data were normalized by to their respective average MTIC for each sample type.

2.5 Raman acquisition and processing

2.5.1 General acquisition parameters

All spectra were acquired using a custom-built inverted Raman scanning confocal microscope with excitation wavelength of 785 nm and a 60x, 1.2 NA water immersion objective on an inverted IX73 Olympus microscope. An Andor Kymera-3281-C spectrophotometer and Newton DU920PBR-DD CCD camera were used for Raman spectra capture and Solis v4.31.30005.0 software was used for

initial processing. Analysis of the spectral data was performed using MATLAB v2021a (Math-Works, MA, USA) via a custom script. Cropping, penalized least-squares (PLS) background correction,[107] smoothing,[108] and unit normalization were applied for spectral pre-processing. Spectra were subjected to PCA and LDA/QDA based on the corresponding MATLAB built-in functions applied to a custom script.

2.5.2 Spontaneous Raman of HNC samples

Plasma and saliva were analyzed in both a native and dried state. Biofluid samples were thawed on ice and 2 µL was pipetted onto a quartz coverslip. For native measurements, the quartz coverslip was immediately placed on our Raman microscope and spectra were collected. For dried measurements, the native spots were allowed to dry for 15 min under ambient conditions prior to measurement. For measurements, exposure time was 30 sec per scan with laser power of 65 mW. Substrates were randomly sampled at 5 regions with 100 spectra collected and averaged at each region. Spectra containing cosmic rays were removed from analysis. For each of the patients with both biofluid samples present, the average plasma spectra and average saliva spectra intensity values were exported into a.txt file. Arbitrary values were assigned to the x-axis starting with 1 and ending with 1694. New files (with plasma first, followed by saliva) were analyzed with the same processing parameters outlined above.

2.5.3 SERS of HNC samples

SERS nanogold substrates (Ocean Insight) were first prepared by pipetting 10 µL of 20 mM cysteamine in 95% ethanol onto the surface. After 1 h incubation, substrates were washed by dipping into an Eppendorf tube containing ultrapure water and 100-fold dilutions of EV samples in ultrapure water were prepared. 40 µL of this solution were pipetted onto the substrates and incubated at room temperature for 2 h. The substrates were then washed three times by briefly dipping into Eppendorf tubes containing ultrapure water. Washed substrates were inverted onto #1.5 glass coverslips for

SERS measurements. For measurements, exposure time was 1 s per scan with laser power of 5 mW. Substrates were randomly sampled across 5–10 SERS-active regions, with at least 100 spectra collected at each spot.

2.5.4 SERS of OvCa samples

Small sensor pieces (~2 mm by 5 mm) were cut out from the prepared parallel (0.2 × 5 cm) stripe-shaped plasmonic sensor substrates. One 2 × 5 mm piece was used per measured sample. Before EV incubation, the sensors were pretreated at pH 6.5 with 10 μL of 20 mM (in 95% EtOH) cysteamine. After 1 h, the substrates were washed 2−3 times by dipping into Eppendorf tubes of pH 6.4 buffer. EV samples were diluted 1:100 in the same buffer, and 30 μL drops were pipetted onto the substrates, covered, and incubated at room temperature for 2 h. The substrates were then washed again and inverted onto a #1.5 glass coverslip for SERS measurements. All steps were performed in liquid conditions, including the EV measurements. Exposure time was set to 1 s per scan with a laser power of ~1−5 mW unless otherwise specified. Across all samples, SERS spectra were sampled randomly in 5−10 different spatial locations with a 20-spectra kinetic series collected. Representative spots were chosen for data collection when noticeable SERS peaks became visible and stable during randomly traversing across the substrate, so there is a positive bias in each spot for containing EV materials. Tests were performed to choose an adequate number of PCs for the LDA, simultaneously avoiding overfitting. Thus, an LDA analysis using the two first PCs (PC1 and PC2) was determined to be the most suitable for the analysis, consistent with the data presented throughout this study.

2.5.5 SERS of Nanofoams

Careful focusing was carried out for each sample to ensure the bulk of the substrate is centrally located in the focal volume. For measurements, raster scans were performed as 20 × 20 pixels with a 400 nm step size equaling an 8 μm by 8 μm area. Heat maps were generated by selecting a pronounced

spectral feature with a normalized color scale. Five scans of 400 spectra (i.e., 20 × 20 pixels) were performed on each substrate and averaged.

2.6.6 Theoretical Calculations of SERS surface coverage

To theoretically estimate the surface coverage of EVs on an average SERS scaffold substrate used in this study, we calculate two different exemplary situations making the following premises:

- A 2 mm x 2 mm piece of substrate is used

- A 1:100 dilution of 5×10^{10} EVs/mL stock solution is used

- An average EV diameter ~100 nm

- 30 μL of (1:100) diluted EV sample is used

Thus, the particle concentration of EVs in the 30 μL (1:100 diluted) droplet pipetted onto the SERS substrate is 5×10^{8} EVs/mL. By this, the total amount of EVs in the 30 μL droplet is 1.5×10^{7} EVs. Hence, with the assumed size of the substrate and the average EV diameter, it is theoretically possible to 'fit' 4×10^{8} EVs as a 'monolayer' on the substrate area given that the piece of substrate is fully covered in EVs. Finally, these result in the total experimental EV coverage of

$$\left(\frac{1.5 \ \times \ 10^{7} \ \text{EVs}}{4 \ \times \ 10^{8} \ \text{EVs}} \right) \times 100\% \sim 3.75\%$$

Thus, with the given EV stock concentration and (1:100) dilution we only cover significantly less than 4% of the substrate area.

If 100x higher particle concentration is used (i.e., stock of 5×10^{12} EVs/mL), these results in the total experimental EV coverage of

$$\left(\frac{1.5 \ \times \ 10^{9} \ \text{EVs}}{4 \ \times \ 10^{8} \ \text{EVs}} \right) \times 100\% \sim 375\%$$

2.6 EV isolation and characterization

2.6.1 Isolation by Ultracentrifugation

First, 1 mL of serum was centrifuged at 300g for 10 min at 4 °C to clear any remaining whole cells. The resulting supernatant was then centrifuged at 2000g for 15 min at 4 °C followed by a 10,000g spin for 30 min at 4 °C to pellet any dead cells and cell debris/larger microvesicles, respectively. All low-speed spins were performed using a Beckman Coulter Microfuge 20R centrifuge with an FA361.5 Biosafe rotor. Finally, the samples were ultracentrifuged twice at 120,000g for 70 min at 4 °C to pellet EVs, dispersing in ultrapure water between spins. Ultracentrifugation was carried out using a Beckman Optima TLX Ultracentrifuge with a TLA 100.1 fixed angle rotor. Resulting pellets were resuspended in up to 100 µL of ultrapure water and stored at −80 °C for up to a few weeks until use. Samples were aliquoted to reduce freeze−thaw cycling.

2.6.2 Isolation by density gradient

200 µL of pre-cleared plasma was layered on to a 5%–40% discontinuous iodixanol (OptiPrep, or OP) gradient. The OP layers were prepared by diluting 60% OP in varying volumes of a stock solution containing 850 g of 0.25 M Sucrose, 200 µL of 1 mM EDTA, and 500 µL of 10 mM Tris-HCL (pH-7.4). Gradients were prepared in layers in Thinwall Polypropylene Tubes (Beckman Coulter) using 3 mL syringes with 26-gauge stainless steel needles. Each layer was filled from the bottom of the tube, starting from light to heavy, 3 mL of 5% OP, 3 mL of 10% OP, 3 mL of 20% OP, 3 mL of 40% OP, and 1 mL of sample for a total of 13 mL. Following sample loading, gradients were spun at 100 000g at 4 °C for 24 h using an SW 41 Ti Swinging-Bucket Rotor and an Optima LE-80 K ultracentrifuge (Beckman Coulter). The samples were manually fractionated from the bottom, with a total of thirteen 1 mL fractions collected per tube. Each fraction was additionally centrifuged to remove the remaining iodixanol. For this, 500 µL of each fraction was pipetted into an Amicon Ultra-0.5 mL centrifugal filter with 100 K MWCO and spun at 14 000g at 4 °C for 5 min using a Microfuge

20R (Beckman Coulter). 400 µL of PBS was added to each filter and then spun again for 5 min (this washing repeated 3 times in total). The filters were then inverted inside fresh tubes and spun 1000g at 4 °C for 2 min. Collected solutions of ∼60 µL were stored at −80 °C.

2.6.3 Isolation by size exclusion chromatography

EVs were collected with an Automatic Fraction Collector (AFC) and pre-formed size exclusion columns (qEV70, Izon Science). Thirteen 1.5 mL Eppendorf tubes were loaded into the AFC carousel and a single qEV70 column was inserted into the mount. The column was flushed with 4 mL of filtered PBS buffer at room temperature. After the column was flushed, excess buffer was removed from the top of the column using a 10 µL pipette. 150 µL of the pre-cleared plasma was loaded on the column and fraction collection started. Once the sample reached the upper frit of the column, it was topped off with 4 mL of PBS buffer. After the void collection was complete, the machine collected 200 µL of each fraction. Fractions 1–3 were pooled, and the resulting solution was concentrated using Amicon Ultra 0.5 mL centrifugal filters to a final volume of 100 µL and stored at −80 °C for maximally 5 days before following experiments were run.

2.6.4 Nanoparticle tracking analysis

Sample particle concentrations and size distributions were measured using a NanoSight LM10 (Malvern Panalytical) equipped with a 405 nm blue laser and sCMOS camera. 1000-fold dilutions of EV isolates prepared as described above where thawed. Ultrapure water used to prepare dilutions was filtered through pre-wet 0.1 µm Nylon syringe filters (Whatman) immediately prior to measurement. Filtered ultrapure water was also used to flush the NTA chamber and tubing before sample addition to ensure contamination was minimized during measurement. 1 mL of each diluted sample was loaded into a syringe and placed on an automatic syringe pump for injection. Data was recorded as three 30 s videos containing a minimum of 200 particle tracks per video, recorded at camera level 12. NTA 3.1 software was used to analyze the data and track the Brownian motion of the individual particles

recorded. Subsequently the software calculated hydrodynamic diameters (nm) of the tracked particles using the Einstein-Stokes relation, and the count-based concentrations (particles per mL) are simultaneously obtained as the number of particles and volume of the sample chamber are known.

2.6.5 Protein concentration measurement

Total protein concentration for each sample was measured with a BCA assay (Pierce BCA Protein Assay Kit, ThermoFisher Scientific) following the manufacturer's instructions. 15 µL of EV stock was mixed with 8 µL of RIPA buffer and 57 µL ultrapure water then vortexed briefly and incubated on ice for 30 min prior to starting on the assay instructions.

2.6.6 Trypsinization of EV glycocalyx

For EV treatment with trypsin, prior to measurement, 5 µL of EV sample was mixed with 500 µL of 0.25% w/v trypsin, pipetted rapidly up and down, and then incubated at 37 °C for 1 h to allow for cleavage of extraluminal surface moieties. Samples were washed thrice with ultrapure water in 10 kDa Amicon Ultra (0.5 mL) regenerated cellulose centrifugal filters according to the manufacturer's instructions.

2.7 Electron microscopy of EVs and substrates

For transmission electron microscopy (TEM) of EV isolates, negative staining was carried out as previously described without modification.[109] TEM images were obtained on a Talos L120C (ThermoFisher Scientific, MA, USA). 2 µL of nanofoam solution was dropped onto copper formvar carbon support grids and allowed to dry before imaging.

Scanning electron microscopy (SEM) micrographs of SERS substrates before and after incubation with EVs were acquired using a ThermoFisher Quattro S (ThermoFisher Scientific, Waltham, MA). Secondary electron scattering from the surface was detected using an Everhart–Thornley detector (ETD), and the backscattered electrons were detected with an annular backscattered (ABS) detector. For the SEM sample preparation, the pretreated substrates were first placed in a 12-

well plate the SERS active surface facing up, simultaneously avoiding drying. The substrates were then washed thoroughly 2 times with sodium phosphate buffered solution (PBS), sequentially submerged for 15 min in glutaraldehyde, and finally in osmium tetroxide for in 15 min (no washing between the steps). Consequently, a graded series of ethanol (EtOH) solutions were used to dehydrate the samples as follows: 30% (5 min), 50% (5 min), 70% (5 min), 95% (2 Å~ 5 min), and 100% (2 Å~ 5 min). As the last step of sample preparation, the substrates were allowed to dry overnight in a fume hood. For imaging, the substrates were mounted on metal studs using two-sided carbon tape. The typical imaging parameters were working distance 10.0–13.5 mm, spot size 3.0, accelerating voltage 10.00 kV, chamber pressure 100 Pa.

2.8 Nanofoam synthesis and characterization

2.8.1 Nanofoam synthesis

Gold nanofoams (AuNFs) were fabricated by mixing trisodium citrate dihydrate and HAuCl4 reactants at differing molar ratios of ($R = C_{citrate}/C_{gold}$). Initial experiments were carried out with $R = 12$ on a stir plate following rinsing with EtOH and drying under air. 31 mg of HAuCl4 was added to 32 mL of ultrapure water in a 50-mL round bottom flask with consistent magnetic stirring maintained at 550 rpm. 367.5mg of trisodium citrate dihydrate was added directly to the flask while stirring. The reaction proceeded at room temperature under constant stirring. The yellow solution quickly turned clear followed by darkening to a purple/black within an hour of the reaction start. Aliquots were taken from the solution at 2 h and 5 h, and the reaction was stopped at 8 h. By this point, AuNFs had precipitated out of solution to form visible black masses at the bottom of the flask, and the solution became clearer. Foams were collected by gentle decantation or left in the flask for subsequent roughening procedure.

2.8.2 Nanofoam roughening

For roughening, the AuNFs were produced as above, except at the 6 h mark, excess volume was removed until 5 mL of the original solution (containing dispersed AuNFs) remained in the flask. A separate solution of 7 mL DMF, 0.1875 g PVP-10, and 40 µL of 50 nM HAuCl4 (in MQ water) was made and added to the original nanofoam mixture. The flask was clamped and an ultrasonication probe (Sonics & Materials INC., CT, USA) inserted into the solution while avoiding touching any of the glass. The mixture was sonicated for 15 min at 30% power (power = 130 W, frequency = 20 kHz) at which point a noticeable blue color shift occurred in the solution. Resulting roughened nanofoams (RNFs) were used in downstream assays as is with no further purification.

2.8.3 Nanofoam deposition onto filters

Nanofoams were dropped using a Pasteur pipette onto 13 mm, 0.22 µm pore size, hydrophilic PVDF Durapore filter paper (MilliporeSigma) placed in a ceramic Büchner funnel under vacuum. Build-up of nanofoams was achieved by continuous dropping before allowing to completely dry. Adequate surface coverage was achieved after 75 drops of AuNF solution, determined by creating filters with increasing numbers of drops (in increments of 25 up to 100 drops) and then measuring SERS signal at random spots throughout the substrate. SEM images of the surface coverage with corresponding pictures of the filters can be seen in Fig. S1. The Raman standard melamine was used as a test molecule due to SERS specific peaks that are only visible when the plasmon resonance is high enough. The emergence of enhanced signal across large areas of the substrate, as suggested by a measurable increase in reporter analyte signal, indicated sufficient AuNFs structure to generate SERS. Subsequent filters were made with at least 75 drops of our reaction.

2.8.4 EM of Nanofoams

Scanning electron microscopy (SEM) images were obtained using a Thermo-Fisher Quattro S (ThermoFisher Scientific, Waltham, MA) to visualize AuNF surface morphology. The instrument is

equipped with an Everhart-Thornley detector (ETD) for secondary electron imaging. Prior to imaging, filters were sputtered with 5 nm gold to reduce substrate charging from the electron beam. Substrates were then mounted on metal studs using two-sided black carbon tape, and the following typical imaging parameters were applied: working distance 10.0 mm, spot size 3.0, accelerating voltage 10.0 or 15.0 kV. Transmission electron microscopy (TEM) images were obtained on a Talos L120C (Thermo Fisher Scientific, MA). 2 µL of nanofoam solution was dropped onto copper formvar carbon support grids and allowed to dry before imaging.

2.8.5 SERS surface area modeling and nanostructure analysis

The analysis procedure is as follow:

1. Open the image with ImageJ/FIJI.

2. Convert to 8-bit greyscale (Image –> Type --> 8-bit).

3. Analyze --> Set Scale --> Remove Scale

4. Use 'Line' tool + Hold down shift to draw a line on the scale bar in the (SEM/TEM/etc.) image

5. Analyze --> Set Scale --> Add scale using the correct dimensions and units (e.g., 1000 nm) --> If you want the scale to apply to apply to other images in the session as well, tick also 'Global' box (Note: Tound the 'Distance in Pixels' number if it is e.g. 368.7 --> Write 369 in the box).

6. Select rectangle tool from the toolbar --> Draw a rectangle around the area you want to analyze.

7. Image --> Duplicate (Produces a copy of the demarcated area)

8. Using the image obtained at step 6.: Process --> FFT --> Bandpass Filter to remove excess noise from the image (Filter large structures e.g., down to 20 pixels + Small structures up to 3 pixels; note that these settings need to be tested and iterated for each case for optimal results + Suppress no stripes + Tolerance of direction 5% + Autoscale after filtering on + Saturate image when autoscaling on --> OK).

9. Activate the filtered image --> Image --> Adjust --> Threshold --> Select the desired color for the background and the particles --> Adjust the threshold bars so that at the end the particles are highlighted in the desired particle color and the background correspondingly in the background color --> Click Apply.

10. It is advisable to clean up the known artefacts manually by hand using the 'Eraser' tool (Red double arrow on the upper right corner of the control panel --> Drawing Tools to reveal the drawing tools) --> If needed, change the color of the eraser --> Edit --> Options --> Colors --> Background (select e.g. black/white). Note also that switching between the B&W and red themes in the 'Threshold' view (by default the 'Dark Background' box is ticked) can help to spot the areas that need to be erased. In a typical situation either set a very stringent threshold is set such that a lot of the relevant structures become excluded, which biases the results, *or* a less restrictive threshold is set but then the image need to be cleaned up more thoroughly, which takes more time. As a rule of thumb, a better practice is to spend more time during the manual clean up rather than cut off most of the relevant structures by thresholding too rigorously.

11. Keep the processed image active --> Analyze --> Analyze Particles --> Size (Set 0-infinity if the particles/features to be analyzed are very unevenly sized; if not, this option can be used to delimit the analysis to certain max size particles) + Circularity (Set 0.00-1.00 if the morphology of the particles is uneven as seen in the exemplary images above; if not, the lower boundary can be increased to e.g., 0.50, such that only more circular shaped particles are counted and analyzed) + Show outlines + Display Results on + Summarize on + Add to Manager (this will add the results in ROI manager, which is very useful) --> OK. The 'Summary' and 'Results' logs enable quantitative nanostructure analysis as desired.

12. If you want to have an overlay and see how well the particles (or features of interest) have been fitted, duplicate the selected area again (originally selected using rectangle tool above at step 6.), and

select "Show All" in the ROI manager (it is typically useful to untick the box "Labels" as the overlay becomes otherwise quite unclear), and finally click "Flatten [F]" that will 'burn' the overlay onto the image. If the "Flatten [F]" is not selected, the overlay will not be saved if you try to save the image e.g., as .tiff.

13. Save the desired files (e.g., particle analysis results, overlay image etc.).

2.8.6 Simulation of optical properties for the nanofoams

<u>AuNF and RF Construction via SEM image interpolation</u>

A 500 nm x 500 nm 3D nanofoam structure is reconstructed using cropped SEM image via MATLAB. Native SEM image is smoothened with Gaussian filter to remove noise. For RNFs specifically, feature height was scaled assuming the feature surface height is isotropic with the surface area; Similarly, for AuNFs, the 3D structure is scaled accordingly assuming the layer height is 45 nm – the modal diameter of the nanofoam determined by TEM imaging. The final 3D surface structure is exported as an STL solid via surf2solid open-source package.

<u>Alternative approach to AuNF Construction</u>

The topological structure of the AuNFs is inferred from the SEM image and the top layer of the AuNF is used as the motif for simulation. Nanofoam structure is assumed to be a single 45-nm thick layer and constructed in Solidworks and exported as an STL file. The STL file is then directly imported into Lumerical FDTD 3D electromagnetic simulation for further analysis.

<u>Alternative approach to RF Construction</u>

RNF is modeled as a collection of gold nanospheres that range from 15 nm to 45 nm in diameters in Lumerical FDTD 3D Electromagnetic Simulator. 200 particles are randomly distributed within a 700 nm by 700 XY space while the particles are allowed to overlap to emulate the aggregate structure seen from the SEM images. X, Y, Z standard deviation, which stands for the number of standard deviation half the sphere covers, is set to 3.

FDTD Simulation

The electric field around the structure is determined using Lumerical FDTD 3D electromagnetic Simulation. Mesh size is chosen to be 1.5 nm uniformly in X, Y, Z directions to ensure mesh symmetry while providing the capability to resolve near field (<10 nm) surface enhancement. A total-field scattered-field propagating at 785 nm is injected directly normal to the surface of the 3D structure. A 3D frequency-domain field and power monitor are used to collect the local electric field of the nanofoam structure. The material property of the structure is defined by Au (Gold)-CRC. The structure is enveloped by planar solid defined by water's optical property. Stabilized PML conditions are used as the boundary conditions to ensure convergence. The enhancement factor for surface-enhanced Raman scattering can be described as $(E/E_0)^4$ where E is the local electric field and E_0 is the input source electric field. Maximum EF at individual mesh cells defined by the XY view is then plotted to visualize the hotspot distribution.

Chapter 3: Fused Raman spectroscopy analysis of blood and saliva delivers high accuracy for head and neck cancer diagnostics

Context: Here we focus on using conventional Raman applied to whole biofluid analysis prior to using more complex biomolecule subpopulations or the extension of SERS. We show strong ability to distinguish cancer from non-cancer from a simple data augmentation, providing support of the diagnostic potential Raman has as a clinical tool.

3.1 Introduction

When cancer is detected early, treatments are more effective, and survival improves. Current diagnostic modalities of imaging (e.g., ultrasound, CT, MRI, PET) and solid biopsy with pathology and immunohistochemistry are either invasive, time-consuming, or frequently inaccurate, therefore not ideal for routine screening of at-risk patients.[110] There is a critical need to develop rapid, inexpensive, and accurate new platforms that identify tumor associated features in circulating biofluids in the earliest stages. Liquid biomarkers—chemical analytes of interest present within a patient biofluid—could provide significant clinical and economic benefits, paving the way towards precision medicine and patient-centered care.[111]

It is unlikely that a single biomarker will detect all types of cancer or reliably inform clinical care throughout diagnosis and treatment; therefore, techniques capable of analyzing signatures representing a broad range of molecules are needed. Omics platforms based on mass spectrometry (MS), encompassing genomics, transcriptomics, proteomics, lipidomics, and metabolomics, have transformed our understanding of cancer molecular biology.[112–114] Yet such approaches are relatively slow, high in cost and complexity, low throughput, and require large sample volumes, thus are impractical for many stages of clinical care. These limitations are especially prohibitive for large scale routine cancer screening, thus there are huge advantages to moving towards diagnostic platforms that do not rely on MS.

Instead, an ideal diagnostic test would be rapid, real-time, reagent-free, non-destructive, inexpensive, highly accurate, and require minimal background training and minute amounts of minimally- or non-invasively collected sample (e.g., plasma, urine, or saliva). Raman spectroscopy (RS) addresses many of these needs: it requires little to no sample preparation, is non-destructive, does not need exogenous dyes or labelling agents, and can be performed directly in aqueous solutions.[115] RS has been applied to diagnose many cancers to date, including breast,[116] pancreatic,[117] skin,[118] colon,[119] gastric,[120] and lung cancer.[121] In head and neck cancer (HNC), prior applications mainly focused on tissue, either as a screening tool,[122,123] for identification of potential recurrence,[124] or general discrimination between normal and cancerous tissues.[125–132] But there is little work done using RS to identify and validate early-stage HNC liquid biomarkers, particularly comparing against benign disease or diagnostic staging. In addition, typical Raman research is carried out on smaller datasets which leads to over-fitting of data and misinterpretation.[133] When applied to larger cohorts, the sensitivity and specificity of such platforms typically drops due to increased complexity and inter-patient variation. These limitations have hindered the clinical adoption of Raman-based platforms.[134]

Of importance to note is that many studies related to cancer detection are carried out using surface-enhanced Raman scattering (SERS), a highly sensitive extension of Raman that uses nanoscale metallic features to induce a strong electromagnetic enhancement.[31,54,55,97,135] SERS has many of the same features mentioned above but measurements can be done more quickly with a stronger signal. However, SERS struggles with reproducibility due to inherent signal heterogeneity, making it difficult to validate the results obtained.[30] For this reason, we decided to utilize conventional Raman in this study.

RS is an attractive diagnostic tool, but there remain some obstacles that need to be addressed to maximize clinical translation potential. Typical Raman instruments tend to have a large physical

footprint. Efforts in producing miniaturized, portable systems are advancing, but it is not clear that their resolution would permit the diagnostic performance achieved in this study. Another drawback currently is the lack of automation for fast and easy measurements. Currently, RS requires highly trained users for sample measurement and data analysis. Furthermore, an accounting for the range of preanalytical variables that may affect measurement was not carried out in this work. It is not clear how diagnostic model performance would be affected by sample storage conditions, time of day for liquid biopsy collection, or total volumes collected (to name a few). Future work to address these pitfalls could increase the translational potential of RS as an indispensable clinical tool.

As of 2018, head and neck cancer (HNC) was the seventh most prevalent cancer worldwide with 890,000 new cases and 450,000 deaths.[3] Although cases linked with tobacco and alcohol use have been on the decline, cases of human papillomavirus (HPV)-associated HNC cancer are increasing, mainly induced by HPV.[136] Approximately 30-40% of patients are diagnosed with stage I or II HNC, which is typically curable with surgery or radiotherapy alone and increases long-term survival rates to 70-90% for those individuals.[137] However, this leaves more than 60% of patients with HNC presenting in stage III or IV, which carries a high risk of distant metastasis, local recurrence, and a 5-year overall survival of 50%.[104] It is evident from these reported numbers that HNC diagnosis could benefit from finding and validating early-stage biomarkers that can be correlated with the disease progression and further monitored to assess patient reaction to treatment.

Another interesting angle of this research involves the augmentation of data, in this case by combining the Raman spectra of multiple biofluids. More diagnostic information may be uncovered by creating these stitched biofluid datasets, leading to a potential increase in diagnostic ability of our platform. This type of low-level data combination has been utilized before in the context of assessing pollutants in oils,[138] clay minerals,[139] or analyzing the purity of red meats to uncover food fraud.[140,141] Some initial work applying Raman spectra concatenation has been applied to biological

samples, but this work was done by combining different types of data (in this case Raman and MALDI spectrometric imaging).[142] We believe this is the first time Raman data augmentation has been performed using multiple biofluid sources rather than analytical techniques.

In this study we carried out RS measurements of paired blood and saliva for a 53-person cohort. Using chemical standards of metabolites identified by MS on a subset of those patients, we confirmed that the spectral features upon which discrimination is based in RS are associated with the same biomolecules identified by MS. We determined optimal pre-analytical variables (e.g., native vs. dried biofluid) that maximized model performance. Our major finding is that accuracy, sensitivity, and specificity approaching, and even surpassing MS, could be achieved by RS using an innovative approach to stitch together spectra from plasma and saliva for each patient. To the best of our knowledge, this is the first study that uses RS to directly validate metabolites from patient biofluids, as well as to analyze combination biofluid spectra to achieve highly accurate diagnostic performance.

3.2 Mass spectrometry analysis

For the initial subset of 28 patients (19 SSC and 9 control cases) collected for this study, plasma and saliva biofluids for each patient were measured by gas chromatography – time of flight mass spectrometry (GC-TOF-MS) for primary and polar metabolite identification.[105] Metabolites grouped by structural class were ranked based on their fold-change in SSC vs. control samples (**Figure 3.1a**). The highest fold changes occur within distinct classes and differ widely between the two biofluid types. Saliva yielded more polarized data compared to plasma, with a higher number of metabolites featuring a significant fold change between cancer vs. benign controls. Nevertheless, both plasma and saliva each provided high diagnostic value when subjected to partial least-squares discriminant analysis (PLS-DA). The first two X-variates in the model yielded the best model performance. For plasma or saliva, this represented 20% of the total variance in each case. For each biofluid, only one sample was misclassified (**Figure 3.1b**). Receiver operating characteristic (ROC) curves were generated by plotting

the true positive rate against the false positive rate for plasma and saliva (**Figure 3.1c**). The area under curve (AUC) values were 95.9% for plasma and 92.4% for saliva. This was the highest reported AUC for GC-MS measurements of HNC plasma and saliva in the literature that we are aware of, with the next highest being 90.4%.[143,144]
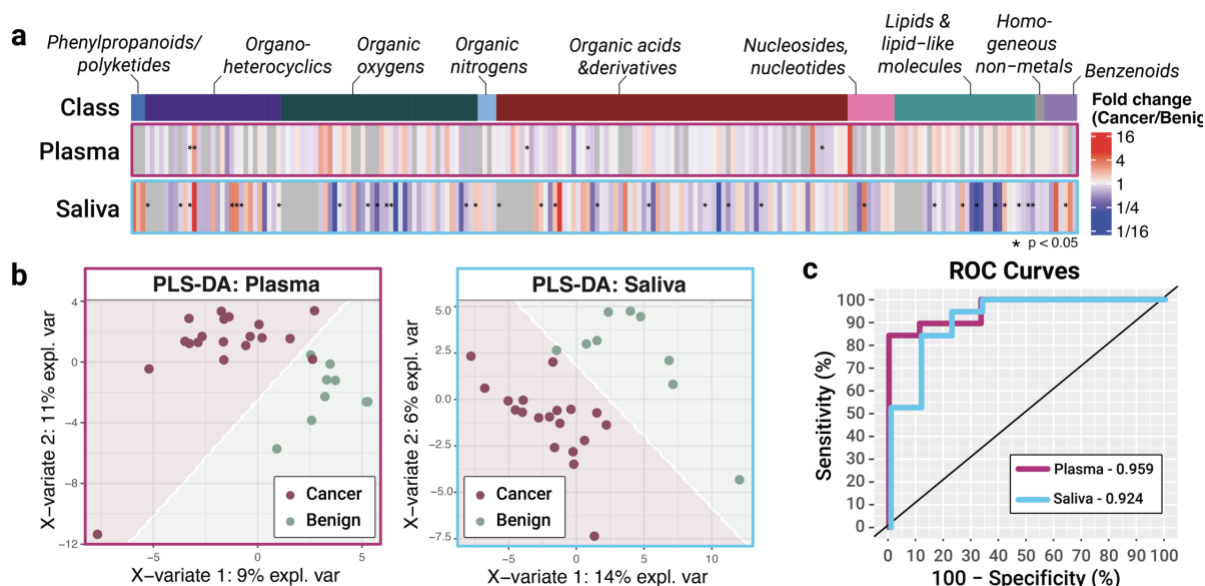
Figure 3.1: GS-TOF-MS analysis of plasma and saliva collected from SSC vs benign control cases. a) Metabolites grouped by chemical class were identified from either plasma (top) or saliva (bottom). Color scale represents fold change for cancer/benign, with red representing a higher prevalence in cancer biofluids and blue a higher prevalence in the controls. b) PLS-DA of the pre-labeled cancer and control samples for plasma and saliva reveals excellent discrimination with only a single sample misclassified in each biofluid. c) ROC curves enable calculation of AUC to be 95.9% and 92.4% for plasma and saliva, respectively.

To understand the main metabolic drivers of this diagnostic modeling, we generated similar AUC plots upon systematically removing the metabolites with lowest variable importance score in the PLS-DA model. We found that even using just the top five metabolites for each biofluid achieved AUC scores of 93.0% and 91.2% for plasma and saliva, respectively Supplemental Table S1. The identity and structure of these top five metabolites driving the diagnostic model performance are shown in **Table S3.2**.

3.3 Raman spectroscopic analysis

The full cohort of 53 subject samples was measured using a custom-built inverted Raman confocal microscope. Spectral averages for cancer vs benign control are shown in **Figure 3.2**. Spots were plotted together in a two-dimensional PC space for initial visual assessment. Measurements were taken in both a native (i.e., wet) and dried state, since it is not clear which would be most accurate for downstream diagnostic modeling. Native state measurements are quicker to prepare, yet the weak nature of spontaneous Raman scattering necessitates a moderately long acquisition time of 30 seconds in unconcentrated samples. During this time, metabolites are diffusing in and out of the focal volume, increasing sampling but also heterogeneity of the signal. On the other hand, drying out the samples under ambient conditions increased sample measurement time by 15 minutes to allow for drying, but concentrates the sample and results in a more stable spectra in the same 30 seconds. **Figure 3.2** plots the average and standard deviation of the Raman measurements for the two biofluids in both native and dried state.
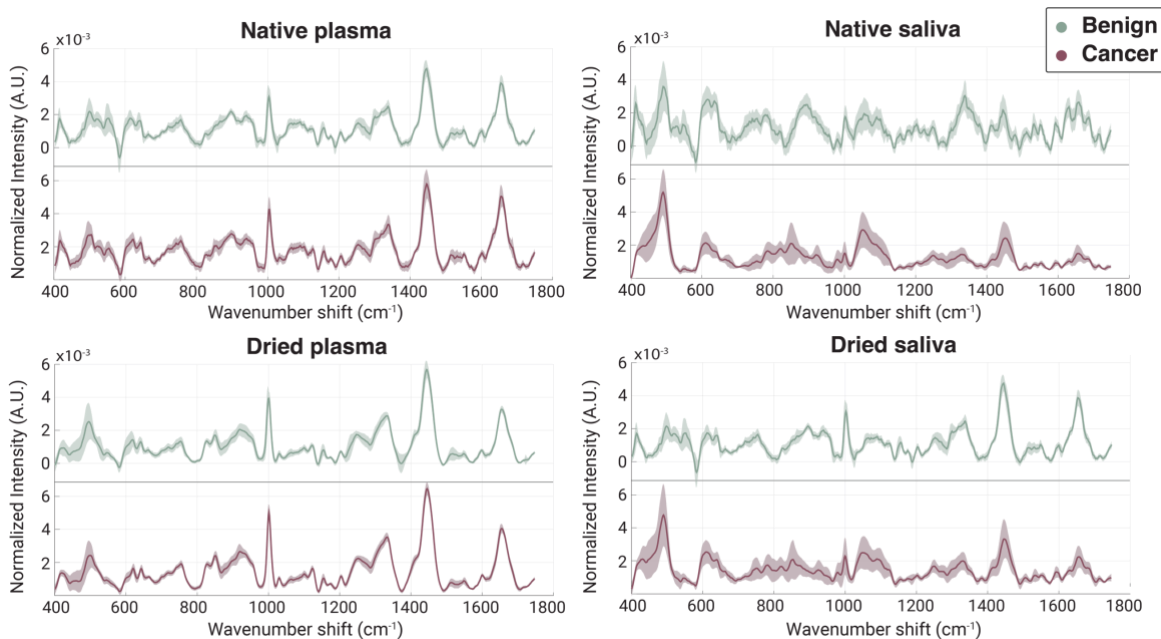
Figure 3.2: Global averages and standard deviations for cancerous samples (purple) and control samples (green) of plasma (left) and saliva (right) in both a native (top) and dried (bottom) state. The native samples had a higher degree of standard deviation from the dried samples, indicating there was more heterogeneity across sample measurements.

The dried measurements exhibit less intra- and inter-sample variation compared to the native samples, a trend that is particularly evident for saliva. Comparing dried and native saliva samples, we observed a large discrepancy in the peaks represented by the cancer versus the control group. Raman shifts in the vicinity of 1000 cm^{-1}, 1300 cm^{-1}, and 1650 cm^{-1} that correspond to key biological materials (**Table 3.1**) have higher intensity differences between cancer and control in the dried spectra. This indicates that some signals may be more prevalent in the dried state than the native, suggesting that the two methods are probing different chemical aspects of the samples.

3.4 Fitting Raman spectra with metabolite standards

Considering that Raman and metabolomics in principle evaluate similar chemical analytes comprising a given sample, we were interested to assess whether the same metabolites driving
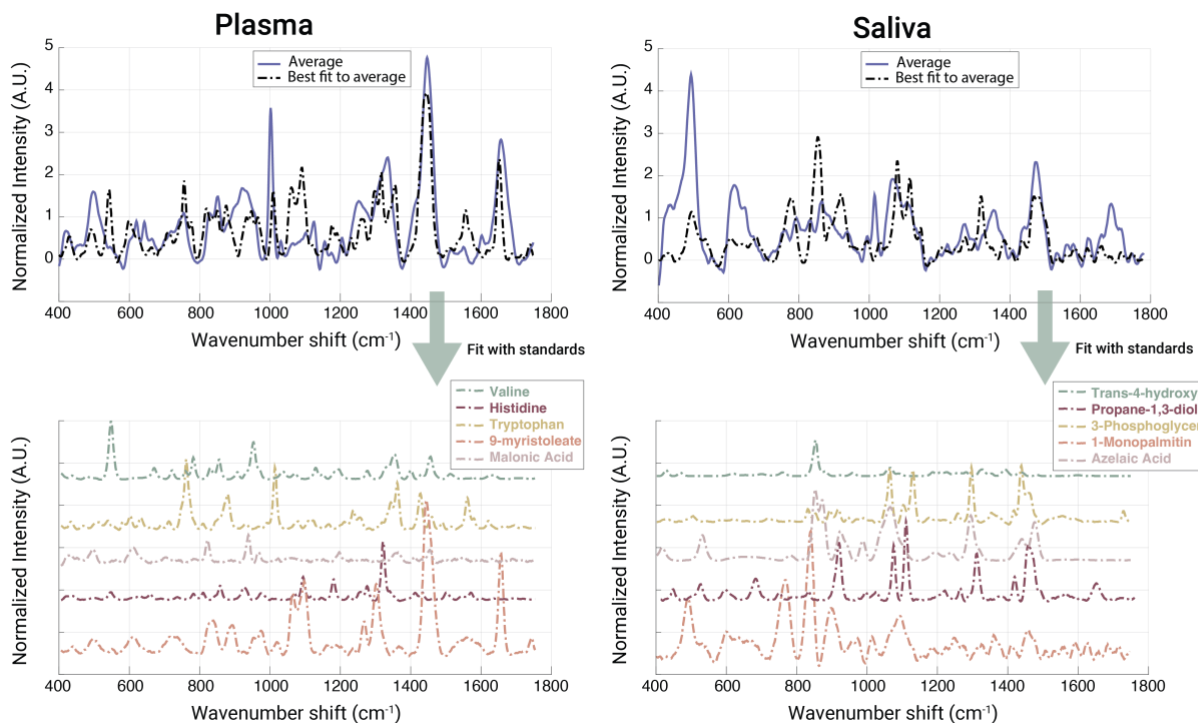
Figure 3.3: Raman spectra of cancer biofluids contain distinct features that can be attributed to the metabolites identified by GC-MS to drive diagnostic model performance. For each biofluid, average spectra of the cancer samples were fit with their respective metabolites. The average plasma cluster for cancer patients (blue) was fit with the reference spectra below for valine (green), histidine (magenta), tryptophan (yellow), 9-myristoleate (orange), and malonic acid (rose). The average saliva cluster for cancer patients (blue) was fit with the reference spectra below for trans-4-hydroxyproline (green), propane-1,3-diol (magenta), 3-phosphoglycerate (yellow), 1-monopalmitin (orange), and azelaic acid (rose).

metabolomics model performance could also be measured in RS. For the ten metabolites shown in **Table S3.2**, analytical standards were obtained and measured by RS. Each metabolite was strongly Raman active and showed a distinct spectral signature (representative spectra are shown in **Figure S3.2**.)

To assess their relevance in relation to the Raman data of saliva and plasma, cluster fitting was performed. Principle component analysis (PCA) of all cancer samples for plasma and saliva was carried out. Hierarchical clustering was applied using Euclidean distance metrics considering the top five principal components. The spectra average for the cancer samples was fit (using asymmetric least squares) to combinations of the metabolite standard spectra to assess the extent of which each metabolite contributed to the complex spectra measured for each whole biofluid (**Figure 3.3**). The average spectra for non-cancer samples were also analyzed using the same method but showed a much poorer fit with the metabolite standards, as shown by **Figure S3.3**. A significant number of features could be attributed to the metabolites driving the MS model performance, as observed in the Raman average spectra. More specifically, certain spectral features from the metabolite standards had strong fittings with peaks seen in the biofluid spectra. For plasma, the main peaks seen at 1450 cm^{-1} and 1650 cm^{-1} correlate well with the main spectral features of 9-myristoleate. The prominent peak at 1005 cm^{-1} can be attributed to tryptophan. Finally, the spectral feature at 1360 cm^{-1} in valine is also apparent in the cancer spectra. For saliva, the 1450 cm^{-1} shift can be attributed to propane-1,3-diol. The peaks seen at 1045 cm^{-1} and 1091 cm^{-1} fit strongly with features present in azelaic acid, 3-phosphoglycerate, and 1-monopalmitin. Finally, there is good agreement between the peak and the spectral feature seen at 491 cm^{-1} in 1-monopalmitin. Prominent distinct features can be therefore attributed to the various metabolite standards.

In other words, the top five metabolites for each biofluid are more prevalent in the cancer samples than the control samples, indicating that there is good correlation of diagnostic information

between the metabolomics and Raman data. It is important to note that the fitting of these metabolites did not account for all spectral variability in either biofluid measurement. For example, in the plasma spectra there was poor fitting at 500 cm^{-1} and 1250 cm^{-1}. For saliva, we can see peaks at 615 cm^{-1}, 1001 cm^{-1}, 1332 cm^{-1}, and 1660 cm^{-1} that do not obviously match with the top metabolite standards. While it is apparent that the complex RS spectra contains signatures of the targeted metabolites, much more information is additionally present.

3.4 Diagnostic model performance using Raman Spectroscopy

We aimed to assess the ability of spontaneous RS platform to distinguish cancer from control samples in either plasma or saliva samples collected from each subject. Data stacks were generated with all collected spectra (i.e., 5 spots averaged across native and dried saliva or plasma for all 53 study subjects). A representative average plus standard deviation for the dried plasma and saliva samples are shown in **Figure 3.4a** and **Figure 3.4e** respectively. Unsupervised PCA was carried out for each sample typed (e.g., native plasma, dried saliva). Each PC spectrum represents a spectral loading that encompasses a certain amount of the total variation across samples; PC1 has the features responsible for the highest level of variation and each subsequent PC has fewer weight than the previous. The spectral loadings for the first three PCs for the dried plasma and saliva RS measurements are plotted in **Figure 3.4b** and **Figure 3.4f** respectively. Individual patient spectral averages can be re-plotted in PC space (**Figure 3.4c** and **Figure 3.4g**), enabling visualization of supervised data modeling via linear or quadratic discriminant analysis (LDA/QDA). Supervision (i.e., cancer vs benign control) labels were applied based on clinical diagnosis using histopathology analysis. For each sample type, a custom algorithm was run to find the specific flavor of LDA/QDA classifier (using built-in MATLAB classes without hyperparameter optimization) over every combination of the first five PCs (PC1-PC5), which represented 82.5% and 89.7% of the total sample's variance for plasma and saliva, respectively. For dried plasma, for example, the "linear" discriminant type over PCs 1-3 yielded the highest accuracy,

sensitivity, and specificity. The shape of that classifier (reduced to dimensions 1,2, and 3) is shown in

Figure 3.4c. Misclassified patients are labeled in yellow. The true (clinician labeled) class vs the RS

predicted class in 2x2 boxes were used to calculate sensitivity, specificity, and accuracy of the model

(**Figure 3.4d** and **Figure 3.4h)**. The sensitivities, specificities, and accuracies for dry plasma and saliva

were found to be 78.1%, 81.8%, and 78.8%, and 72.1%, 70%, and 71.7% respectively. For native saliva

and plasma, the sensitivities, specificities, and accuracies were 82.8%, 58.3%, and 71.7%, and 78.6%,
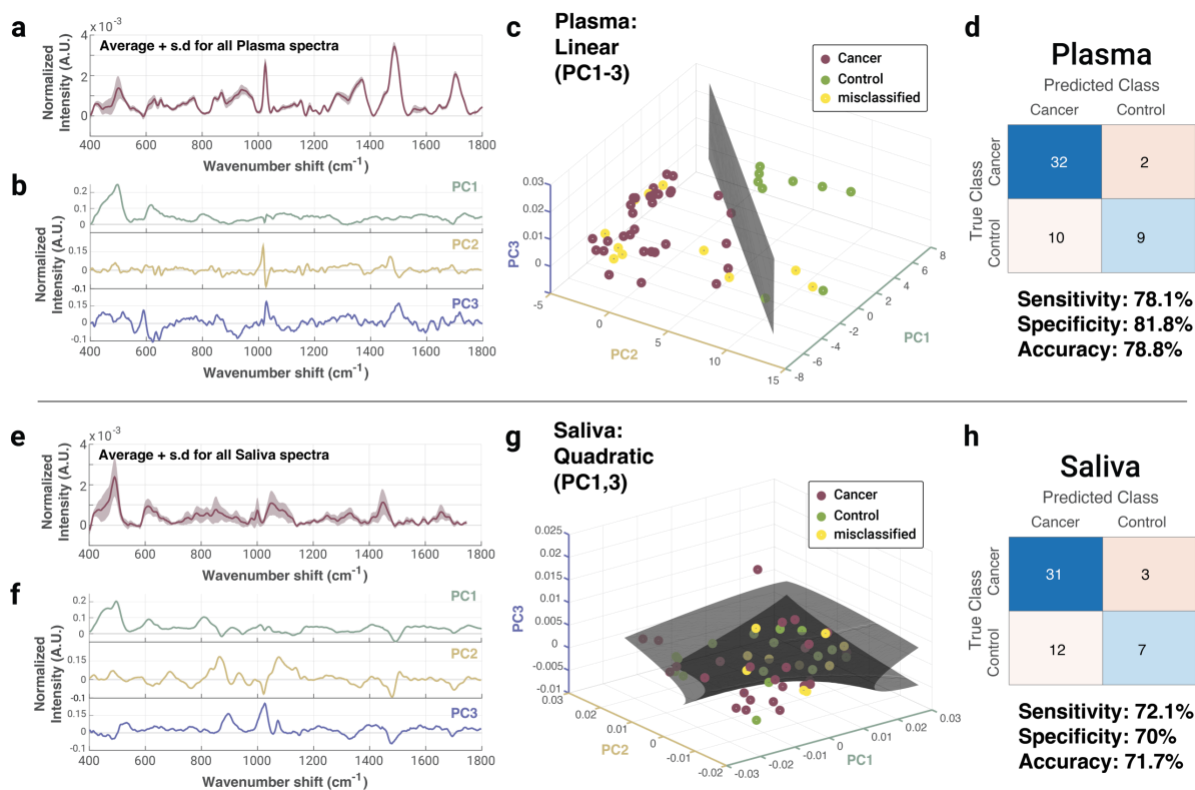
Figure 3.4: Representative spontaneous Raman data for dried plasma and saliva samples. a) Average spectra and standard deviation for all plasma measurements are plotted. b) Principal component (PC) loadings for PCs 1, 2, and 3 show the major spectral variations amongst the samples. c) The plane of best separation following LDA/QDA algorithm optimization, with cancer (magenta dots) moderately separated from control (green dots) and several misclassified samples (yellow dots). d) 2x2 table generated from the best classifier and their associated sensitivity, specificity, and accuracy. e) Average spectra and standard deviation for all saliva measurements are plotted. f) Principal component (PC) loadings for PCs 1, 2, and 3 show the major spectral variations amongst the samples. g) The plane of best separation following LDA/QDA algorithm optimization, with cancer (magenta dots) moderately separated from control (green dots) and several misclassified samples (yellow dots). h) 2x2 table generated from the best classifier and their associated sensitivity, specificity, and accuracy. Plasma analysis yielded higher diagnostic capabilities but overall the technical performance was only moderate.

90.1%, and 81.1% respectively. More detailed information about the groups and the classifiers used for each can be found in supplementary **Table S3**.

Although plasma outperformed saliva in separating cancer from non-cancer, both biofluid groupings had lower diagnostic capability than the metabolomics results showed. We were then curious to see if simple data augmentation methods could improve performance. Therefore, we stitched average spectra across both biofluids together for each patient to create a single unified spectrum. The intensity values from the saliva samples were copied and added to the backend of the plasma samples to create these new combined biofluid spectra. X-axis values were reassigned as arbitrary numbers from 1 to 1694 (the horizontal CCD pixels doubled after merging the data together). For each of the 53-subject cohort (34 HNC cancer patients and 19 benign controls), the same procedure of averaging each spot to produce one spectrum per patient was followed and the samples were once again projected into the PC space to create a stack with the PC1-5 associated values. The global averages and standard deviations of this new group for all dried samples is shown in **Figure 3.5a** with the first three PC loadings shown in **Figure 3.5b**. With the best classifier (quadratic with PC 1-5), we achieved a remarkable sensitivity, specificity, and accuracy of 96.3%, 85.7%, and 91.7% (**Figure 3.5c**). The sensitivity vs. 1-specificity for all groups (both native and dried, single biofluid and combined biofluid) are presented in **Figure 3.5e**. As evidenced by this graph, the saliva alone tends to have better performance than the plasma when analyzed individually, but the performance of the plasma and saliva combined is superior to the individual biofluid groups. These combined biofluids give diagnostic ability on par with the metabolomics results, supporting our Raman system, combined with simple data augmentation, as a strong diagnostic approach.

Identification of the spectral features driving model performance is a powerful way to glean deeper chemical information from samples. To investigate what chemical entities were the highest drivers of spectral importance, we created a representative composite spectrum of the combined

plasma and saliva specimens by averaging all the cancer and control samples and then calculating the difference. The resulting spectrum is shown in **Figure 3.5d** with the most influential peaks labelled. The saliva section of the combined spectrum contained far more meaningful peaks than the plasma section. We further analyzed the chemical signatures associated with each peak using the tentative assignments shown in **Table 3.1**. Although efforts to assign the vibrational peaks prominent in the spectrum have been made, we caution against overinterpretation of single spectral peaks. Instead, we consider the significance of major groupings of distinct feature types such as carbohydrates, proteins, lipids, or nucleic acids.
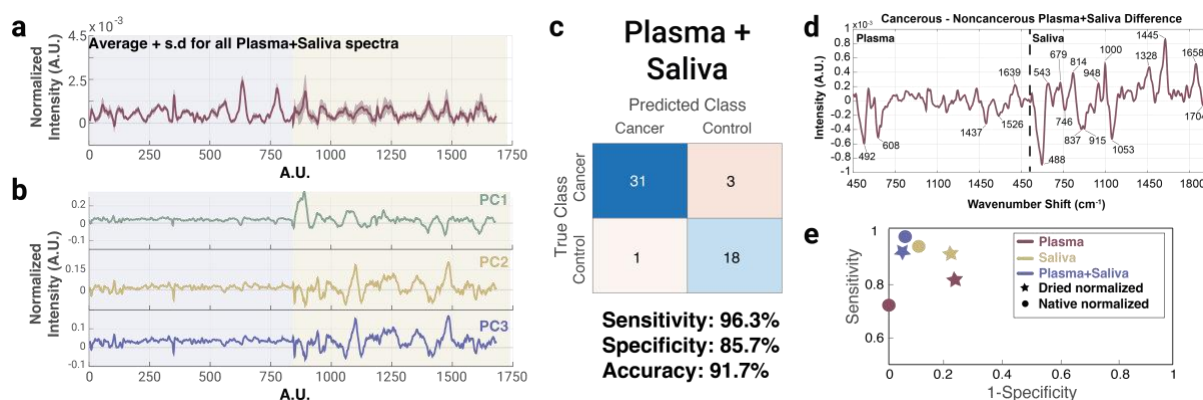
Figure 3.5: Representative spontaneous Raman data for combined plasma and saliva dried samples. a) Global average and standard deviation of the plasma and saliva combined spectra. The blue overlay represents the portion of the spectra that is plasma, and the gold overlay represents the portion that is saliva. b) Principal component (PC) loadings for the first three PCs showing the different areas of variation between the plotted samples. c) 2x2 table created using the Quadratic PC1-5 classifier to assess sensitivity, specificity, and accuracy, of which were 96.3%, 85.7%, and 91.7% in this group. d) Spectrum representing the peaks obtained from subtracting the average control spectrum from the average cancer spectrum for combined plasma and saliva. Important spectral features were identified and labelled. e) Plot of all combinations (native and dried, combined and individual) sensitives vs. 1-specificity. The combined biofluids outperformed the single biofluids for most of the categories.

The majority of the peaks identified in the plasma portion (e.g. 492 cm⁻¹, 608 cm⁻¹, 1437 cm⁻¹, and 1526 cm⁻¹) correspond to protein vibrational modes. Further, all besides one are negative which indicates these protein signatures are more commonly seen in the non-cancerous samples than the cancerous ones. This indicates that important distinct differences between the two sample types are reflected in protein composition. This notion is further supported when reflecting back to the top five metabolites identified for plasma from the GC-MS measurements. Of the five, three are amino acids,

the building blocks of proteins and only one comes from a class associated with lipids, strengthening the idea that protein content is generally driving the differences between the cancer and control samples. We also identified the peaks that can be attributed to the metabolites themselves. For example, the best fit to the average line shown in **Figure 3.3** (which contains all five metabolites together) reflects key protein peaks at 492 cm^{-1}, 1437 cm^{-1}, and cm^{-1}. Two distinct peaks from tryptophan (877 cm^{-1} [93], and 1556 cm^{-1} [145]) are present in the fitting spectra but not in the plasma section of the stitched data. There were also peaks at 602 cm^{-1} [97], 1060 cm^{-1} [146], 1090 cm^{-1} [145], and 1179 cm^{-1} [147] that are contributing to C-C stretches in lipids and proteins. These absence of these peaks in **Figure 3.5d** indicates they did not play a strong diagnostic role after the biofluid stitching procedure was complete.

Table 3.1: Raman peaks of interest with characteristics in cancer samples (increased or decreased), with assigned functional groups

Peak/band (cm^{-1})	Cancer	Chemical Assignment
492	-	S-S stretch[148]
608	-	CH$_2$ twist[149]
1437	-	CH$_2$ bending in proteins and lipids[93,150]
1526	-	C-N stretching, Amide II[151]
1639	+	Amide I C=O stretching vibrations in proteins[93,97]
488	-	Glycogen[146]
543	+	S-S disulfide bridges in cysteine[151]
679	+	Guanine ring breathing[148]
746	-	C-S aliphatic stretching, Thymine[152]
814	+	Phosphodiester bands[153]
837	-	Amino acids, sugars, and nucleic acids[154]
915	-	Carbohydrate-related SERS vibrations[155]
948	+	C-C, alpha-helix[152]
1000	+	Symmetric ring breathing mode of phenylalanine[153]
1053	-	C-C stretch lipids[146]
1328	+	Amide III—collagen[146]
1445	+	CH$_2$ and CH$_3$ deformations in proteins and lipids[93,150]
1658	+	Amide I (C=O stretching of proteins)/C=C lipid stretch[93,150]
1704	-	Amide I[151]

In the saliva section of the composite spectrum, we also observed notable chemical groupings. Strong signals at 543 cm^{-1} (S-S disulfide bridges in cysteine), 679 cm^{-1} (guanine ring breathing), 1000 cm^{-1} (symmetric ring breathing in phenylalanine) and 1445 cm^{-1} (CH2 and CH3 deformations in

proteins) are seen with positive values, once again aligned with the idea that the protein profile of cancer and control samples differ widely. Peaks are 746 cm^{-1} (C-S aliphatic stretching) and 1053 cm^{-1} (C-C stretch in lipids) speak to the general lipid profile and are negative, indicating their commonality in the non-cancerous spectra. Taken together the positive protein and negative lipid peaks may demonstrate the necessity to analyze general ratios of these components present in future samples. Once again there were analogous peaks between those identified above and the average fitting spectra from the saliva metabolites shown in **Figure 3.3**, including 543 cm^{-1}, 837 cm^{-1}, 1053 cm^{-1}, and 1445 cm^{-1}. However, we similarly observe a rise of peaks specific to the fitting spectra that did not appear in the stitched data. These were 774 cm^{-1} (nucleic acids)[145] , 845 cm^{-1} (polysaccharides)[145], 908 cm^{-1} (skeletal C-C in lipids)[149], 1100 cm^{-1} (C-C stretch in lipids)[151], and 1296 cm^{-1} (fatty acids)[145]. These results indicate that specific features of the metabolites are helping identify the cancerous samples more directly than others and serve as the potential chemical drivers contained within the diagnostic information.

Perhaps the most interesting thing to note is the exceptionally negative peak at 488 cm^{-1}. This peak is associated with glycogen, a polysaccharide that serves as a main form of energy storage. The negative value here argues that this peak is very prominent in non-cancerous samples but not cancerous ones. This is interesting to see considering cancer cells undergo aerobic glycolysis (referred to as the Warburg effect) to promote rapid and continuous growth. Human Papilloma Virus (HPV) is a large mediator of new HNC cancers, and there are many associated HPV proteins that activate specific proteins or pathways within the body to assist in the switch to aerobic glycolysis. These include epidermal growth factor receptor (EGFR), protein complex mTORC2, and the retinoblastoma protein (Rb).[156] Interestingly, it has been shown that when HPV viral proteins interact with these groups, the level of glycogen present drastically decreases.[156] This in combination with the fact that

the glycogen peak presents as negative in the composite spectrum support the notion that glycogen signal could be a strong diagnostic indicator.

Within the cohort of cancer patient samples, we attempted to carry out discrimination of cancer staging, i.e., split into two groups of early (stage I/II) vs late (stage III/IV), as assessed by the clinician. But the performance of our models was poor. In future work with a higher number of samples in each category, we will apply more sophisticated data models to try to elucidate stage-based discrimination. While we did not perform SERS in this study, this may be a future area of interest where stitching data across biofluids could improve performance metrics.

3.5 Discussion

The accuracy of HNC diagnostics using Raman spectroscopy is highlighted in several recent works. In direct analysis of whole tissues, Jeng, et. al reported an accuracy of 81.25%, sensitivity of 77.27%, and specificity of 86.11% for discrimination of cancerous versus healthy samples on a cohort of 80 total patients.[126] Yan, et al was able to increase these numbers to the high 90s through implementation of a machine learning algorithm, albeit on a small dataset of only 12 patient samples.[132] A systematic review of using Raman for oral cancer diagnostics by Zhan, et al also describes a meta-analysis of 41 articles, citing that the accuracy of RS in oral cancer diagnostics on in vitro frozen tissues as 99.68%.[131] Although these are impressive numbers, the clinical relevance for diagnostics is lacking, as these studies do not address the need to create fast, non-invasive liquid biopsy approaches for rapid diagnostics. Another group performed RS measurements on HNC saliva samples from a cohort of 32 patients with accuracy of 90%, which was lower than the numbers reported from the groups analyzing tissue but still clinically useful.[130] Our stitched biofluid accuracy, sensitivity, and specificity slightly outperforms that study across a much large patient cohort.

Recent reviews have investigated the application of metabolomics to HNC diagnostics and provide a thoughtful summary of where the field stands.[157,158] Metabolomics analysis of HNC has

been carried out in many different biofluids ranging between urine[159] to serum[160–163] to saliva.[164–167] Saliva as a biofluid source is of interest for many reasons: first, it is non-invasive and easily obtained from patients; second, low volumes are needed for metabolomic analysis, and third, the close proximity saliva has to the HNC tumors may provide additional biomarker information and contain a higher level of cancer metabolites of interest. Although a few studies have been carried out that show saliva contains important features that can distinguish cancer from non-cancer, there is little agreement of which metabolites are important when comparing the results across studies. Furthermore, the dynamic nature of saliva and contamination from recent diet may pose issues for accurate detection of tumor biomarkers. Few studies have been carried out using RS directly on saliva from HNC samples.[130,168,169] The studies that have been conducted are diverse in their methodologies and results, making it hard to provide concrete evidence that RS analysis of saliva is a viable diagnostic tool. Further, there are many variables that influence the profile of saliva collected from patients, including age,[170] smoking habits,[171] time of day,[172,173] fasting regimen,[173] and gender.[170] Controlling for all of these factors is necessary for clinical adaptation.

Bringing RS into the clinic is attractive for many reasons. RS can be performed in aqueous solutions without the interference of a water signal that can hinder other spectroscopic techniques such as infrared spectroscopy. Collection and separation of biofluids from patients undergoing treatment is common and being able to perform point-of-care measurements directly on those biofluids in near real time creates an obvious advantage for RS systems. Metabolomics remains the gold standard for biomarker discovery due to its ability to develop rich chemical data libraries.[114] However, there are drawbacks to using this technology as the main tool for such investigation. Perhaps the most vital drawback is the challenge of validating the identified metabolites robustly across many datasets. The analysis of samples and production of results may be relatively straightforward, but the potential biomarkers cannot be used unless they are rigorously validated to report on the disease state.

By combining each patient's Raman data from their plasma and saliva samples into a single spectrum, we dramatically improved the diagnostic value of spontaneous RS, a key finding of this study. These data indicate that future work should focus on the development of methods that can provide a more comprehensive view of the physiological state of an individual's health. Further, we showed that the same metabolites identified as driving diagnostic model performance in GC-MS could be correlated by RS performed in the very same samples, providing a level of validation that many other technologies lack. Our findings validate that RS is inherently measuring a similar subset of metabolites compared to GC-MS, confirming them as promising biomarkers for HNC. Yet is also establishes that the spectral features themselves, divorced of assignment to any particular metabolite species (and their concentrations) are highly capable of driving accurate diagnostics. Although RS, even for the combined biofluid data augmentation, performed slightly worse in terms of accuracy compared to GC-MS, RS is comparatively easier, quicker, uses less sample volume, is non-destructive, requires minimal sample prep, and is more inexpensive to carry out.

3.6 Supplemental Information

Table S3.1: Clinical biofluid information with demographics data for each patient

Patient ID	Plasma	Saliva	Diagnosis	Gender	Age
OD-0272	X	X	Cancer	Male	73
OD-0275	X	X	Cancer	Male	86
OD-0276	X	X	Cancer	Male	63
OD-0277	X	X	Non-cancer	Male	30
OD-0278	X	X	Non-cancer	Male	27
OD-0279	X	X	Cancer	Male	28
OD-0280	X	X	Cancer	Male	66
OD-0281	X	X	Non-cancer	Female	43
OD-0284	X	X	Cancer	Male	53
OD-0286	X	X	Non-cancer	Male	63
OD-0287	X	X	Cancer	Male	72
OD-0288	X	X	Non-cancer	Female	31
OD-0289	X	X	Cancer	Female	74
OD-0291	X	X	Non-cancer	Male	72
OD-0292	X	X	Cancer	Male	51
OD-0293	X	X	Non-cancer	Male	50
OD-0294	X	X	Non-cancer	Female	44
OD-0295	X	X	Cancer	Female	71
OD-0296	X	X	Cancer	Male	66
OD-0297	X	X	Cancer	Male	77
OD-0298	X	X	Cancer	Male	81
OD-0300	X	X	Cancer	Male	79
OD-0301	X	X	Cancer	Male	57
OD-0302	X	X	Non-cancer	Female	70
OD-0304	X	X	Cancer	Male	67
OD-0305	X	X	Cancer	Male	58
OD-0306	X	X	Cancer	Male	56
OD-0310	X	X	Cancer	Male	65
OD-0312	X	X	Cancer	Male	63
OD-0313	X	X	Cancer	Male	64
OD-0314	X	X	Cancer	Male	57
OD-0315	X	X	Cancer	Female	72
OD-0316	X	X	Cancer	Male	65
OD-0318	X	X	Cancer	Female	78
OD-0319	X	X	Cancer	Female	62
OD-0320	X	X	Cancer	Male	54
OD-0321	X	X	Non-cancer	Female	47
OD-0322	X	X	Cancer	Male	69
OD-0323	X	X	Cancer	Female	78
OD-0324	X	X	Cancer	Male	57
OD-0326	X	X	Non-cancer	Female	58
OD-0327	X	X	Cancer	Male	61
OD-0328	X	X	Cancer	Female	71
OD-0329	X	X	Cancer	Female	72
OD-0330	X	X	Cancer	Female	30
OD-0331	X	X	Cancer	Male	76
OD-0334	X	X	Cancer	Male	67
OD-0336	X	X	Non-cancer	Female	66
OD-0337	X	X	Non-cancer	Female	58
OD-0339	X	X	Non-cancer	Male	65
OD-0340	X	X	Non-cancer	Male	29
OD-0341	X	X	Non-cancer	Female	57
OD-0342	X	X	Non-cancer	Male	37
OD-0345	X	X	Non-cancer	Male	34
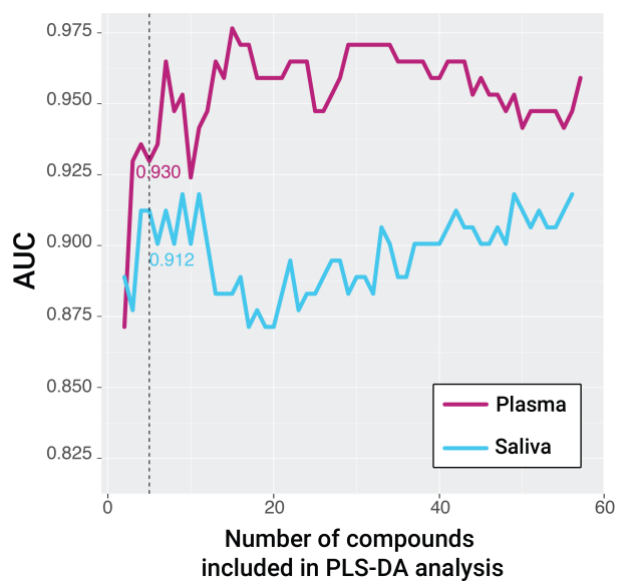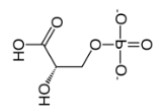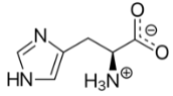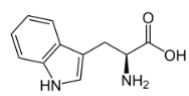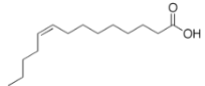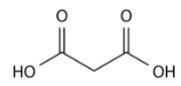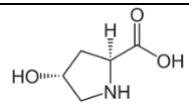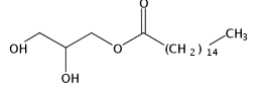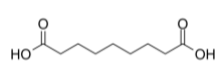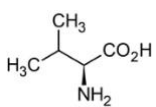
Figure S3.1: Area under curve (AUC) values with increasing number of metabolites as detected by GC-TOF-MS included in the PLS-DA model according to variable importance score for plasma (purple line) and saliva (blue line). The dotted black line indicates the AUC values for the PLS-DA model incorporating the top 5 metabolites for each biofluid, with their corresponding AUC values labeled.

Table S3.2: Top five metabolites identified by variable importance score in the PLS-DA model for cancer vs control in both plasma and saliva

Biofluid	Metabolite	Class	Structure
Saliva	trans-4-hydroxyproline	Organic acids and derivatives	
	propane-1,3-diol	Organic oxygen compounds	
	3-phosphoglycerate	Organic oxygen compounds	
	1-monopalmitin	Lipids and lipid-like molecules	
	azelaic acid	Lipids and lipid-like molecules	
Plasma	valine	Organic acids and derivatives	
	histidine	Organic acids and derivatives	
	tryptophan	Organoheterocyclic compounds	
	9-myristoleate	Lipids and lipid-like molecules	
	malonic acid	Organic acids and derivatives	
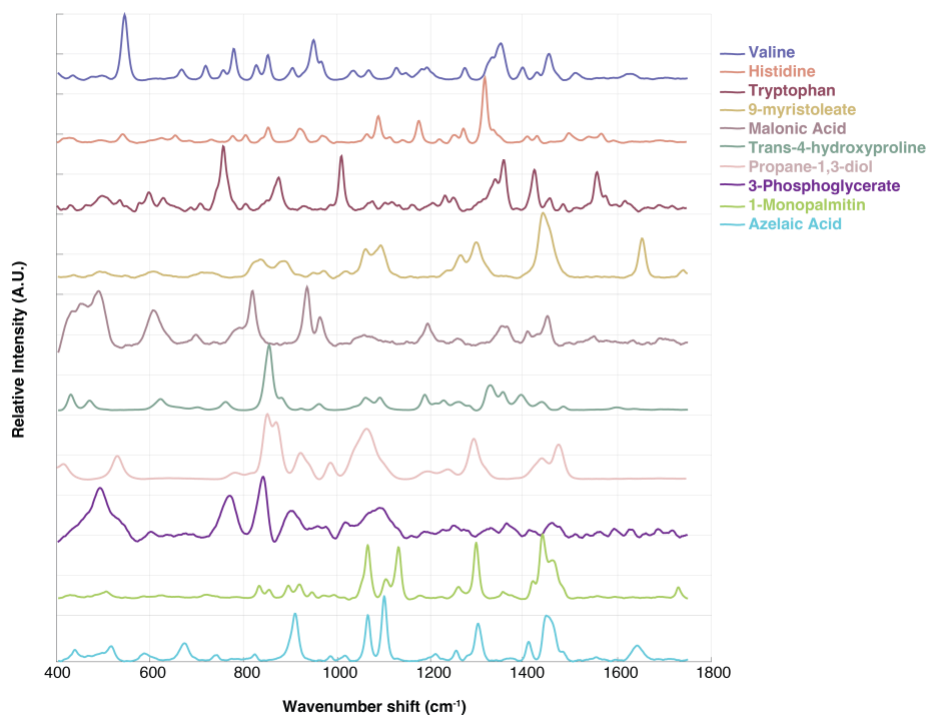
Figure S3.2: Raman spectra of the ten metabolites identified from GS-TOF-MS measurements grouped by their identification in PLS-DA models from either plasma (top five) or saliva (bottom five). Within each group, they are listed in order from most prevalent to least with respect to their variable importance score in the PLS-DA model. Valine, histidine, tryptophan, 9-myristoleate, and malonic acid were identified from plasma and trans-4-hydroxyproline, propane-1,3-diol, 3-phsophoglycerate, 1-monopalmitin, and azelaic acid were identified from saliva.

Table S3.3: The biofluid group along with the best identified classifier, and the accompanying accuracy, sensitivity, and specificity achieved with it.

Group	Best Classifier	Accuracy, Sensitivity, and Specificity
Dry Plasma	1,2,3 Linear	78.8%, 78.1%, 81.8%
Native Plasma	1,2,3,5 Quadratic	81.1%, 78.6%, 90.1%
Dry Saliva	2,5 Diagquadratic	71.7%, 72.1%, 70%
Native Saliva	1,3,4 Quadratic	71.7%, 82.8%, 58.3%
Dry Combined	1,3,4,5 Quadratic	86.3%, 90.3%, 80%
Native Combined	1,2,3,4,5 Quadratic	91.7%, 96.3%, 85.7%

3.7 Conclusions

In this study, we analyzed a robust clinical dataset of 51 HNC patient and benign control liquid biopsy samples to classify disease. Metabolomics measurements were performed using GC-MS as a

gold standard of comparison. GC-MS results yielded a 95.9% and 92.4% cancer vs. control discrimination using PLS-DA. The top five metabolites identified for each biofluid were further studied using our custom Raman scope. We found that the prevalence of these metabolites was higher in all cancer samples versus the control, validating that RS is inherently sensitive to the same metabolites driving excellent GC-MS model performance. We further tested the ability of our Raman platform to separate cancer from control within the individual biofluids. With a pseudoquadratic classifier we achieved sensitivities and specificities in the 70-90% range. Instead, with simple data augmentation to stitch plasma and saliva datasets together to create a single, integrated spectrum, sensitivity, specificity, and accuracy increased to 96.3%, 85.7%, and 91.7%. The results of this study indicate an exciting step in validating Raman spectroscopy as a robust diagnostic tool, as well as introducing a new finding that a holistic view of an individual's sample (in this case, a combination of their plasma and saliva) can provide a greater level of information indicative of specific disease states.

Chapter 4: Hybrid Nanoplasmonic Porous Biomaterial Scaffold for Liquid Biopsy Diagnostics Using Extracellular Vesicles

Context: Here we use SERS to investigate a more targeted biomolecule population of EVs to research their ability to reflect the disease state and provide a snapshot of the patient's health. We were able to decipher important chemical features present specifically in the glycocalyx that allow for good separation of cancerous and non-cancerous samples in the context of ovarian cancer.

4.1 Introduction

It is estimated that by 2025, over 20 million new cancer cases will be annually diagnosed.[174,175] While early-stage diagnosis leads to measurably improved patient outcomes, tumor heterogeneity and transformability are large obstacles. Tissue biopsies are the current gold standard for cancer diagnosis yet are invasive, often fail to capture tumor heterogeneity, are incapable of assessing small and hard-to-reach tumors or ones that have metastatically spread, and risk propagating the tumor to adjacent tissues.[176,177] Liquid biopsy entails the detection of tumor-associated biological material in circulating biofluids, including circulating tumor cells (CTCs), circulating tumor nucleic acids (ctDNA/ctRNA), tumor-educated platelets (TEPs), small molecular products of tumor metabolism, circulating tumor-derived proteins, and more recently, extracellular vesicles (EVs).[178–182]

EVs are lipid-bilayer enveloped nanoscale assemblies (from ~30 - hundreds of nanometer in diameter) that traffic bioactive molecules including nucleic acids, proteins, lipids, carbohydrates, and metabolites and related small molecules.[65,183] They are heavily implicated as mediators of cardiovascular and metabolic diseases, inflammatory diseases, neurological disorders (e.g. Alzheimer's disease), and cancer.[184,185] While EVs are released from cells in both normal and diseased states, it is clear that cancer cells exploit these signaling routes to dispatch EVs that promote tumor

progression in the local microenvironment as well as for metastatic purposes, including via the formation of a pre-metastatic niche.[81,186,187] Tracking tumor associated EVs aberrations in the biochemical landscape of body fluids can unveil the presence of cancer, recurrence, relapse and drug resistance.[188] In ovarian cancer (OvCa), a significant number of EV-trafficked proteins have been reported to correlate with cancer type and staging.[95,189,190]

Despite this limited success, liquid biopsy-based EV diagnostics are largely impeded by the high number of off-target healthy EVs present in all biofluids. Many analytical tools have been applied to EV-based liquid biopsies including Western blots, nanoparticle tracking analysis (NTA), flow cytometry, and direct fluorescence imaging techniques via antibody or aptamer labeling. However, these approaches often require tedious preanalytical isolation and large sample volumes, are lacking in throughput and multiplexibility, and are not cost-effective. An attractive solution to overcome these limitations is label-free analysis using chemical spectroscopy, such as Raman scattering. This technique provides global chemical composition of EVs and has been recently used to elucidate key differences between cancerous and non-cancerous EVs.[93,95,145,191–194] To address the weak nature of Raman scattering, surface-enhanced Raman scattering (SERS) can be employed via the use of plasmonic substrates or particles.[195–197] We have recently reviewed the application of nanoplasmonics to detect and analyze EVs.[87] SERS in particular is very attractive for liquid biopsies, given that it is label-free, exhibits unprecedented and highly tunable sensitivity and specificity, and has the potential for automation, miniaturization, and integration with microfluidics and machine learning.[61,87,198]

In this report we employ a new type of inexpensive, biocompatible plasmonic substrate integrating the benefits of a novel biosilicate material embedded with silver NPs (AgNPs) for use in label-free liquid biopsy of OvCa EVs (schematized in **Figure 4.1**). We use multivariate data analysis to extract relevant features among spectral sets that distinguish tumor samples from controls in *in vitro*

cell derived EVs and also clinical human serum samples from patients suspected of OvCa. We further explore cysteamine functionalization of AgNPs for non-specific recruitment of EVs to the substrate and chemical treatment of EVs to modulate their localization at the plasmonic AgNPs.
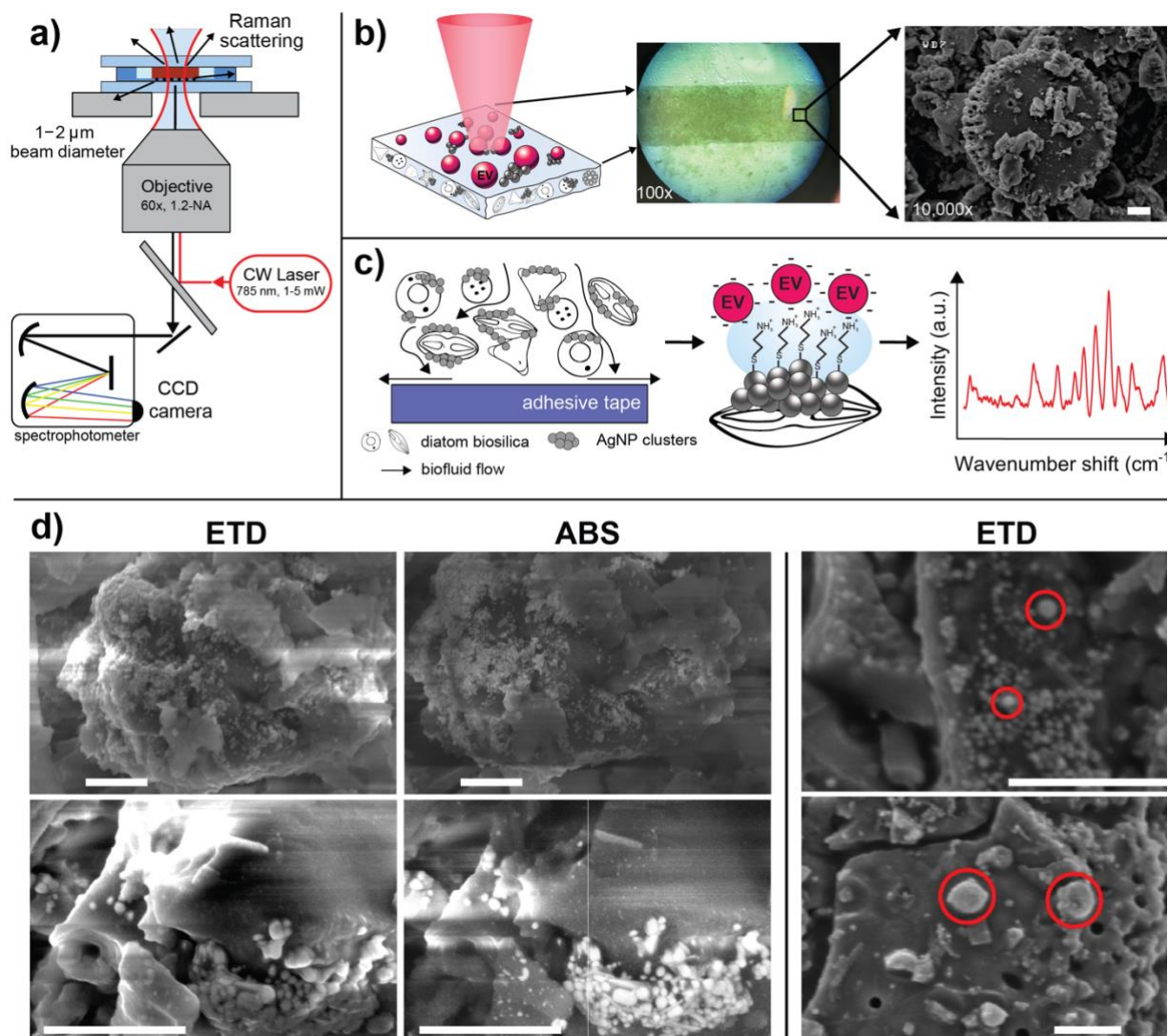
Figure 4.1: Overview of the nanoplasmonic substrate and SERS imaging process. **a)** Schematic of the SERS optical setup, where the substrate is sandwiched between quartz windows for analysis using an inverted confocal Raman scanning instrument. **b)** The biosilicate SERS substrate is irradiated by laser light to instigate Raman scattering. The insets show the heterogenous surface structure of the compacted diatom mesh at 100x and then under SEM at 10kx, where single diatoms are visible. **c)** The substrate allows for transport of EVs from solution to the proximity of AgNP clusters adsorbed to the compacted silicate scaffold. When functionalized with cysteamine, thiol bonds anchor to the AgNPs, enabling anionic EVs to adhere electrostatically to cysteamine's terminal amine groups. Spectral SERS fingerprints can be acquired from EVs adjacent to AgNPs. **d)** SEM micrographs of hybrid biosilicate mesh with AgNP clusters. An Everhart-Thornley detector (ETD) records the secondary electrons scattering from the surface whereas the annular backscattering detector (ABS) collects electrons more sensitive to atomic weight, highlighting the AgNP clusters. The images on the right show likely EV candidates localized in the vicinity of AgNP clusters throughout the hybrid material. The approximate starting concentration of EVs was $\sim 5 \times 10^8$ EV/mL. All scale bars are 1 μm.

4.2 AgNP-embedded plasmonic biosilicate scaffold for SERS-based diagnostics can filter and trap EVs from solution

At the core of plasmonic sensing are nanostructured metal materials, and cost-effective, highly sensitive, and flexible nanomaterials are of great interest,[199] particularly for low-resource settings. The main function of plasmonic SERS scaffolds is to boost weak spontaneous Raman scattering upon irradiation with light. We recently introduced the fabrication of a simple, robust, and flexible SERS substrate that has an increased enhancement factor (EF) of $\sim 1.0 \times 10^5$ with a high level of reproducibility for the development of inexpensive label-free biosensors.[200] In these substrates, enhancement is achieved via decoration of AgNPs throughout compacted biosilicate diatoms (**Figure 4.1**). Diatoms are unicellular photosynthetic biomineralized marine microalgae that excrete an amorphous silica cell wall, or frustule. These frustules serve as inexpensive photonic crystals[201,202] without the need for labor-intensive and costly lithography or etching techniques. When AgNPs are embedded within the diatom frustules, a dual plasmonics effect can be accomplished stemming from the coupling between LSPRs of metal NPs and guided-mode resonances of the frustules.[203,204] There are a few examples of utilizing gold or silver NPs as diatom-based hybrid plasmonic biosilicate SERS substrates, wherein the diatom-metal composites are typically achieved via in-situ growth or self-assembly of metal NPs.[205–207] These novel materials represent an inexpensive, easily fabricated SERS sensing alternative for a broad range of applications in life and materials sciences. Here we demonstrate the proof-of-concept use of these substrates for EV-based cancer diagnostic application.

Prior to incubation with biological materials, we used SEM to microscopically evaluate the surface of the substrate and the adherence of AgNPs to the diatom surfaces **(Figure 4.1d).** The ETD provides micrographs with contrast stemming from surface features, whereas the ABS detector is well-suited for establishing contrast sensitive to atomic weight. Hence, in the ABS images, AgNP clusters

are clearly separable as bright structures compared to the biosilica material. We also point out several candidates of EVs are adsorbed to the frustules at the vicinity of the AgNPs. Although the isolation procedure yields predominantly EVs in the size range of 50-200 nm as seen in **Figure 4.1d** in the upper right corner SEM image, it inevitably co-isolates proportions of bigger (>200 nm) EV subpopulations, some of which may be readily apparent in the lower right corner image. These EV populations are traditionally called e.g. "microvesicles", but due to the manifold nomenclature in the EV field, we chose to use a collective term "EVs". Comparably similar EV structures as visualized by SEM have been demonstrated previously.[208]

Recently we showed that the porous nature of the diatoms allows smaller molecules and nanostructures to disperse within the substrate, filtering through the biosilicate material.[200] The small average hydrodynamic diameter of EVs allows them to enter and distribute throughout the three-dimensional biosilica mesh, with smaller contaminants exiting through bottom of the substrate (theoretical calculations for this approximation can be found in the methods). To utilize these capabilities and immense surface area of the biosilica microstructure, we analyzed EVs isolated from SKOV-3 cells, a common *in vitro* human ovarian cancer cell line, as well as EVs isolated from various clinical serum samples. We chose to call 120,000 × *g* pelleted materials as EVs for the purpose of this study unless otherwise explicitly noted.[86]

To better localize the anionic EVs close to the AgNP clusters throughout the heterogenous biosilica substrates, we pretreated with cysteamine ($H_2NCH_2CH_2SH$, CA), a practical functionalizing agent to couple anionic species to metal surfaces.[209–211] The sulfhydryl group (-SH) of cysteamine binds to Ag/Au while the opposite terminal amine group (-NH$_2$) is freely exposed. Even after thorough washing, cysteamine remains present throughout the material. The strong peak at 650 cm^{-1} and the moderately fainter peak at 735 cm^{-1} both reporting on C-S stretching are practically absent in the spontaneous Raman spectrum of cysteamine (full detailed peak assignments are displayed in **Table**

4.1). This highlights that cysteamine forms thiol bonds with the AgNPs, such that these bonds undergo significant enhancements due to their proximity to the strong electromagnetic SERS fields.

Table 4.1: Chemical assignments for the relevant spectral peaks or bands identified in the work

Peak/band (cm^{-1})	Chemical assignment
643	Amino acids in proteins, e.g. tyrosine[212]
650	C-S stretching[209]
735	C-S stretching[209]
789-795	Vibrations in nucleic acids[93,97,193]
805	Si-O stretching; predominantly silicon motion e.g. within Si-O-Si units[185]
903	Carbohydrate-related SERS vibrations[155]
931	C-C ring stretching in e.g. proline[213]
940	C-C stretching vibration possibly coupled to C-N stretching vibration[209]
960	Protein vibrational modes, e.g. C=C deformation or C-N stretching[212,214,215]
1010, 1050, 1090	Si-O stretching; oxygen vibrating between silicon in the Si-O-Si bond[185]
1015	C-C stretching vibration possibly coupled to C-N stretching vibration[209]
1095	PO^{2-} stretching, C-C stretching, C-O-C stretching, glycosidic link in DNA/RNA[213]
1110	C$_\alpha$-N, C$_\alpha$-C, C-N stretching in protein backbone, C-C stretching in acyl chains of lipids[93,213]
1160-1170	Carbohydrate-related SERS vibrations[216]
1175	Nucleic acid vibrations in DNA/RNA, phenylalanine or tyrosine vibrations in proteins[93,213]
1240	C-N stretching + N-H deformation; amide III in proteins[92]
1287	CH$_2$, CH$_3$ deformation / C-N stretching + N-H deformation; amide III in proteins[93,213]
1290	CH$_2$ deformation in acyl chains of lipids[93,213]
1310-1340	Carbohydrate-related SERS vibrations[155]
1336	Backbone deformation C$_\alpha$-H / C$_\alpha$-C stretching / CH$_2$, CH$_3$ twisting or wagging in proteins[93,213]
1360	CH$_2$, CH$_3$ wagging in proteins[213]
1386-1390	Symmetrical CH$_3$ deformation in DNA/RNA, proteins, or lipids[92,213]
1400	Protein vibrational modes, e.g. CH$_2$ deformations[212]
1445-1460	CH$_2$ and CH$_3$ deformations in proteins and lipids[93,145]
1500	Conjugated -C=C- vibrations in nucleic acids[92–94]
1545	Protein vibrational modes, e.g. amide II vibrations[92,213]
1590	C-C ring vibration in aromatic groups[217]
1595	Vibrations in nucleic acids[93,213]
1620	C=C vibration in e.g. proteins[92]
1630	Amide I C=O stretching vibrations in proteins[93,97]
1650	Amide I vibrations in proteins or C=C stretching in lipids[93,145]

Following substrate treatment with cysteamine to functionalize AgNP clusters, we used a slightly acidic (pH = 6.4) buffer to wash the cysteamine-treated substrates in order to facilitate EV adsorption, since at this pH the amine groups are pushed towards cationicity (NH$_3^+$). On the basis of

the preliminary testing with various types of EVs and concentrations, it was significantly more difficult to find SERS hotspots with EV signatures when the surface was not pre-treated with cysteamine. To highlight the effectiveness of cysteamine modification, *in vitro* SKOV-3 EVs were incubated on non-cysteamine treated and cysteamine-functionalized substrates. An area of 64 µm² with a step size of 400 nm (i.e., 20 x 20 pixels) was raster scanned (**Figure 4.2**). A section of the fingerprint region (1400-1900 cm⁻¹) was integrated over, given that this region contains many peaks arising from biomolecules (**Table 4.1**) and is a quiet region for the blank substrates. Heatmaps were generated from the scans, and it is apparent that the cysteamine-functionalized surfaces exhibit more 'hot' areas than the substrates without cysteamine. We concluded that without cysteamine the EVs do not strongly adhere to the surface easily and are mostly rinsed away during subsequent washing steps. Cysteamine functionalization allows us to achieve reasonable measurement reproducibility via non-specific binding of EVs.
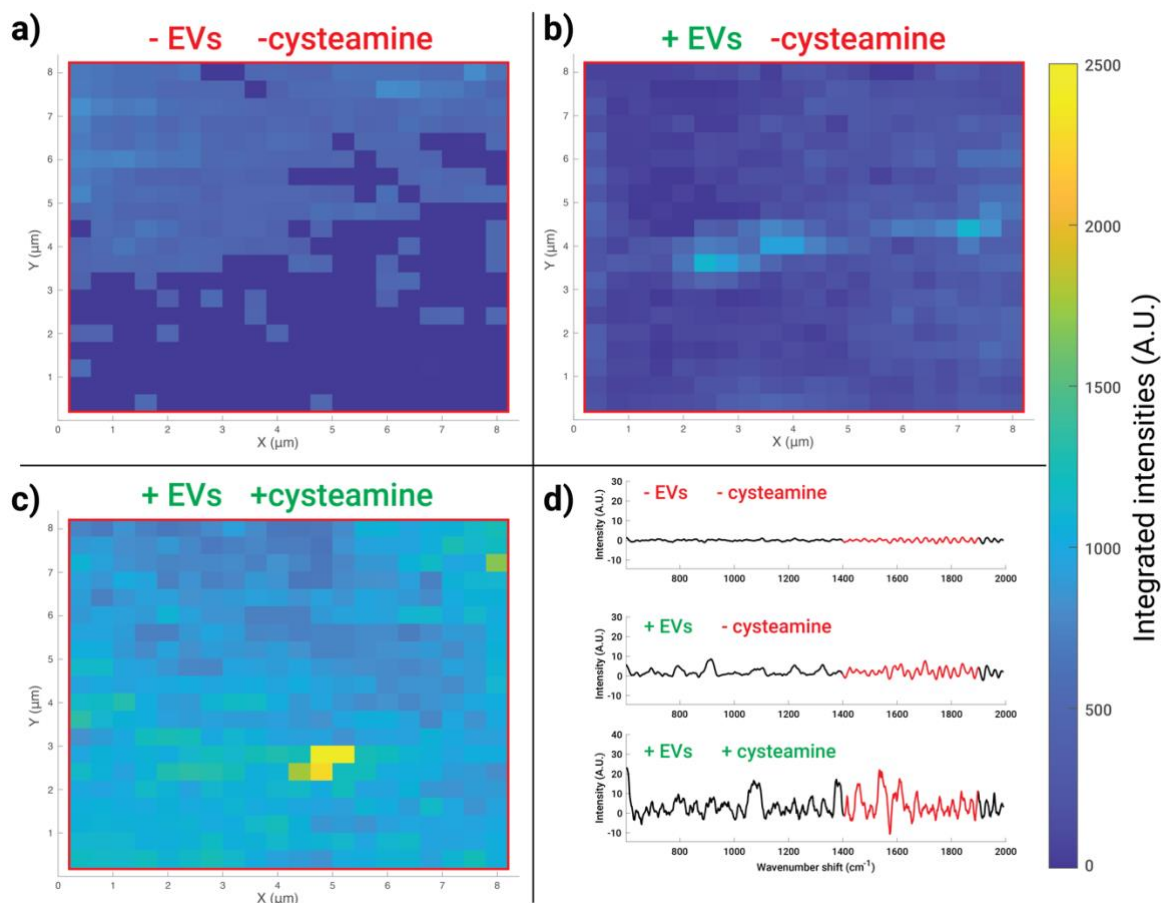
Figure 4.2: Spectral maps show increased signal of biosilicate SERS substrates upon cysteamine treatment. Maps of dimension 8 x 8 μm with 400 nm spacing between spectra were collected from (a) control substrate (b), substrate with SKOV-3 EVs, and (c) cysteamine pre-treated substrate with SKOV-3 EVs. Representative spectra for the maps are shown in (d). The red highlighted portion of each spectra in (d) represents the portion integrated under to generate the maps, chosen due to its coverage of protein and lipid peaks (Table 1), thus used as a surrogate for biomaterial. It is apparent that cysteamine pre-treatment enabled increased coverage of biomaterial in the substrate.

4.3 EVs treated with and without trypsin provide complementary biomolecular analysis

Method development for EV characterization and identification was initiated using *in vitro* SKOV-3 EVs produced in bioreactor flasks, which allow for cost-effective high yield EV production.[218,219] Particle concentrations as measured by NTA were used to normalize EV additions. In early experiments, we noticed that the majority of chemical components in SERS spectra of EVs could be attributed mainly to sugars with some small extent of protein features, but no nucleic acids, in contrast to our previous report of spontaneous Raman scattering from optically trapped whole EVs.[93] We suspected this was due the distance dependence of SERS, thus used enyzmatic

treatment of EVs to modulate the portion in contact with the plasmonic substrate. We previously demonstrated that EV surface proteins residing on a hydration layer can be modified by trypsin treatment.[93] Trypsin non-specifically cleaves extraluminal domains of surface proteins and a thick layer of carbohydrates (i.e., the glycocalyx),[220] which has been demonstrated to be a part of EV structure.[221] Our assumption was that this corona prevents EVs from getting close enough to the plasmonically active AgNPs (**Figure 4.3**). In turn, removing this layer may help to (i) expose complementary biomolecules for plasmonic signal amplification that takes place approximately within 5-10 nm distance[212,222] from the AgNPs and (ii) eliminate a major source of heterogeneity of EVs present in the glycocalyx. It is worthwhile stressing that the SERS distance is an estimate. It can slightly vary depending on the plasmonically active metal used (i.e. whether the metal is for example Ag, Au, Pt, or Al), and whether the measurements are performed on a film or planar nano-roughened surface or a colloidal metal nanoparticle solution.[212,222] The size and shape of nanostructures also contribute; in the case of films or planar surfaces the dimensions of nano-roughened surfaces dominate, while when using colloidal metal nanoparticles solutions, the size of nanoparticles is essential.

Furthermore, we acknowledge the potential of the glycocalyx for diagnostic purposes, therefore we hypothesized that a portion of the EVs' diagnostic value may be lost by enzymatic treatment. As meticulously demonstrated by Shurer et al., the overall composition and physical nature of glycocalyx appears to possess a remarkable role in cell membrane shape regulation, EV biogenesis, and thus on the surface composition of secreted EVs – including their glycocalyx corona.[223] The level of glycosylation of EVs is reported to affect their *in vivo* biodistribution,[216] and simultaneously EVs can carry enzymes on their shell that shape their own glycocalyx as well as similar glycocalyx structures in the extracellular matrix and surrounding cells.[224] Furthermore, given that tumor cells typically secrete high numbers of EVs[225] and their cell surfaces are abundantly crowded by mucins

and hyaluronan, we have a good reason to believe that (i) the EVs secreted by tumor cells reflect similar glycocalyx membrane composition with their parent cells, and therefore (ii) investigating the different constituents of the EV-associated glycocalyx corona indeed holds a great uncharted potential in the context of liquid biopsies and cancer diagnostics.
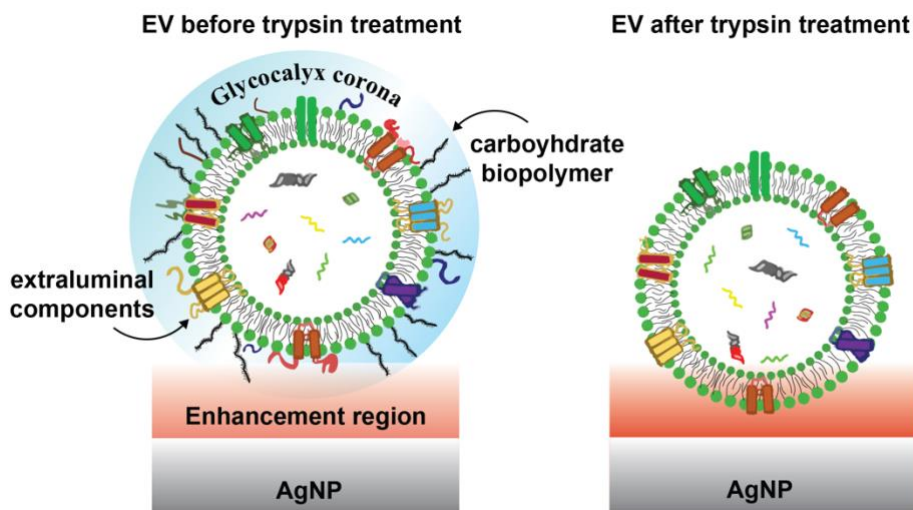
Figure 4.3: The potential effect of trypsin treatment on the glycocalyx and protein corona of EVs. Prior to trypsinization, the chemical components comprising the corona and near the outer shell of the EV are mainly exposed to the electromagnetic SERS amplification field (red). Trypsin cleaves off extraluminal domains of surface proteins and sugars that extend outside the vesicle's phospholipid shell, placing the EVs in closer contact with the AgNP with different parts, including some intraluminal components, experiencing stronger signal amplification.

To test that trypsin did not affect the cysteamine pretreatment, we incubated substrates with trypsin prior to any addition of EVs and rinsed thoroughly. We also measured the SERS spectrum of a non-treated empty substrate in order to demonstrate that the weak spectral features stemming from the substrate have none to minimal interference with the measured biological specimens. **Figure S4.1a-c** shows representative spectra of these controls, including solid cysteamine and cysteamine-functionalized substrates treated without and with 0.25% w/v trypsin solution, respectively. Characteristic cysteamine SERS peaks remained, suggesting that even harsh trypsin treatment did not significantly remove cysteamine, or blocks its ability for EV enrichment. **Figure S4.1d** shows representative spectra of a blank substrate, with discernible peaks/bands that are well-characterized and known to relate to various vibrational modes of Si compositions.[185] In particular, features at

805 cm^{-1} (Si-O stretching; predominantly silicon motion e.g. within Si-O-Si units), 1010 cm^{-1}, 1050 cm^{-1}, and 1090 cm^{-1} (Si-O stretching; oxygen vibrating between silicon in the Si-O-Si bond) are prevalent in the measured spectrum (**Table 4.1**). On this note, these spectra regions do not overlap and therefore interfere with our analyses distinguishing non-cancerous and cancerous EVs.

Subsequent analyses comprised stages where the EVs were treated with trypsin followed by
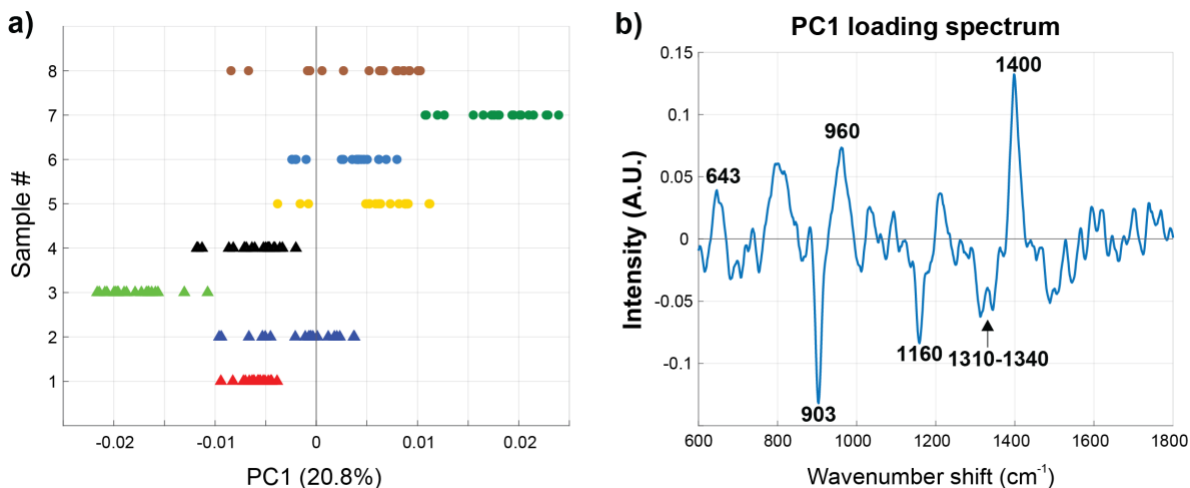
Figure 4.4: Trypsin treatment removes carbohydrates from EVs. a) PC1 score plot of native SKOV-3 EVs (triangle markers) and trypsin-treated SKOV-3 EVs (circular markers) measured on the substrate. b) PC1 loading spectrum with six spectral regions identified, three assigned to protein vibrational modes (643, 960, and 1400 cm^{-1}) and three assigned to carbohydrates (903, 1160, and 1310-1340 cm^{-1}). The negative scores on PC1 for trypsin treated EVs correspond to carbohydrates, indicating that the treatment effectively cleaves the extraluminal domain of EVs, exposing complementary biomolecules.

thorough washing. As shown in **Figure 4.4a**, a clear separation between native non-treated (triangle markers) and trypsin-treated (circular markers) SKOV-3 *in vitro* EVs was observed in the 1-dimensional principal component (PC) space, where each marker represents one individual spectrum. The PC loadings report on the variables, i.e., wavenumber regions, in the spectra that are pertinent for the group separation and thus provide information on the chemical differences between the measured groups. **Figure 4.4b** displays a PC1 loading spectrum that captures ~20.8% of the total variation between the SERS spectra acquired from native and trypsin treated EVs. Although the other PCs also have their contribution to the observed differences throughout the analyses, for ease of interpretation we display these results on the basis of PC1 since that dimension adequately and

consistently identifies the relevant biochemical contributors that differentiate these analyzed specimens from each other. In any case, all raw SERS spectra data is available for viewing or independent analysis.

As the PC score values (**Figure 4.4a**) are primarily negative for the native SKOV-3 EVs and positive for the trypsin-treated SKOV-3 EVs, this indicates that in the SERS data the wavenumber regions 643 cm^{-1} (amino acids in proteins, e.g. tyrosine), 960 cm^{-1} (protein vibrational modes, e.g. C=C deformation or C-N stretching) and 1400 cm^{-1} (protein vibrational modes, e.g. CH$_2$ deformations)[62] are pronouncedly present in the trypsinized EVs. Simultaneously the regions at around 903 cm^{-1}, 1160 cm^{-1} and 1310-1340 cm^{-1} are less represented. Intriguingly these three bands potentially report on carbohydrate-related SERS vibrations[61] (**Table 4.1**). Trypsinized EVs had clearly reduced protein contents in comparison to native EVs, while particle count by NTA remained in a similar range. Taken together, these findings imply that the EV glycocalyx/corona is indeed affected by trypsin treatment and as hypothesized, complementary EV surface structures are exposed to SERS amplification. This may be a generalizable treatment that can be applied to a variety of SERS substrates.

4.4 Limit of detection (LOD) for the biosilicate SERS scaffold

We determined the limit of detection (LOD) for sample concentration and laser power. SKOV-3 EVs were chosen for both of these experiments to promote consistency over the course of the testing. For the concentration LOD, SKOV-3 EVs were tested starting with an initial concentration of ~5 x 10^{12} particles/mL. After diluting 10^6-fold, the signal was still easily located in different areas on the substrate. After another 10^4-fold dilution (bringing the total dilution to 10^{10}-fold), we were still able to locate a few spots that produced signal, indicating the LOD for EV concentration is less than 600 particles/mL. Many plasmonic studies demonstrate LODs down to hundreds or a few thousand EVs.[208,226] Thus, the performance of our substrate resides in similar range demonstrating its comparability and feasibility for EV characterization. We additionally

determined the LOD for our laser power, an appropriate measure, since it would be useful for point-of-care diagnostics, particularly in low resource settings, to minimize the laser power. A lower laser power may also help preserve the sample condition to ensure platform reliability and repeatability. The substrates were prepared once again with SKOV-3 in a typical 100-fold dilution. Spots were interrogated across the substrate at decreasing levels of laser power. Spots were fairly easy to locate down to 800 µW, with even an occasional signal being seen as low as ~500 µW. The testing was eventually stopped because the laser power could not be decreased any further. We have previously established the SERS enhancement factor for these novel substrates.[200]

4.5 High inherent chemical heterogeneity of EVs isolated from a single patient sample

Before analyzing EV samples across a panel of clinical patients, we endeavored to evaluate the inherent heterogeneity within one clinical EV isolate derived from an ovarian cancer patient. Even one patient's EV sample can reflect various physiological states depending on the individual's physical activity, nutrition, etc. before the sample was drawn.[227,228] Furthermore, even the most subtle sample preparation and transfer practices can alter their internal composition and induce measurable variation between the EV subtypes present.[229] As expected, EVs exhibited internal variation even amongst a single analyzed clinical sample, as visualized by the three clearly separate clusters (blue, red, green) in **Figure 4.5a**, with hierarchal clustering analyses determined using the first 5 PCs. In the cluster-specific spectral loadings (**Figure 4.5b-d**) a positive peak indicates the existence of a certain chemical feature whereas a negative peak reports on the absence of a proposed chemical entity, compared to the global mean (shown in gray behind the cluster average spectra). The conceptual mathematical processing for obtaining these spectra can be found in the methods. We identified six regions of interest: 931 cm^{-1} (C-C ring stretching in e.g. proline), 1095 cm^{-1} (PO^{2-} stretching, C-C stretching, C-O-C stretching, glycosidic link in DNA/RNA), 1360 cm^{-1} (CH$_2$, CH$_3$ wagging in proteins), 1445 cm^{-1} (CH$_2$ and CH$_3$ deformations in proteins and lipids), 1590 cm^{-1} (C-C ring vibration

in aromatic groups), and 1620 cm^{-1} (C=C vibration in e.g. proteins) (**Table 4.1**). Based on these peak assignments, the measured EVs forming the blue cluster are seemingly enriched in nucleic acid (DNA/RNA) related vibrations whereas the red cluster represents the majority of the EVs, which are relatively consistent with the overall global average spectrum with the exception of fewer CH$_2$/CH$_3$ wagging vibrations from proteins. On the contrary, the green cluster EVs are enriched in those vibrations. It is not clear if this clustering represents an inherent chemically defined subpopulation spread of EVs, or rather the relative positioning of EVs towards the plasmonically enhanced electromagnetic fields propagated by the AgNPs throughout the substrate. Based on several scanning results as shown by way of example in **Figure 4.2**, we cautiously suggest that the inherent heterogeneity of EVs and their binding via cysteamine dominate variation, rather than the substrates themselves.
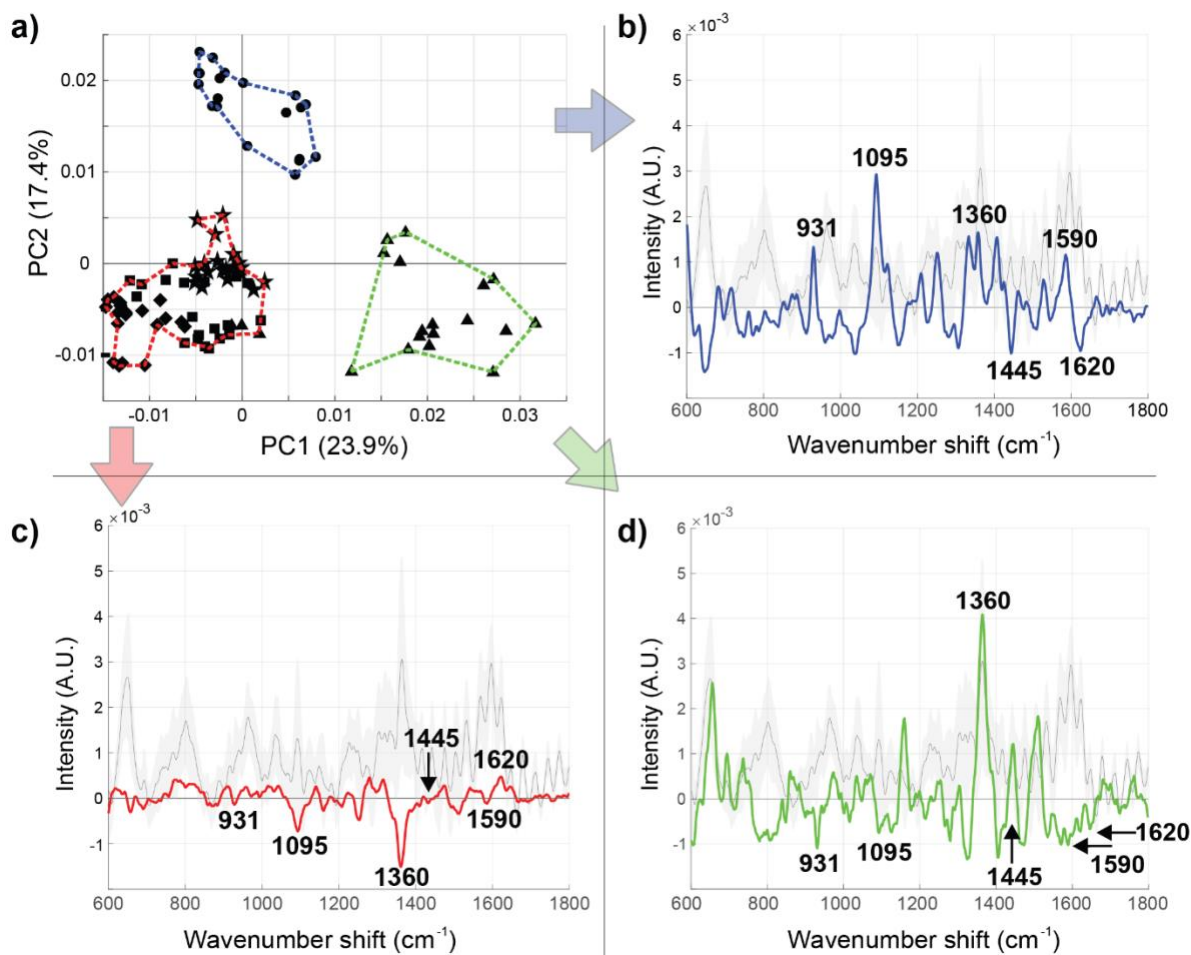
Figure 4.5: Distinguishable heterogeneity within EVs isolated by UC from a single patient diagnosed with ovarian cancer. (a) Two-dimensional PC score plot revealed three distinguishable clusters (blue, red, and green - defined using the first 5 PCs). Each point represents a single measurement taken within the substrate, with circles, stars, triangles, squares, and diamonds representing groups of repeated measurements sampled throughout the substrate (20 1-s spectra per spot). The chemical heterogeneity (as evaluated by the Euclidean distance in PC space) is more consistent within a sampled region (e.g., triangles) compared to spectra samples in different regions (e.g., triangles vs. circles). (b-d) The cluster-specific SERS spectra color coded according to the outlined regions in (a).

4.6 Evaluation of native clinical samples

8 clinical serum samples were obtained from the UCDCCC Pathology Biorepository resource as "remnants" – samples to be discarded following doctor-ordered CA125 ELISA assays as part of the patients' standard clinical care. These deidentified samples were annotated with clinical diagnosis of cancer type and staging, allowing us to bin samples accordingly. One of these patients turned out to not have malignant lesions, thus serves as a negative control. The other 6 samples represented

different cancer subtypes. Here we used this initial dataset to explore the utility of the SERS substrate and evaluate the inherent chemical heterogeneity across samples. **Fig. S4.2** shows representative SERS spectra of *in vitro* SKOV-3, endometrial cancer, ovarian cancer, and benign ovarian neoplasm EV samples used for subsequent multivariate analyses.
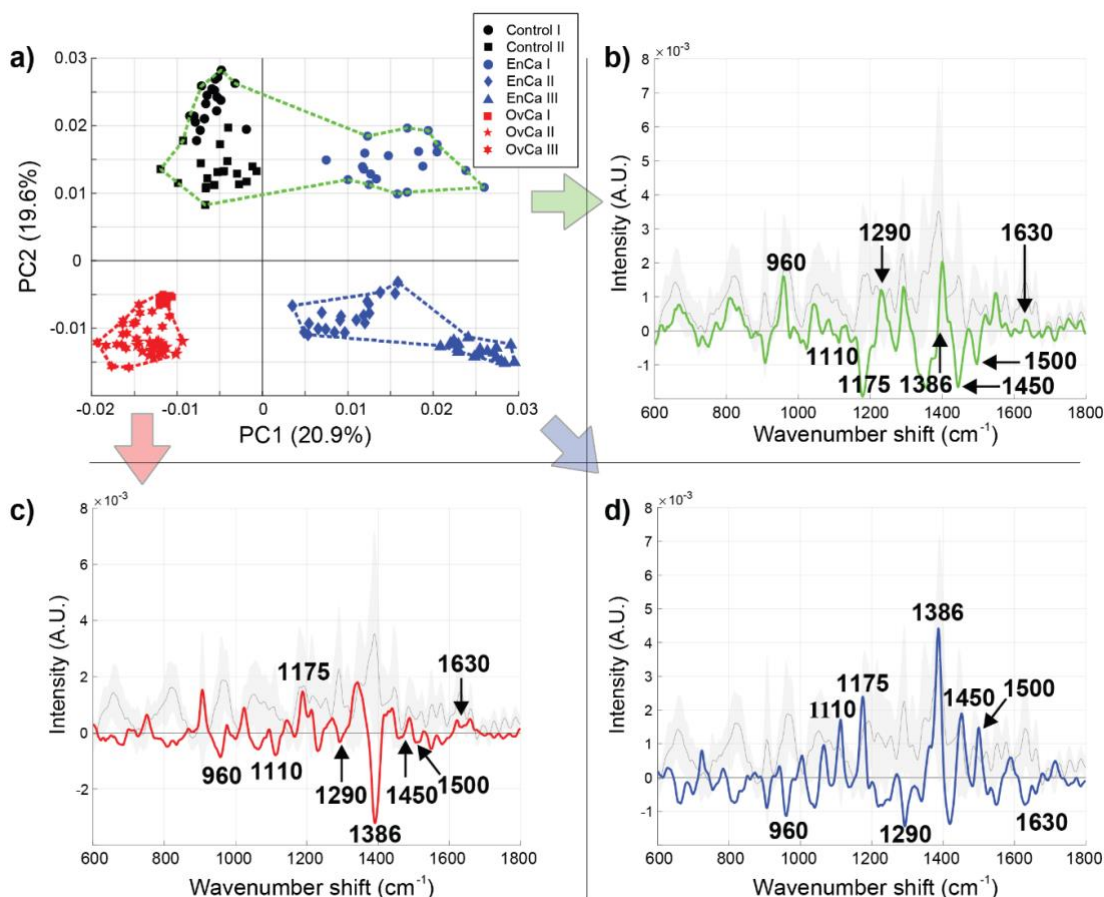
Figure 4.6: SERS analysis of native EVs isolated from endometrial (EnCa) and ovarian cancer (OvCa) clinical samples. (a) The PCA score plot and (b-d) three cluster-specific spectra derived from hierarchical cluster analysis (blue, red, and green dotted lines - defined using the first 5 PCs). Given the separation of EVs isolated from clinical samples, it appears that PC1 reports on the cancer type while PC2 informs on extent of cancer burden (the EnCa I patient, blue circles, was lower grade than the rest of the EnCa/OvCa samples).

Figure 4.7 represents the PCA for the acquired SERS spectra data from EVs of eight different individuals. **Figure 4.6a** displays the two-dimensional PC score plot (PC1 and PC2 capture ~40.5% of the total variation within this data set) while **Figure 4.6b-d** shows the cluster-specific SERS spectra (blue, red, green). Three of the samples represent different types and stages of endometrioid

malignancies (blue), three different types and stages of ovarian malignancies (red), and two controls that were not staged (black). A total of 8 spectral regions were selected for the subsequent analysis in order to infer the pertinent chemical differences between these clinical test samples: 960 cm^{-1} (protein vibrational modes, e.g. C=C deformation or C-N stretching in amino acids), 1110 cm^{-1} (C$_{\alpha}$-N, C$_{\alpha}$-C, C-N stretching in protein backbone, C-C stretching in acyl chains of lipids), 1175 cm^{-1} (nucleic acid vibrations in DNA/RNA, phenylalanine or tyrosine vibrations in proteins), 1290 cm^{-1} (CH$_2$ deformation in acyl chains of lipids), 1386 cm^{-1} (symmetrical CH$_3$ deformation in DNA/RNA, proteins, or lipids), 1450 cm^{-1} (CH$_2$ and CH$_3$ deformations in proteins and lipids), 1500 cm^{-1} (conjugated -C=C- vibrations in nucleic acids), and 1630 cm^{-1} (amide I C=O stretching vibrations in proteins) (**Table 4.1**). In addition to PCA and hierarchical clustering analysis, we also performed PCA followed by linear discriminant analysis (LDA). The control and cancerous samples can be distinctly classified, which is consistent with the obtained results using PCA-hierarchical clustering. An accuracy, sensitivity and specificity of 99.4%%, 100%, and 99.2% were calculated, respectively. Despite the model misclassifying only very few spectra, these numbers must be interpreted with caution given the limited sample size, inevitably yielding biased results and necessitating larger clinical cohorts in future studies. PCA-hierarchical clustering is largely used for our analyses since it enables determination of cluster-specific spectra that forecast the chemical differences more explicitly between the investigated sample groups.

By interpreting the cluster-specific spectra in **Figure 4.6** on the basis of the 8 assigned spectral regions, we can deduce tentative chemical contributors responsible for the observed differences. First, the EVs in the blue cluster exhibit distinctly enriched contents of proteins, lipids, and nucleic acids in comparison with the EVs in red and green cluster (positive bands on the blue cluster-specific spectrum at 1110 cm^{-1}, 1175 cm^{-1}, 1386 cm^{-1}, 1450 cm^{-1}, and 1500 cm^{-1}). Second, EVs from ovarian malignancies (OvCa I-III) have a pronouncedly different lipid composition compared to the EVs in blue and green

clusters (negative bands on the red cluster-specific spectrum at 1110 cm^{-1} and 1386 cm^{-1}). Third, the EVs in the green cluster demonstrate certain protein and lipid components being profoundly more represented than the same components in EVs forming the blue and red clusters (positive bands on the green cluster-specific spectrum at 960 cm^{-1} and 1290 cm^{-1}). However, simultaneously many of the nucleic acid and protein related vibrations are nearly absent in the green cluster (negative or negligible bands on the green cluster-specific spectrum at 1175 cm^{-1}, 1450 cm^{-1}, 1500 cm^{-1}, and 1630 cm^{-1}). PC1 clearly separated EVs from endometrioid type malignancies (EnCa I-III) from ovarian type malignancies (OvCa I-III). Also, EVs from ovarian malignancies cluster discernibly (red cluster and the associated cluster-specific spectrum). Lastly, the green cluster is formed by EVs from grade I endometrioid adenocarcinoma (blue markers, EnCa I) and two control samples (black markers): a benign ovarian neoplasm (Control I) and an unspecified gynecologic neoplasm (Control II). Interestingly, while the unspecified control was marked as low CA125 in the clinical testing, it was not able to be explicitly graded. Our analysis may provide a unique angle to better grade such samples where histological analysis is unclear. This green cluster resides on the positive side of PC2 axis, and the red and blue clusters are located on the negative side along PC2 axis. Taken all these considerations into account, we posit that PC1 fundamentally reports on the disease type while PC2 informs on the disease state. To further investigate, whether the hypothesis regarding PC2 interpretation (i.e. containing information about the disease state) was plausible, we cultured an EnCa *in vitro* cell line and isolated the EVs. We then used the *in vitro* EnCa and OvCa EVs for validation representing cancerous chemical features, the clinical control samples (Control I and II) were harnessed as representatives of non-cancerous characteristics, and the clinical "early stage" and "late stage" EnCa and OvCa EVs were subjected to the analysis. Along the lines with the results displayed in **Figure 4.6**, this initial validation emphasizes that cautious interpretation of the disease state can potentially be made, especially for EnCa samples. However, we acknowledge that the sample size in the current study is

limited, that the explicit chemical differences remain to be resolved, and the main emphasis of this study was to discern different cancer types from each other using a novel SERS approach. On this note, however, this demonstrated separation capability might suffice as a practical pre-diagnostic SERS application in a clinical setting complementing conventional screening methods.

4.7 Trypsinization of clinical EVs greatly reduces diagnostic specificity

In the final stage of this study our intention was to subject the analyzed clinical EV samples to trypsin treatment. Such enzymatic treatment would result in (i) cleavage of non-specific glycocalyx/corona components (wholly or partially) to expose EV inner core structures for plasmonic amplification, and (ii) reduction of the inherent chemical heterogeneity. The native EV samples not subjected to trypsin treatment are shown in the **Figure 4.7a** PCA score plot as filled markers and the trypsin-treated samples are represented as empty markers. In **Figure 4.7b-d** eight spectral regions were pinpointed in the three cluster-specific spectra (blue, red, green) for further analyses: 789 cm^{-1} (vibrations in nucleic acids), 904 cm^{-1} (carbohydrate-originating vibrations), 1287 cm^{-1} (CH$_2$, CH$_3$ deformation / C-N stretching + N-H deformation; amide III in proteins), 1336 cm^{-1} (backbone deformation C$_\alpha$-H / C$_\alpha$-C stretching / CH$_2$, CH$_3$ twisting or wagging in proteins), 1390 cm^{-1} (CH$_3$ deformation in nucleic acids, proteins or lipids), 1450 cm^{-1} (CH$_2$ and CH$_3$ deformations in proteins and lipids), 1595 cm^{-1} (vibrations in nucleic acids), and 1650 cm^{-1} (amide I vibrations in proteins or C=C stretching in lipids) (**Table 4.1**). The experiments and analysis were carried out using the same clinical EV samples with the exception of excluding the unspecified gynecologic neoplasm group (Control II) due to the lack of adequate amount of sample material. Notwithstanding the sample groups and experimental parameters were kept consistent.
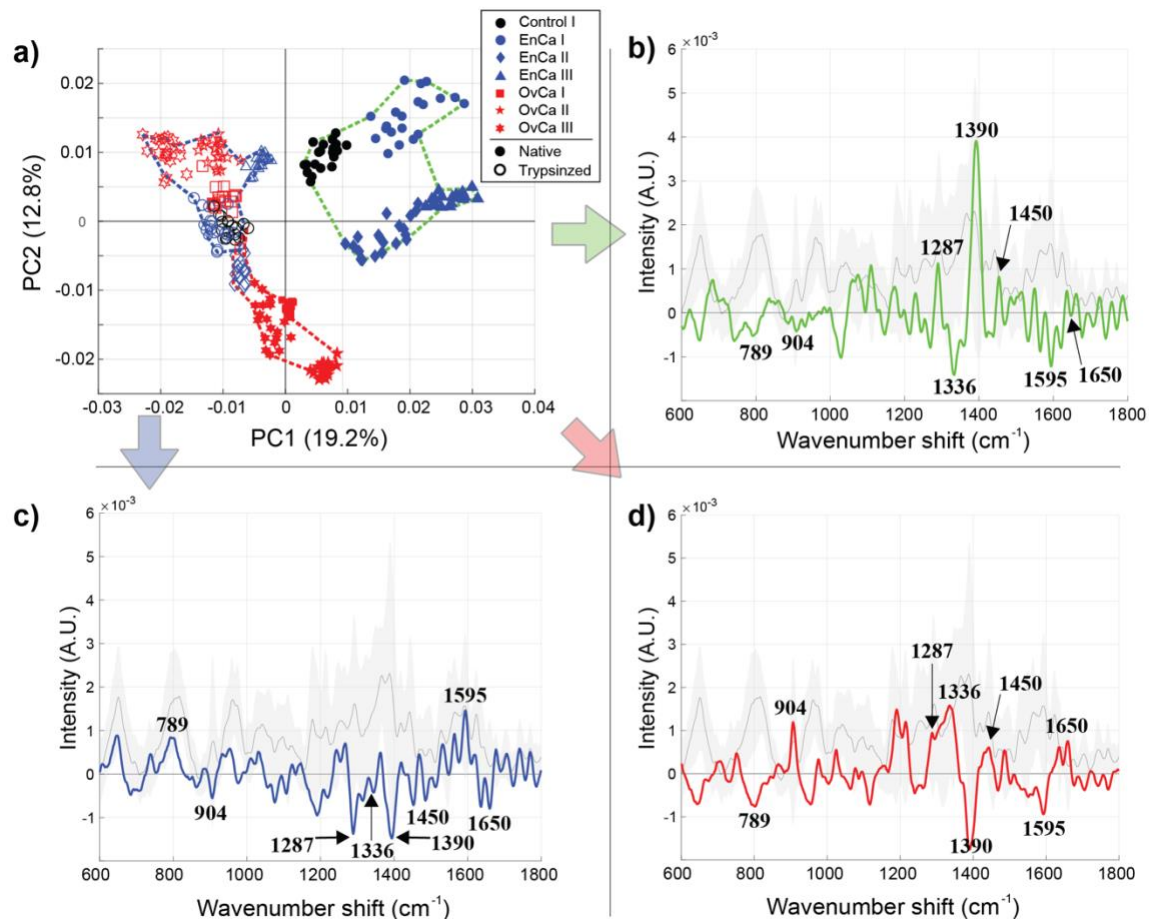
Figure 4.7: SERS of EVs isolated from seven clinical samples without and with trypsin treatment. (a) The PCA score plot and (b-d) the three cluster-specific SERS spectra (blue, red, green - defined using the first 5 PCs). The native EV samples are shown as filled in markers while the trypsin-treated measurements are shown as empty markers. As visible by their tighter spacing in this PC space, the trypsinized samples were markedly reduced in overall chemical content, indicating the glycocalyx/corona may also indicate disease-relevant chemical information.

Intriguingly, the band regions at around 789 cm^{-1} and 1595 cm^{-1} (arising from vibrations in nucleic acids) are distinctly positive for the majority of trypsin-treated EVs (blue cluster-specific spectrum) while the same region is clearly negative for non-treated EVs (red and green cluster-specific spectra) implying that trypsinization indeed facilitates exposing more of the intraluminal EV contents (e.g., DNA/RNA) to SERS amplification. Concurrently, large part of the other bands describing mainly protein and carbohydrate features of the EVs are negative for the trypsin treated EVs compared to the non-trypsinized EVs further indicating that at least partially these constituents may have been cleaved off by trypsin. The red cluster containing all the non-trypsinized EVs from ovarian malignancy type patients (OvCa I-III) and the trypsinized EVs from a serous endometrial cancer

patient (EnCa II, empty blue diamond markers) is highly positive for bands at 904 cm^{-1}, 1287 cm^{-1}, 1336 cm^{-1}, and 1450 cm^{-1} compared to the global average. This observation may indicate a specific protein and carbohydrate composition in these EVs. Even though some trypsinized serous EnCa EVs (from EnCa II) cluster with the untreated OvCa samples, they are closer in PC space to the trypsin treated EVs (blue cluster), and therefore explicit conclusions about their chemical composition following trypsin treatment remain unclear. Similarly, the green cluster comprises untreated EVs isolated from endometrioid malignancy type patients (EnCa I-III, filled markers) and the benign ovarian neoplasm control sample (Control I, filled black circle markers). These samples potentially have a unique – highly likely protein and/or lipid related – chemical fingerprint as the band at around 1390 cm^{-1} discernibly stands out compared to the EVs in blue and red clusters. Importantly, as evidenced by these results, our initial hypothesis of losing some of the diagnostic relevance through the trypsin treatment of EVs is evident. Although we were potentially able to better expose the intraluminal components of EVs for SERS amplification, the separability between samples decreased (**Figure 4.7**, non-trypsinized vs. trypsinized EVs). LDA analysis of the native EVs and trypsin treated EVs allow for computing a confusion matrix (**Figure S4.3b,d**). We utilized the data from the confusion matrix to assess the accuracy, sensitivity, and specificity of detecting cancer using our SERS substrate and clinical EVs. For native EVs our sensitivity and specificity are 100% and 99.2%, respectively, and the accuracy is 99.4%. But after trypsinization of those samples, the sensitivity drops to 45%, specificity to 99.1%, and accuracy to 86.4%.

These results strongly imply that the extraluminal domain, including membrane proteins and glycosylated moieties of lipids and membrane proteins, are critical to indicating cancer presence. While we acknowledge that the sample size of this clinical dataset is small, this is a key finding of this work that warrants further investigation. It is known that variations in cell surface glycoproteins significantly impact the progression of cancer, including the patients' prognosis.[230] Functional and analytical

studies will be needed to elucidate the particular glycoproteins that are involved in distinguishing clinical samples from one another, and to discern their potential role in EV signaling in cancer.

4.8 Supplementary Information
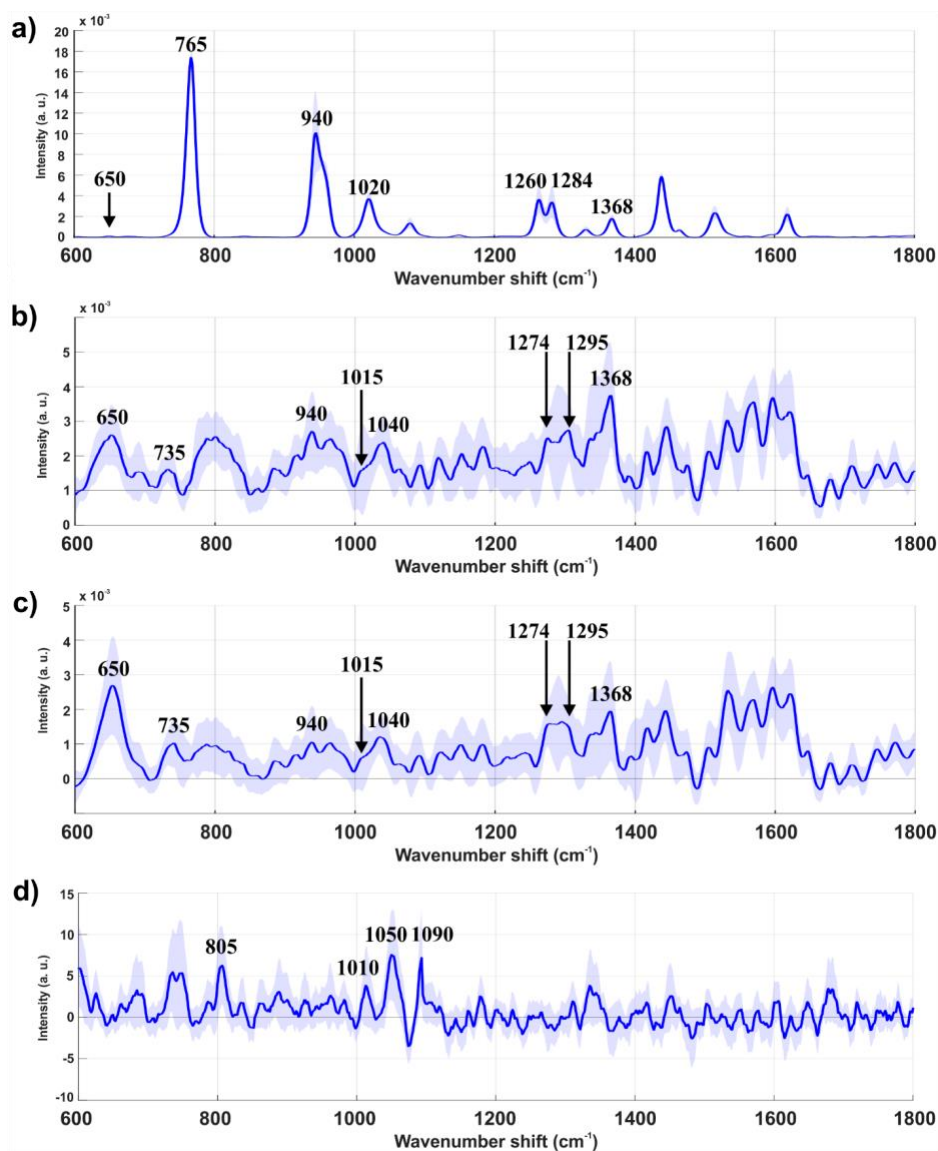
Figure S4.1: a) Spontaneous Raman spectrum of solid cysteamine, **b)** SERS spectrum (± 1 standard deviation) of 20 mM cysteamine solution measured from the biosilicate substrate before and **c)** after 0.25 % w/v trypsin treatment. The pretreatment testing demonstrated discernible existence of characteristic cysteamine SERS peaks/bands at 650 cm^{-1}, 735 cm^{-1}, 940 cm^{-1} and 1015 cm^{-1} before and after the surface was incubated in trypsin. Therefore, it is conceivable that trypsin does not quench or block cysteamine functionality, hence providing a suitable platform for EV enrichment. **d)** Spectrum of a blank biosilicate substrate without any trypsin or cysteamine treatment nor EVs added. The peaks/bands at 805 cm^{-1}, 1010 cm^{-1}, 1050 cm^{-1} and 1090 cm^{-1} can predominantly be assigned to different modes of Si-O stretching vibrations. It is noteworthy that these features do not overlap with the spectral regions of interest used for the EV analyses.
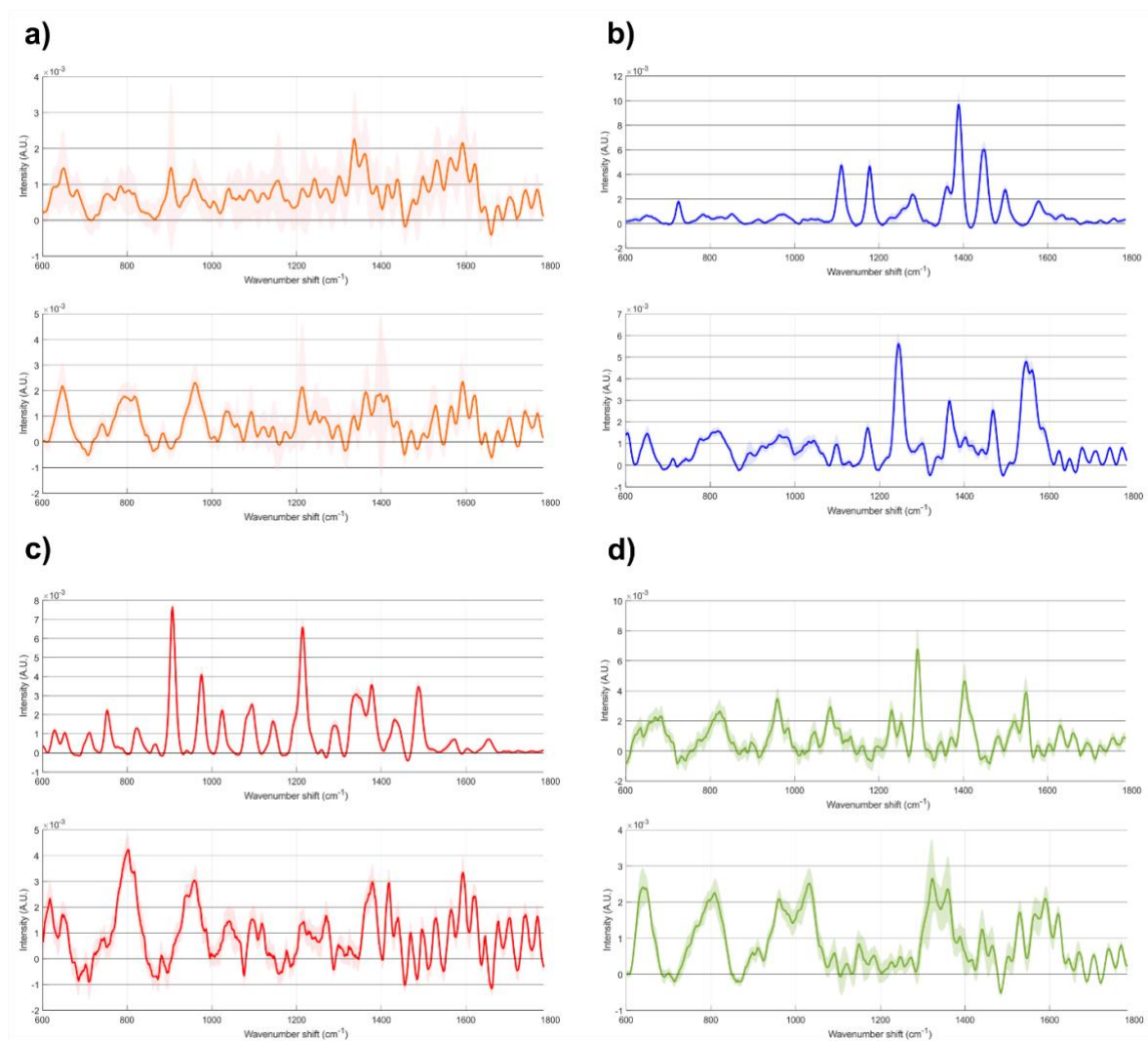
Figure S4.2: Representative examples of non-trypsinized and trypsinized SERS spectra. The upper panel for each group represents non-trypsinized sample and the lower panel displays trypsinized sample. **a)** In vitro SKOV-3, **b)** endometrial cancer, **c)** ovarian cancer, and **d)** benign ovarian neoplasm EVs measured on the biosilicate SERS substrate. Spectra were processed via normalization (total area to 1), smoothing, and background fitting using penalized least squares (PLS).
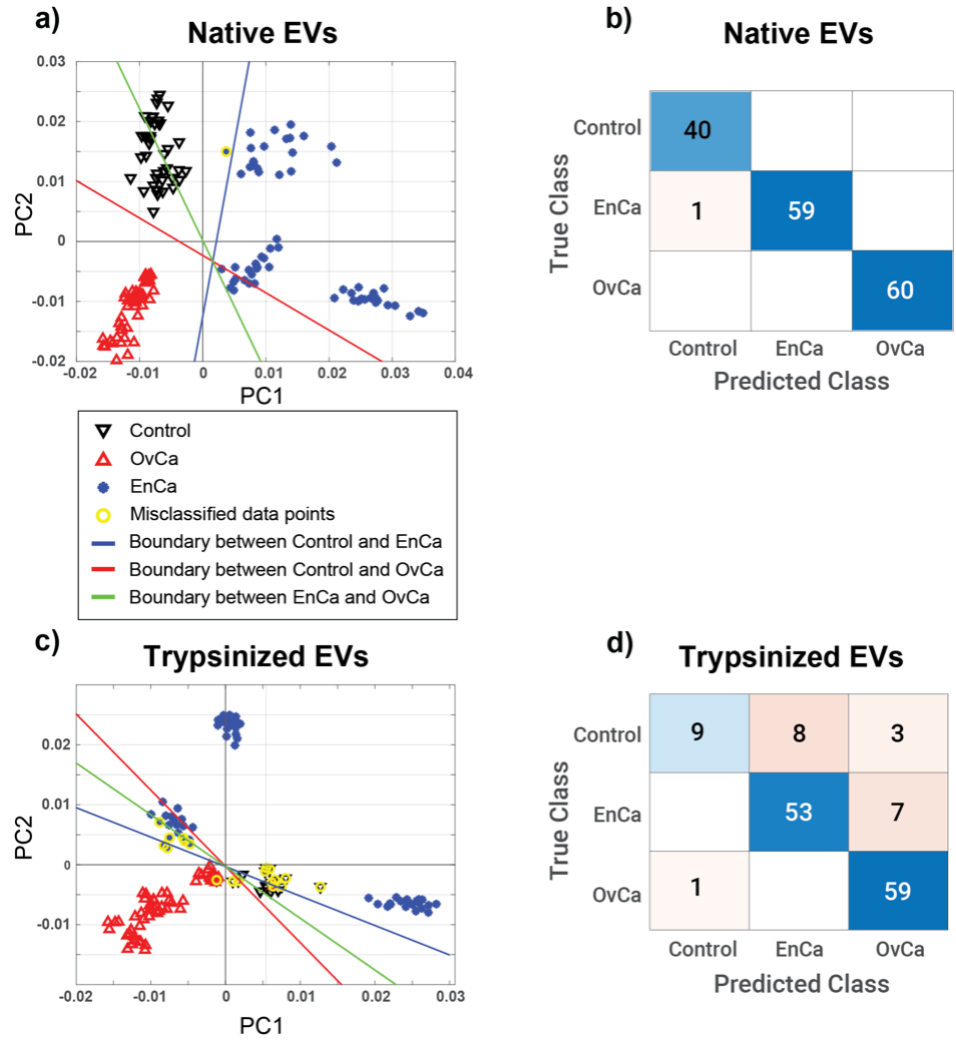
Figure S4.3: A PCA-LDA analysis performed for the tested clinical EV samples. **(a)** The LDA determined for native EVs after data dimensionality reduction by the PCA. The control samples are marked with black downward pointing triangles, OvCa samples with upward pointing red triangles and EnCa samples with blue asterisks. The blue and red boundaries differentiate the control, EnCa, and OvCa samples, respectively. The green boundary separates the EnCa and OvCa samples. The yellow circles around the data points indicate the misclassified spectra. **(b)** The confusion matrix for the native EVs. An accuracy of 99.4% was calculated for the assays. The sensitivity (TP/TP+FN) was determined 100%, and the specificity (TN/TN+FP) 99.2% regarding its capability to distinguish between non-cancerous and cancerous samples. **(c)** The LDA determined for trypsinized EVs, and **(d)** the corresponding confusion matrix. An accuracy of 86.4%, sensitivity of 45% and specificity of 99.1% were calculated for the assay when trypsinized EVs were analyzed instead of EVs in their native state. However, due to the limited sample size utmost caution need to be exercised while interpreting these numbers, and a more thorough patient cohort study carried out to evaluate the true performance of the method.

4.9 Conclusions

This report outlined the preparation of a new type of porous, nanoplasmonic substrate for EV analysis. We detailed a methodology for tackling the inherent heterogenous structure of the scaffolds and rigorous multivariate data analysis steps in order to reproducibly reveal the cancerous SERS spectra features in the measured data sets. As the spectral analyses demonstrate, we have successfully investigated and characterized EVs from *in vitro* cell cultures and clinical samples with an estimated LOD of ~600 EVs/mL with low laser powers. We demonstrate both a chemical treatment using cysteamine to non-specifically bind EVs, and also the large effects of extraluminal cleavage to provide complementary chemical information using a SERS approach. Both chemical treatments are generalizable to SERS analysis platforms, but especially useful for our substrate, which is easily washed due to its porous structure. Of note, we report that enzymatic cleavage of the EVs' extraluminal domain resulted in loss of sensitivity to detect clinical patient samples of endometrial and ovarian cancer, indicating that those components may be of clinical significance. To implement liquid biopsy methodology based on this platform to the clinic, standardization/automation of isolation and sample handling techniques, evaluation of reproducibility and cost-effectiveness, and validation by clinical trials are required. We envision that this work can act as a step towards a modern, minimally invasive plasmonic liquid biopsy platform with adequate sensitivity, specificity, and economical aspects for future implementation.

Chapter 5: Surface enhanced Raman scattering of extracellular vesicles for cancer diagnostics despite isolation dependent lipoprotein contamination

Context: Here we expand on the ability of SERS to uncover diagnostic information from competing signals stemming from co-isolated biomolecules. Lipoprotein particles are isolated in the same fractions as EVs, meaning they are present in the samples being studied. We show our technique is sensitive enough to ignore the spectral features from these co-isolates and still uncover important information from EVs that correlate to the patient's disease state.

5.1 Introduction

Extracellular vesicles (EVs) are nanoscale biomolecular packages of variable size and composition readily found in all biofluids and shed by every cell type measured to date.[230] EVs play important roles in cellular communication via the directed shuttling of functional proteins, lipids, small molecules, and small non-coding nucleic acids.[64],[86] EVs are generally subdivided into categories, including exosomes, microvesicles, ectosomes, oncosomes, apoptotic bodies, and more, typically based on molecular features (*i.e.*, size, morphology, composition) or biogenesis pathway.[231] There has yet to be unanimous agreement on the appropriate terminology for a given subpopulation, so in this study we refer to the isolated vesicular particles across all methods using the more generic term of EVs,[86] though it is clear that these isolates also contain contaminating non-vesicular species as demonstrated in this study.

Given that released EVs exhibit composition reflective of their parent cells in response to local external stimuli, they represent a rich source of potential biomarkers with great potential for clinical application.[64,74–79,232,233] Yet many challenges remain before that potential can be reached, especially in the choice of EV isolation methodology, which has a known effect on the quality and content of the isolated product.[86] In addition to vesicles, isolates may contain a variety of additional

nanoscale biomolecular assemblies, including ribonucleoparticles,[234] protein aggregates, small cellular debris, viruses,[235] and many types of lipoprotein.[218,236–240] There is no consensus on the expected concentration range of each particle type present in a given biofluid, since abundance is not predictable and influenced by a number of parameters, such as age,[241] sleep,[242] exercise,[243] diet,[244] and disease burden.

This study focuses on quantifying extent of contamination in EV isolates by lipoprotein, which represent a major fluctuating source of nanoscale particles in human biofluids. In plasma isolates, lipoprotein particles can be present up to 100-fold more than EVs.[239] Lipoprotein manifest in many classes that vary in size and density. Chylomicrons serve as lipid and cholesterol transporters abundant in the blood with wide variation in size, ranging from ~75 to 1,200 nm.[245] Smaller very low-density lipoprotein (VLDL), with nominal dimensions between 30-80 nm,[26] can further be converted into
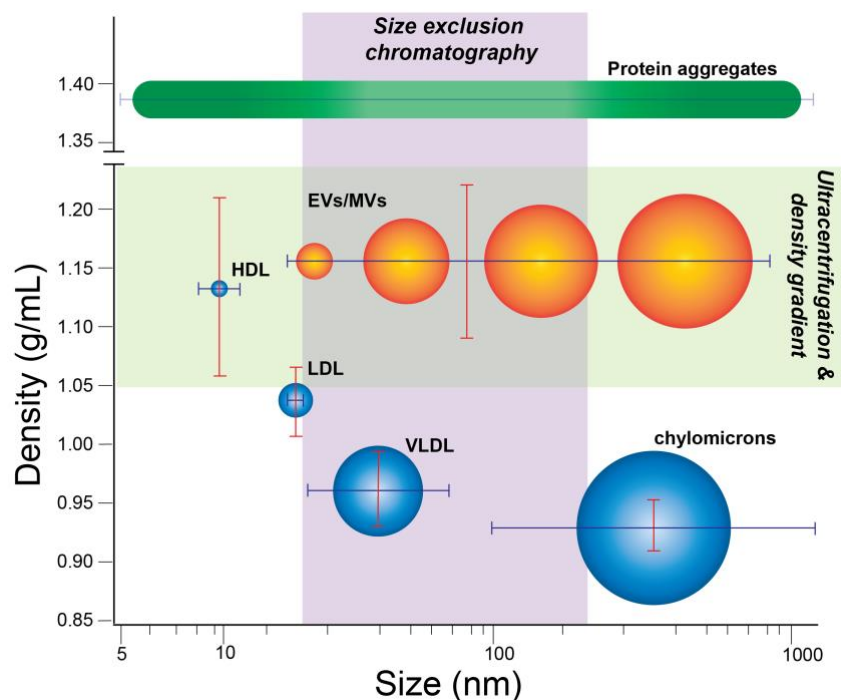
Figure 5.1: EVs and lipoprotein subtypes overlap depending on isolation method. Lipoproteins (blue) and EVs (orange) plotted according to respective size and densities, with various methods of isolation overlaid to show the relevant populations isolated by a given technique. EVs represent a heterogenous grouping of vesicular particles, including nanoscale exosomes, ectosomes, and other small EVs, but also larger microvesicles. EVs are thus spread over a large continuous range of sizes and densities. While more discrete in size and density per subtype, certain lipoproteins (HDL, LDL, VLDL, or chylomicrons) share significant overlap with EVs in size and/or density, thus are co-isolated to various extent depending on the particular isolation method.

even smaller types of lipoprotein, including intermediate-density lipoprotein (IDL, 25-35 nm) and low-density lipoprotein (LDL, 18-25 nm), though IDL is a transient species not readily isolated on its own.[245] Chylomicrons, VLDL, and some LDL share nominal size overlap with EVs (~30-150 nm). High-density lipoprotein (HDL, 5-15 nm) is the smallest in nominal size and below the lower threshold for EVs, yet does overlap with EVs in density (~1.05-1.20 g mL^{-1}).[245] Because of these features, isolation methods based on separation according to size or density can co-purify lipoprotein to various extent (**Figure 5.1**).

The most appropriate EV isolation method depends on the biofluid source and desired purity or downstream application, since isolation methods greatly influence yield and purity of EVs.[88,246] Differential ultracentrifugation (UC) remains the most commonly used gold standard method.[88,246–248] UC separates components according to relative density with additional influence from the size of the particles present. For a given rotor type and speed[249] sedimentation rate is proportional to (i) the difference between the density of the medium and the density of the particle and (ii) the square root of the particle radius.[237] HDL particles co-isolate with EVs when employing UC.[240] Although EVs are larger than HDL particles and thus sediment faster, prolonged UC spins typical for EV isolation permit a significant amount of HDL lipoprotein to pellet as well.[237] Still, the percentage of EV to HDL vesicles remains unclear, as current methods struggle to efficiently distinguish them post isolation.[240]

Related to UC is density gradient (DG) (or density cushion) ultracentrifugation. Also based on density, DG relies on chemical gradients to separate particles during an extended (~18 hr) spin.[247] In DG, plasma components move through the gradient until they reach their respective isopycnic point (equilibrium condition). Banded fractions can be collected, and the gradient material removed to enrich EVs. Given their similar density ranges, EVs and HDL elute to the same locations and are co-isolated.[240] Thus, for both UC and DG, HDL is the primary lipoprotein contaminant.

Size exclusion chromatography (SEC) is an emerging alternative to high-speed centrifugation techniques.[246]·[90,250,251] In SEC, gel matrices with defined pore sizes provide a mechanism for smaller contaminants to travel through, while larger particles cannot enter the pores and elute more quickly. Eluted fractions can be pooled and concentrated to enrich EVs from biofluids. Yet, since chylomicrons, LDL, and VLDL all overlap in size with EVs, they each are co-isolated in the EV-rich fractions.

Some work has been performed to assess the purity of different bulk isolation methods using biochemical techniques of Western blotting or ELISA, yet they are either not quantitative or require high volumes of sample input or expensive reagents, and neither are amenable for rapid analysis.[239] A promising approach to improve on these limitations is surface-enhanced Raman scattering (SERS). SERS is a spectroscopic technique that provides valuable chemical information through the plasmonic amplification of inelastically-scattered photons following sample irradiation. It is an appealing technique for bio-analysis given that it is inherently label-free, non-destructive, and ultrasensitive, and can provide multiplexed chemical fingerprinting at the nanoscale with a single laser.[54–56,58,96,135,252] The application of SERS to identify EVs in a label-free manner has been recently reviewed.[253] Besides diagnostic evaluation of EVs, spontaneous Raman spectroscopy has been reported to be able to assess purity, yet that study did not consider the effects of lipoprotein contamination, analyze combinations of methods, nor evaluate clinically significant samples acquired from patients.[150]

In this study we utilized SERS to quantify the extent of lipoprotein contamination (accounting for each of the major subtypes) in a representative clinical dataset of EV isolates purified from plasma of head and neck cancer patients and healthy controls. We varied isolation methods between UC, DG, SEC, and a combination of UC+SEC to assess the effect on lipoprotein vs. EV content. By fitting resulting spectra of purified isolates to spectra of analytical standards of chylomicrons, VLDL, LDL,

and HDL, we could accurately recapitulate the type and extent of lipoprotein co-isolated across each method. Notably, due to the multiplexed nature of SERS chemical analysis (spectra also contain molecular differences between samples not due to lipoprotein contamination), we found that cancer patient samples could be readily distinguished from non-cancer controls regardless of chosen isolation methodology and extent of lipoprotein contamination. This renders SERS a powerful tool, capable of both assessing lipoprotein content and concentration, but also seeing through such chemical contamination to reveal underlying disease-associated features relevant to diagnostic application.

5.2 EV and lipoprotein isolation and characterization

We analyzed a focused dataset of whole blood samples isolated from patients undergoing head and neck surgery at UC Davis Health. Patients were consented prior to surgical tumor resection using an IRB-approved protocol and samples were provided to our lab stripped of identifying information. Our sample cohort contained nine patients with squamous cell carcinoma and four non-malignant controls, according to histopathological analysis.

After pre-clearing large aggregates up to 10,000 x g, samples were evenly divided by volume and subject to either UC, DG, or SEC isolation protocols. In later experiments, sequential isolation methods were employed (*i.e.*, UC followed by SEC on the same sample). Following a particular isolation method, EV-enriched isolates were analyzed for size and number concentration by nanoparticle tracking analysis (NTA). Across isolation techniques, samples consistently contained from 1×10^{11} to 2.5×10^{12} particles mL^{-1} with diameters apparently ranging from $\sim$50 – 300 nm and modes between 65 – 165 nm (**Figure 5.2a**). There are some caveats to NTA, given its practical lower detection limit of $\sim$70 nm for typical refractive index measures of organic material[254,255], though it is known large numbers of EVs are present down to 30 nm[256,257]. Transmission electron microscopy (TEM), for example, reveals a large number of sub-70nm particles (**Figure 5.2b**). For both NTA and TEM, due to the overlapping sizes of EVs with chylomicrons, VLDL, and LDL,

particle count interpretation is difficult, thus we are careful not to overinterpret any slight differences between EVs from various preps across these methods. Isolates were further characterized by single particle interferometric reflectance imaging sensing (SP-IRIS) using the ExoView R100 (NanoView Biosciences, Boston) platform and antibody coated spots of anti-CD9, anti-CD63, anti-CD81, and control mouse anti-IgG, and the same antibody types for sandwich detection.[258] While TEM and NTA cannot easily determine if particles are lipoprotein or EV in nature, SP-IRIS helps confirm the presence of common EV sequestered tetraspanins (**Figure 5.2c,d**). When expression levels for capture/detection pairs are normalized to each sample's total particle count, (**Figure 5.2d**) it is clear

that trends in expression of those three tetraspanins are relatively consistent across several clinical samples over a mix of isolation methods.
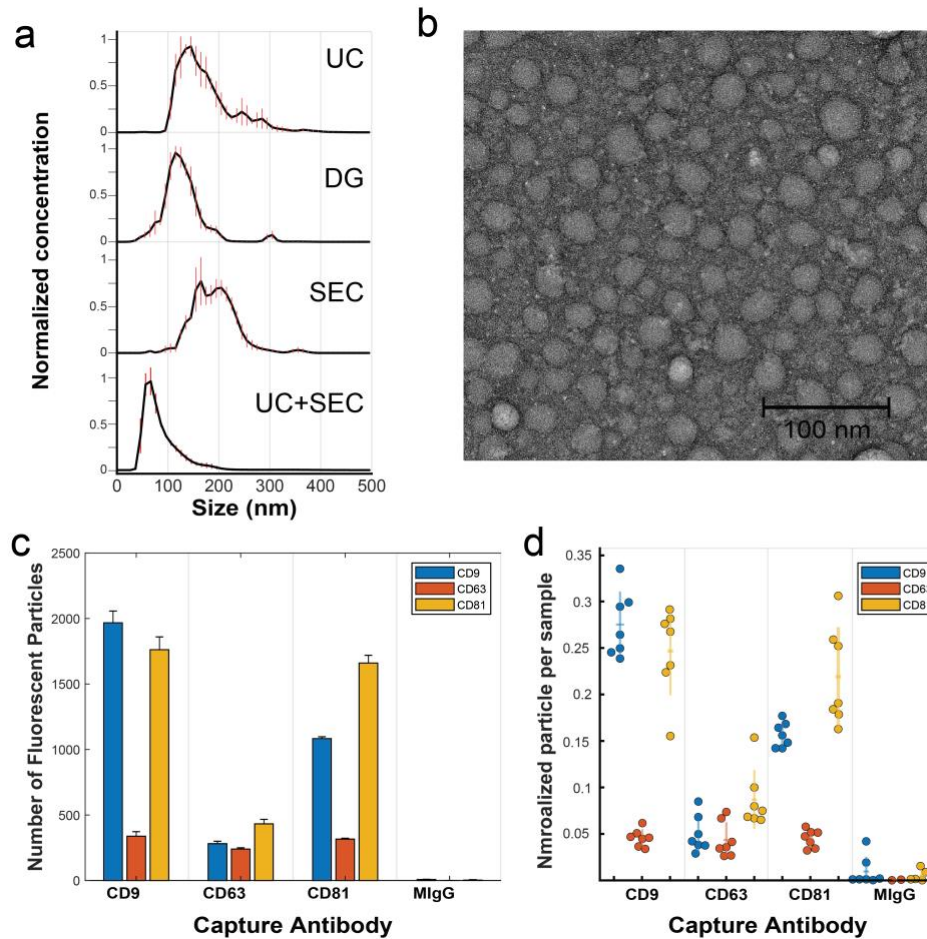
Figure 5.2: Characterization of EVs. **(a)** NTA is used to measure size distribution and particle concentration for the isolation methods UC, DG, SEC, and UC+SEC performed on a representative clinical sample. **(b)** A negative-stained TEM micrograph illustrates the size and morphology of particles isolated by SEC. **(c)** Representative data of an antibody sandwich assay using SP-IRIS, which demonstrates the presence of EVs captured against tetraspanins CD9, CD63, and CD81, alongside control mouse-IgG (MIgG). Particle counts from fluorescently labeled detection antibodies are displayed, e.g., the first orange column from the left represents detected particles both captured by anti-CD9 and also labeled with anti-CD81. **(d)** Column scatter plot of SP-IRIS data from 7 representative clinical samples, each sample normalized to its total particle count for ease of comparison. Each circle represents the average expression value for a given clinical sample, with horizontal dashes representing the group mean and vertical lines one standard deviation from the mean.

5.3 Functionalization of SERS substrates to non-specifically capture anionic EVs and lipoprotein

For SERS measurement, we employed a commercially available substrate comprised of a silica nanowire matrix embedded with gold nanoparticle clusters, grafted to a conventional glass microscope slide (Ocean Insight). EVs distributed throughout this matrix (schematized in **Figure 5.3**) and localized in close proximity to the plasmonic gold experience the high electromagnetic fields generated by coupling between the excitation laser and localized surface plasmons on the matrix. This surface enhancement gives rise to immense amplification of otherwise weak Raman scattering signals, which can be detected via our custom-built confocal scanning Raman microscope. In preliminary testing,[91] we dried out a concentrated drop of EV-rich isolate onto the SERS substrate, but noted that this resulted in a dense impenetrable monolayer of dried biomass that masked any detectable EV-specific signal and largely prevented EV diffusion into the 3D nanowire mesh. On the other hand, simply dropping a small volume of EVs onto the SERS substrate, followed by washing, only resulted in modest EV retention in the mesh. To improve this, we developed a method of surface functionalization by cysteamine prior to EV sample addition. Cysteamine is a useful biofunctionalization linker,[209,259] with a terminal thiol group on one end that binds to the gold substrate and a free amine on the other end, effectively priming the surface with positive charge for non-specific capture of inherently anionic EVs and lipoprotein. We recently showed that cysteamine functionalization allows for excellent retention of EV-rich material even after several rounds of washing.[91] Following cysteamine-mediated EV adsorption, we imaged the substrate morphology with SEM (**Figure 5.3b**), which shows EVs localized to the surface of the nanowires, demonstrating their effective retention and proximity to plasmonic substructures for subsequent SERS measurement. Notably, anionic lipoprotein co-isolated with EVs from clinical biofluids would also be pulled down

to the cysteamine-functionalized surface and potentially subjected to plasmonic enhancement as well.[260,261]
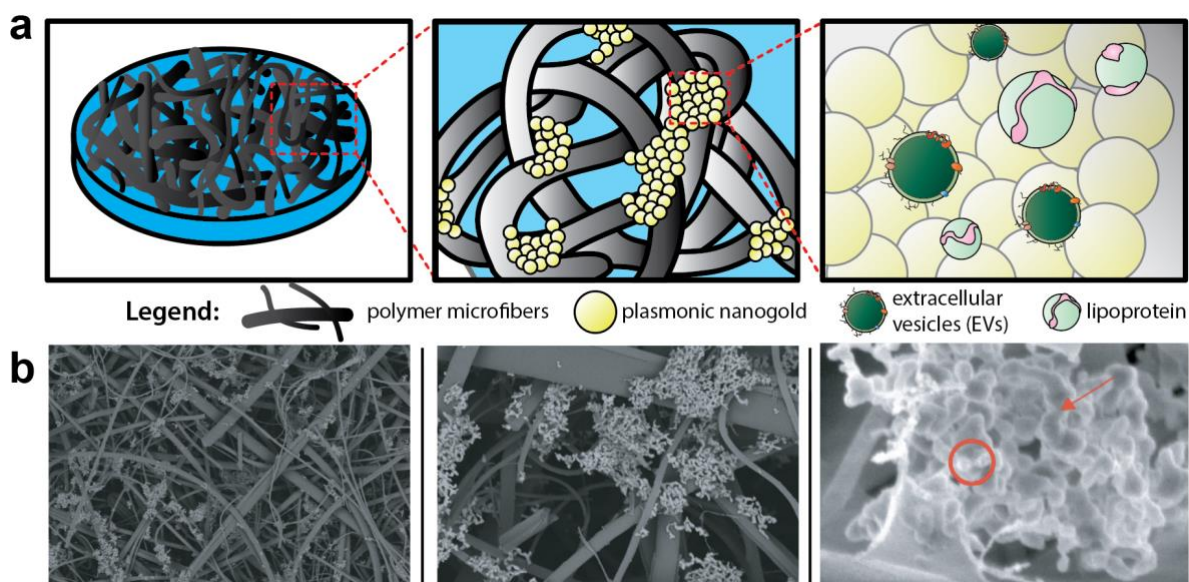
Figure 5.3: Porous plasmonic SERS substrates are used for label-free analysis of EVs and lipoprotein. We utilized a commercial SERS substrate based on plasmonic nanogold clusters embedded throughout a polymer microfiber matrix. As schematized by cartoon in **(a)** with corresponding images captured by SEM in **(b)**, EVs and lipoprotein particles can traverse the polymer network structure and localize to the plasmonic nanogold for subsequent enhancement. The substrate is pre-treated with cysteamine to increase efficiency of pull down of anionic EVs and lipoprotein to the surface. The red circle and arrow annotate bioparticles adsorbed to the nanogold surface.

During typical SERS analysis, the laser was swept across the substrate to randomly sample plasmonically active spots throughout. Across many randomly selected spots in the substrate, several subsequent sets consisting of twenty consecutive 1-second spectra were captured at each selected spot. Therefore, for a given sample condition across a single substrate, dozens of spectra were captured and analyzed.

Prior to EV analysis, lipoprotein analytical standards were measured from stock solutions, without SERS and substrates and then following incubation with SERS substrates (**Figure 5.4a-b**). Raman spectroscopy has been previously used to sensitively distinguish lipoprotein variants.[262] Here, samples are compared throughout using principal component analysis (PCA), which we have previously reported for reducing dimensionality of Raman spectral datasets.[93,95] PCA generates an intuitive visualization of multivariate data, capturing as much variability as possible and conserving the

pertinent information responsible for the major sources of data variability.[263] The analysis yields two commonly interpreted outputs; a principal component (PC) score plot and PC loading spectra. The PC score plots aid visual comprehension of the variance and groupings within the analyzed data, and the magnitude of differences (**Figure 5.4c**). The PC loading spectra (**Figure 5.4d**) report on the contribution of each independent variable (*i.e.*, spectral region) to the observed differences, and thus can be used to pinpoint the prominent spectral features that can further be assigned to encompass different chemical bonds, structures, and functional groups. Notably, each of the four classes of
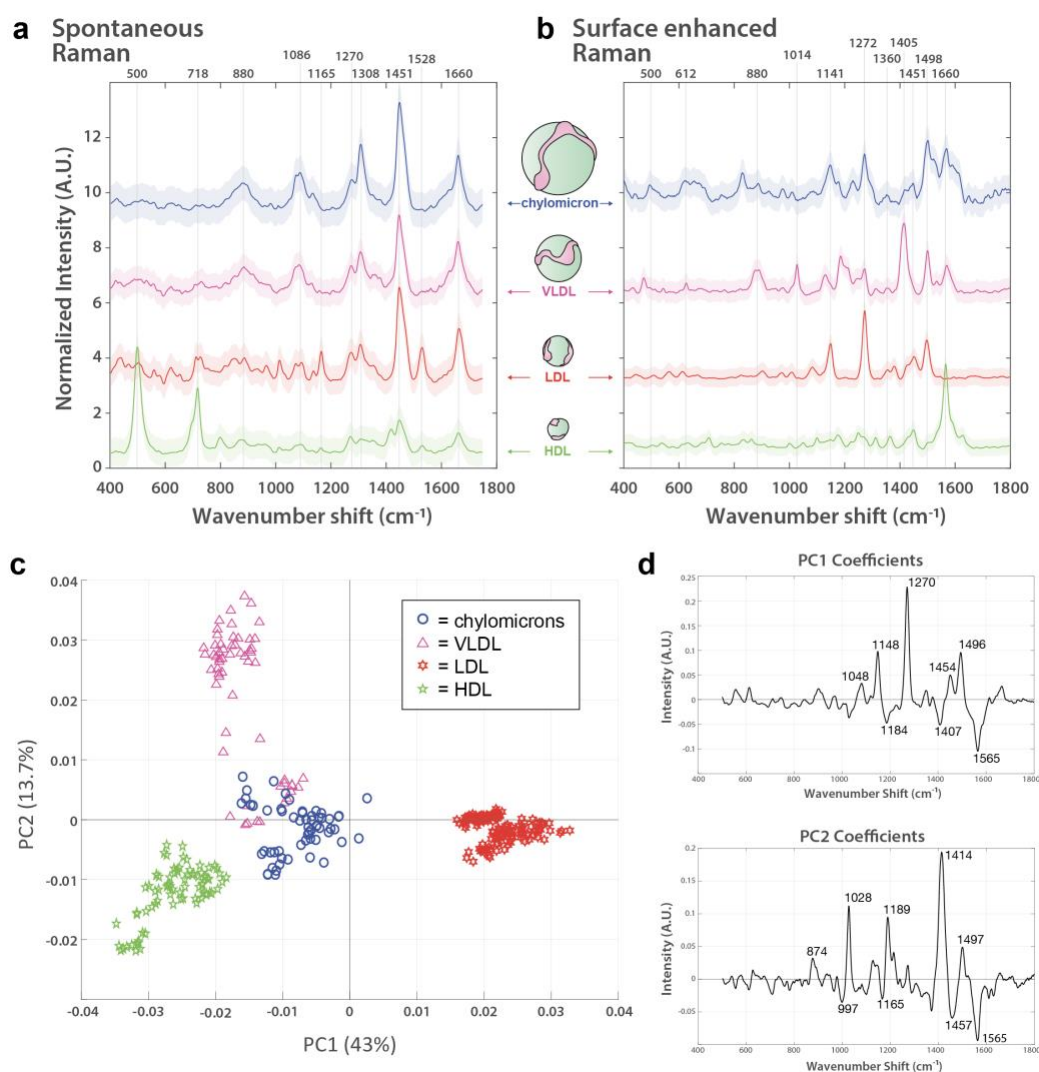
Figure 5.4: Lipoprotein analytical standards are readily distinguished by Raman scattering. **(a)** Spontaneous Raman and **(b)** surface enhanced Raman spectra for lipoprotein analytical standards. While SERS related peaks are different than their spontaneous counterparts, they are readily distinguished from each other. **(c)** Principal component analysis using PC1 and PC2 (together representing more than 56% of the total variability in the dataset), with loadings **(d)**, shows distinct separation of the lipoprotein subtypes according to spectral differences.

lipoprotein (chylomicrons, VLDL, LDL, and HDL) could be distinguished from one another in PC space following their interrogation by SERS substrate, as observed by the distinct clustering in **Figure 5.4c** along the PC axes represented by the spectral loadings in **Figure 5.4d.**

We have made efforts to fully assign the vibrational peaks driving variability across the datasets (annotated throughout this study's figures, *e.g.*, in **Figure 5.4d**), but caution against overinterpretation of single spectral peaks, particularly for SERS spectra which are often very dynamic in time during even a short measurement. While our full assignments for each peak of interest, according to literature references,[33,54–63] can be found in **Supplementary Table 5.1**, we comment throughout in the main text on the possible significance of certain major groupings of feature types (*e.g.*, when multiple peaks are indicative of lipids, nucleic acids, proteins, etc. for a given spectral loading).

For example, in the lipoprotein dataset, 43% of the sample variability is accounted for in PC1, which splits LDL from the other lipoprotein variants. The main peaks responsible for the variation in PC1 are an increase in 1048 cm^{-1}, 1148 cm^{-1}, 1270 cm^{-1}, and 1454 cm^{-1}, previously noted to correspond to carotenoid compounds that can associate with LDL (but to a lesser degree with HDL), as well as aliphatic chains of LDL-contained lipid species.[265,267] PC2 further stratified the remaining lipoprotein types, driven primarily by phospholipid type features. VLDL and chylomicrons displayed the most similarities to each other, as indicated by their proximity and slight overlap. This is somewhat anticipated, as VLDL is the first type of lipoprotein produced as chylomicrons get broken down by the liver.[245] Although these lipoproteins are all derivative of each other and chemically similar, it is clear that they each maintain unique differences and are distinguishable according to their SERS spectra.

5.4 EVs isolated from clinical biofluids using various methods show key compositional differences

We next analyzed EV isolates using the SERS assay. EVs were isolated from each patient sample using either UC, DG, or SEC techniques and analyzed by PCA. As evident in **Fig. 5.5a** using a representative PC score plot for patient C-1, diagnosed with nasal cavity squamous cell carcinoma, the various isolation methods are primarily responsible for driving the chemical differences across samples, as evident by their clear separation in PC space. For example, the band regions 926 cm^{-1}, 1005 cm^{-1}, 1323 cm^{-1}, and 1521 cm^{-1} seen in PC1 are related to nucleic acids signatures and are positive for all of the DG spectra (red) while the same regions are negative for SEC (pink) and UC (blue), implying that additional nucleic acid material is traveling to the same isopycnic spot as our EV preps. The accompanying negative PC1 loading regions of 1144 cm^{-1}, 1275 cm^{-1}, and 1485 cm^{-1} all relate to various lipid and protein signatures. This analysis implies that these lipid and protein signatures are more present in UC and SEC samples than in DG samples. This is a clear indication that each method co-isolates specific patterns of nucleic acids, lipids, and proteins in various amounts, and the chemical composition of these patterns differs depending on some extent to the isolation method.
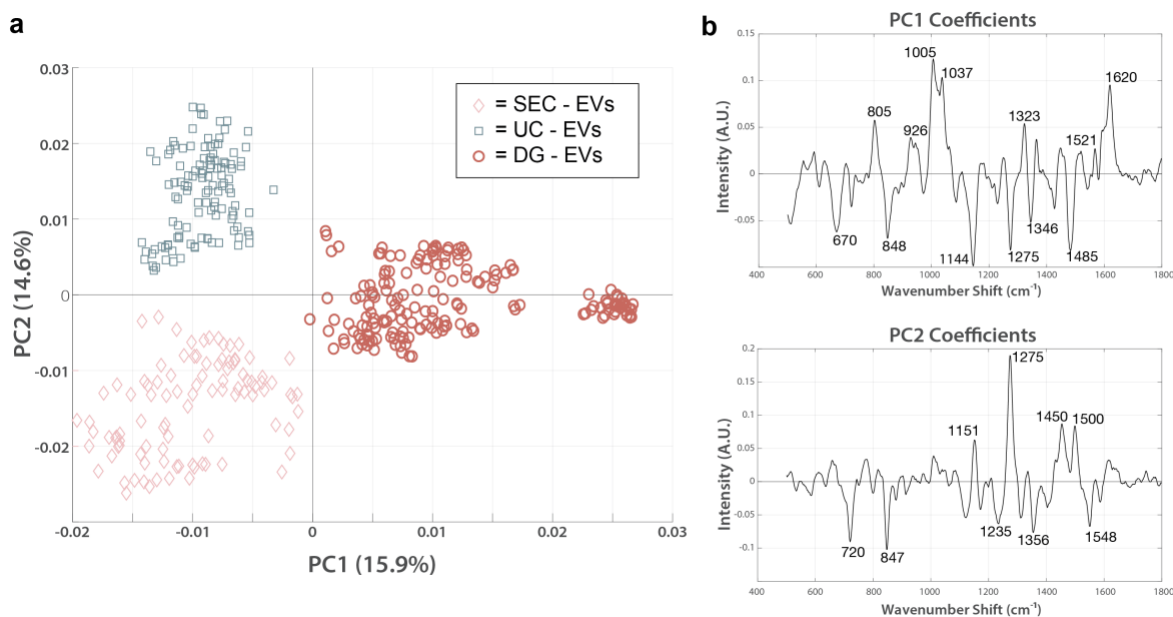
Figure 5.5: PCA of SERS spectra from EVs isolated by various methods are chemically distinct. Principal component analysis of SERS spectra from EVs isolated from patient C-1 (diagnosed with nasal cavity squamous cell carcinoma). Isolation methods of the same sample produce chemically different clusters **(a)** 2D principal component score plot (PC1-PC2) containing measurements from EVs isolated by either SEC (pink), UC (blue), or DG (red). Each marker represents a single measurement sampled across the SERS substrate after incubation with EV isolates. **(b)** PC1 and PC2 loading spectra reveal the chemical attributes responsible for the driving variation between populations.

Stratification along PC2 represents an increase in peaks 1151 cm^{-1}, 1275 cm^{-1}, 1450 cm^{-1}, and 1500 cm^{-1}, notable lipid and protein signatures. It is not clear whether these differences are due to varying extent of contamination by lipoprotein, so as an initial negative control we compared EVs isolated from an ovarian cancer cell line (SKOV-3). We measured the SERS spectra for SKOV-3 EVs isolated by both UC and SEC and plotted them against each other. Given that the cell lines are grown in culture media without lipoprotein, their released EVs should be free of the chemical signatures we gathered from the standards which makes them an appealing negative control. In fact, there was no separation from these two populations (**Supplementary Figure 5.1a**), indicating that no major differential accumulation of contaminants is taking place depending on the technique used. When plotted with the lipoprotein standards, the SKOV-3 EV SERS measurements revealed clear separation from all the different types of lipoproteins (**Supplementary Figure 5.1b**). The lack of overlap with

the signals indicates that there is no lipoprotein co-isolated with the *in vitro* derived SKOV-3 EVs, regardless of isolation method.

5.5 EV preparations spectrally cluster with lipoprotein standards based on isolation method

To assess the extent and type of lipoprotein signatures conceivably present in our clinical EV isolations, we analyzed the lipoprotein standards and EV isolations together. **Figure 5.6a** shows a representative figure for the patient sample C-1. In fact, the spectral features identified in PC1 (1270 cm^{-1}, 1454 cm^{-1}, 1497 cm^{-1}) are highly reflective of the overall chemical content of VLDL and LDL. EVs isolated by SEC (pink diamonds) shared similar protein and lipid signatures that were seen in the VLDL and chylomicron spectra (magenta triangles and red stars, respectively). VLDL and chylomicrons exhibit a high degree of overlap with EVs in the size range of particles purified by SEC, supporting our finding of similar spectra and interpretation that this means SEC-isolated EV preps co-isolate those particular lipoproteins. EVs isolated using either UC or DG (blue squares and orange circles in **Figure 5.6a**, respectively) have a much greater association with the HDL spectra (green stars). The position of the UC and DG in combination with the PC2 axis shows that they still have a higher enrichment of distinguishable lipid features (1180 cm^{-1}, 1376 cm^{-1}, and 1436 cm^{-1}; all report on lipid vibrations as shown in **Supplementary Table 5.1**) as compared to the HDL standard. Taken together we can determine that there is a correlation with the co-isolation of HDL when employing DG, a density-based isolation method, *i.e.*, specimen that have resembling densities co-locate in the same fraction(s) of the gradient solution. In all of the clinical EV samples we tested, similar trends for grouping were followed. We expected to see lipoproteins in the same size range as the EVs (chylomicrons, VLDL, and LDL) to group more consistently with EVs from SEC while those with the same density (HDL) would share higher proximity to the density-based EV isolation methods of UC and DG. The PC analysis supported this hypothesis and showed a strong correlation of the

grouping based on both size and density. Taken together, these findings indicate that different types of lipoproteins are present in varying amounts depending on which EV isolation technique is used.

5.6 Combination of isolation techniques leads to less lipoprotein contamination of the samples

To examine whether a multi-step isolation approach could remove all types of lipoprotein, EV samples that were first isolated by UC were further purified by subsequent SEC. Samples were concentrated and measured using the SERS assay, then mapped with the same lipoprotein standards in PC space for evaluation. The resulting plot showed a clean separation of the dually isolated sample from all of the lipoprotein present (**Figure 5.6c-d**). From the positive spectral features of PC2 we can note that the VLDL, chylomicrons, and LDL exhibit a very different lipid and protein chemical profile from both HDL (as previously noted) and the dually isolated EV sample. The PC2 loading peaks at 1005 cm^{-1} (phenylalanine), 1280 (CH$_2$, CH$_3$ deformation/C-N stretching), 1560 cm^{-1} (tryptophan), and 1636 (amide I) are pronouncedly present in HDL and UC+SEC compared to VLDL, chylomicrons, and LDL, which points to the protein-enriched chemical contents in HDL and UC+SEC samples. On the other hand, the peaks at 1124 cm^{-1} (C-C and C-N stretching of proteins and lipids), 1188 (C-C or C-O e.g., phospholipids), 1415 cm^{-1} (CH rocking in lipids), and 1493 cm^{-1} (conjugated C=C vibrations) could evidence the abundance of lipid-related components in VLDL, chylomicrons, and LDL, simultaneously less represented in HDL and UC+SEC samples. Of note, even though the PC1 analysis first implied that there might had been VLDL/LDL signatures in the UC+SEC EV isolate, the PC2 analysis showed that the EV isolate can be distinguished from these lipoproteins. Hence, the observed SERS peak similarities in PC1 analysis highly likely stem from the fact that the peaks can represent multiple chemical entities (*e.g.*, the peak at 1271 cm^{-1} can be assigned to amide III bond vibrations in EV proteins in the UC+SEC sample, in unison representing C=C bonds in fatty acids
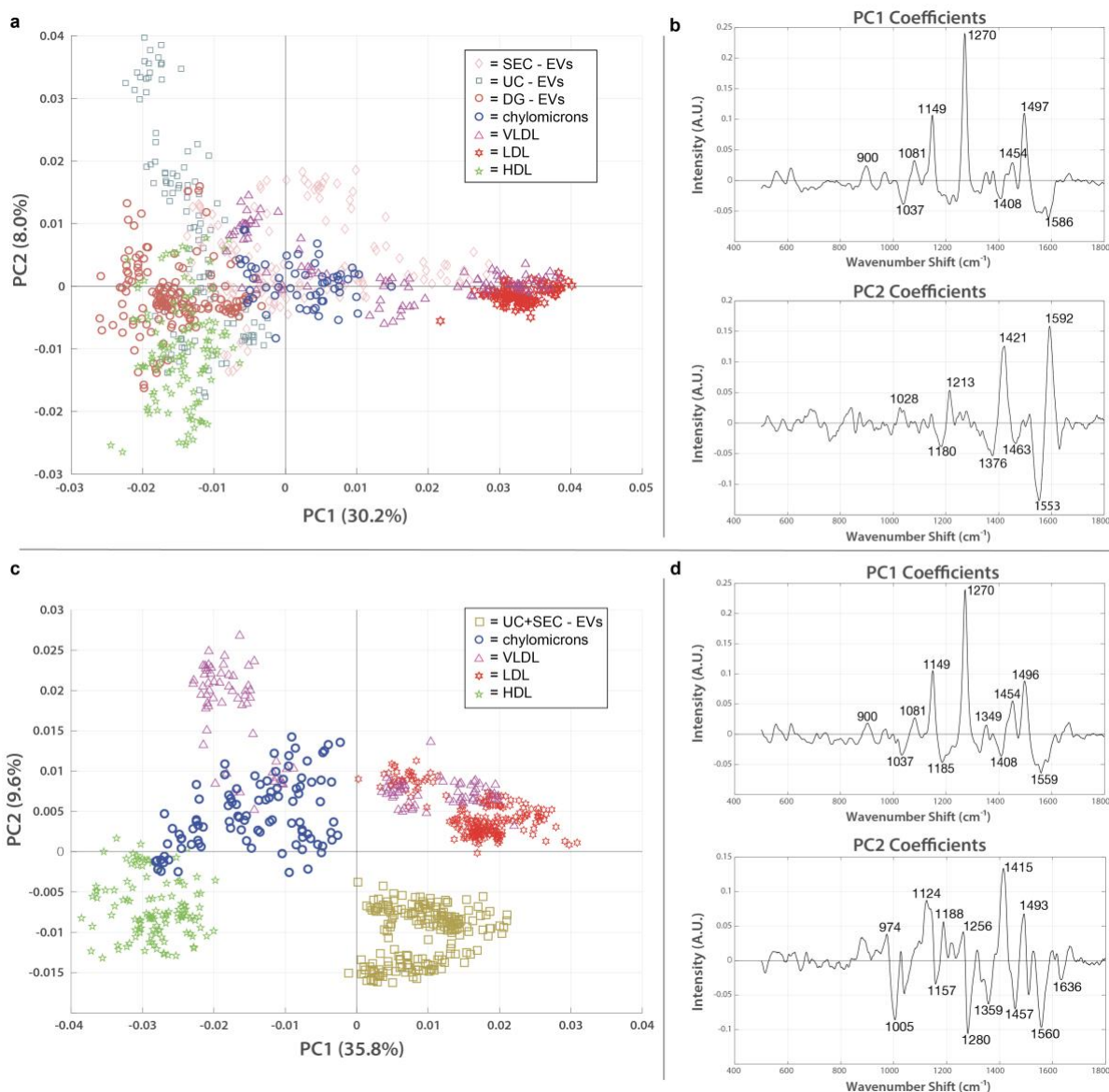
Figure 5.6: PCA of SERS spectra from clinical EVs isolated across various methods compared to lipoprotein standards reveals extent of contamination. PCA score plots and loading spectra for EVs isolated by different methods and lipoprotein standards. EVs group with lipoprotein populations to which they are more chemically similar. **(a)** Single isolation methods for EVs using either SEC (pink diamonds), UC (blue squares), or DG (orange circles) group differently with chylomicrons (blue circles), VLDL (magenta triangles), LDL (red stars), and HDL (green stars). **(b)** PC1 and PC2 loadings indicate the chemical peaks responsible for the greatest amount of variation between samples in panel (a). **(c)** Dual isolation strategy of EVs using UC followed by SEC (brown squares) has no overlap with the lipoprotein standards. **(d)** PC1 and PC2 loadings representing the spectral areas responsible for the majority of variation between samples in panel (c).

and aliphatic chains of LDL-contained lipid species). The capability to project the data in PC space containing multiple directions is the strength of our multivariate analysis approach. Thus, SERS analysis is a viable tool to validate the purity of the isolate. To our knowledge, this is the first direct

indication that dual isolation using UC and SEC in tandem is more capable of purifying EVs from lipoprotein.

5.7 Cancer diagnostic performance of the SERS platform is largely unaffected by EV isolation method

Although we saw evidence that the type of isolation method used changes the chemical signature of the EV samples, we were interested in evaluating and quantifying the capabilities of our SERS platform to distinguish cancer from non-cancer, regardless of the technique used. Following variable reduction by PCA we applied a straightforward machine learning (ML) approach using either supervised linear discriminant analysis (LDA) or quadratic discriminant analysis (QDA), which have attained notable interest in vibrational spectroscopy applications.[126,268,269] We refer to the methods as PCA-LDA and PCA-QDA, respectively. In essence, LDA and QDA are relatively simple boundary discriminant methods that separate sample classes or groups. LDA presumes a single variance-covariance matrix across classes, resulting in linear boundaries that are straight lines or hyperplanes dividing the variable space into categorized regions. QDA, in turn, assumes that the variance-covariance matrices are different for each class, yielding quadratic boundaries that are quadratic curves or hyperplanes dividing the variable space. Thus, QDA represents a potentially more flexible modeling approach since it allows for discriminating classes wherein the class-specific covariance matrices are significantly different. Although QDA is considered to perform well for normally or multi-normally distributed data, requiring minimal optimization, and being comparably immune to overfitting,[269] the superiority of LDA versus QDA is rarely known *a priori*.

Therefore, we tested PCA-LDA and PCA-QDA for UC, DG, SEC, and UC+SEC isolated samples in the context of cancer detection and diagnostics (**Figure 5.7**). The PC scores were used as input data for LDA/QDA, and to avoid overfitting,[270] we chose to use either the first two or three PCs (PC1-PC2 or PC1-PC3, respectively) as input features for the classifiers. In order to effectively

compare these models, we established quality performance metrics consisting of accuracy (*i.e.*, error rate), sensitivity, and specificity to discriminate cancerous samples from non-cancerous controls. The full metrics for each approach is shown in **Supplementary Table 5.2.** The best performing model (*i.e.*, most accurate) for each isolation method is plotted in **Figure 5.7**. Panels a, d, g, and j show the 2D or 3D PC space with the linear or hyperplane decision boundary drawn in dark grey, cancerous samples in red, non-cancerous control samples in blue, and misclassified data points as yellow circles. Corresponding PC loadings for the first two PCs are shown in panels b, e, h, and k, along with annotated peaks color coded according to their presence in the raw cancer or non-cancer spectra. **Supplementary Figure 5.2** displays the global mean and standard deviation for the processed SERS spectra for each isolation methodology, along with annotated wavenumber regions corresponding to the numbers shown in the **Figure 5.7** loadings. The panels c, f, I, and l display the confusion matrix accompanied with the performance metrics table for sensitivity and specificity.

DG, SEC, and UC single isolations all resulted in practically equivalent accuracies of 98.3%, 97.8%, and 98.0%, respectively. Yet the same model was not used for each. DG and UC were most successful with a QDA model, while SEC performed better with an LDA model. In each of the isolation methods, the inclusion of a third PC made only a slight difference (**Supplementary Table 5.2**). Notably, the combination of UC+SEC, which in principle would result in a more highly purified sample, performed much worse than either of the individual methods, with accuracies ranging from 85%-86.5% across the model classifiers. For the three individual isolation methods, each of the tested four models (PCA-LDA with PC1-PC2, PC-LDA with PC1-PC3, PCA-QDA with PC1-PC2, and PCA-QDA with PC1-PC3) demonstrated robustness to detect cancer and diagnose various types of head and neck cancers adequately. According to our analyses, the DG method using PCA-QDA with PC1-PC3 stood out as the most accurate (98.3%) and sensitive (98.3%) isolation procedure. DGA

with PCA-LDA using either the first two or three PCs had 100% specificity (**Supplementary Table 2**).

Supplementary Figure 5.2 provides additional insight into the chemical groups driving the separation of cancer and non-cancer samples. In those spectra, particular chemical features are annotated that distinguish between the two cohorts, while virtually equal peaks/band regions between cancer and non-cancer samples were excluded. The band in the 1000-1040 cm^{-1} area is very active across all the isolation methods; this specifically stands out among the non-cancer control samples. As this region can be associated to *e.g.*, symmetric ring breathing in phenylalanine and/or CH_2CH_3 bending in lipids, it is conceivable that these chemical features are diminished in EVs originating from cancerous cells. Another possibility is that the total vesiculome in a cancer burdened system may undergo metabolic changes resulting in discernible EV representation. In UC+SEC isolation approach, however, the control samples have less of the 1000-1040 cm^{-1} properties and are correspondingly weaker at discerning
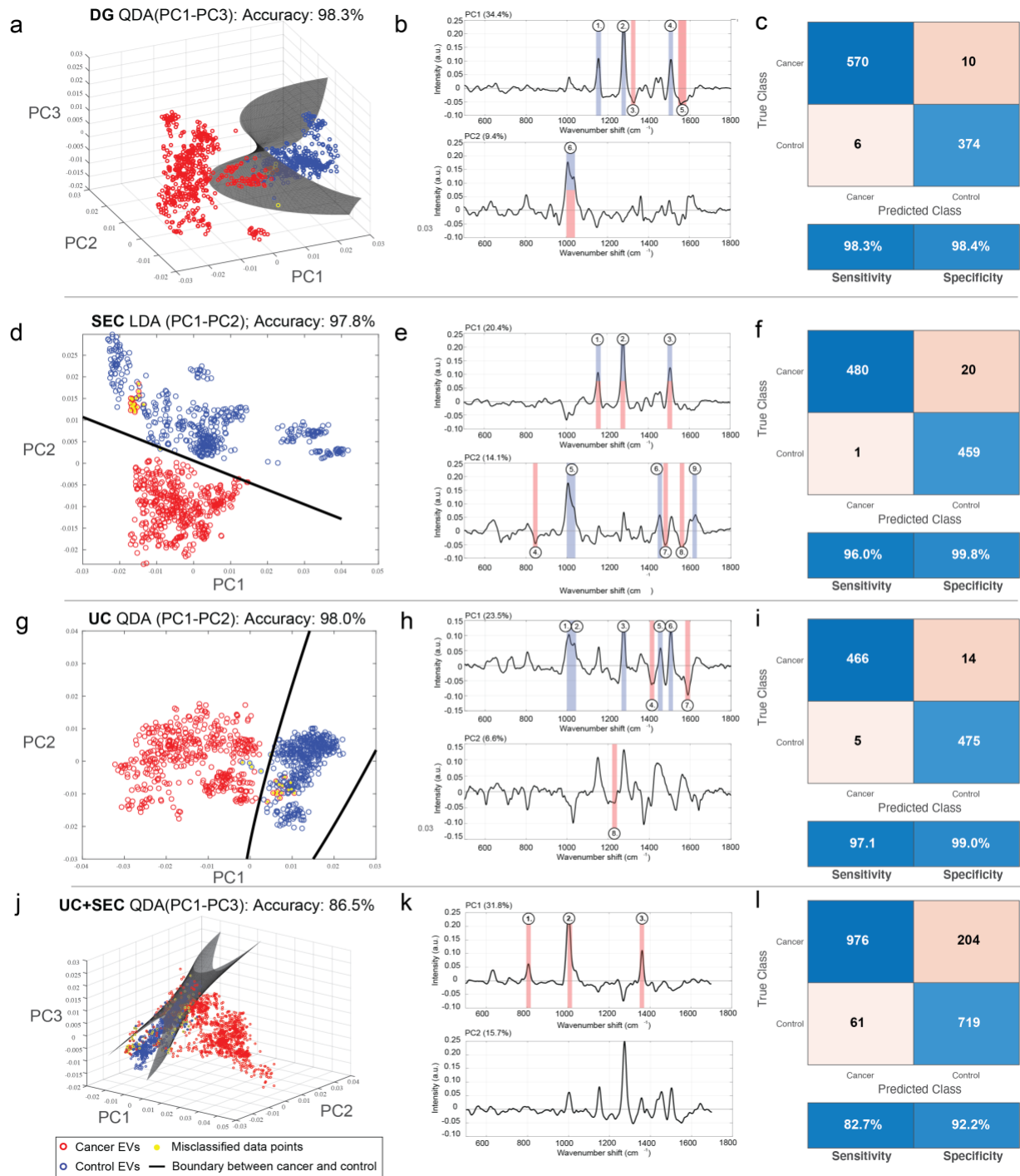
Figure 5.7: ML classification of SERS spectra shows accuracy is largely unaffected by EV isolation methodology. EVs isolated from head and neck cancer patients (red circles) and non-cancerous control patients (blue circles) either by DG **(a-c)**, SEC **(d-f)**, UC **(g-i)**, or UC+SEC (**j-l**) were measured using the developed SERS assay. **(a,d,g,j)** Following PC analysis, various machine learning classification approaches were tested; shown is the best performing classifier for each isolation type in terms of overall accuracy, either using LDA or QDA, and testing over the first two or three PCs. Decision boundaries are shown as lines (a,b) or as a hyperplane (c,d) depending on the dimensions of best fit. **(b,e,h,k)** Loadings for the first two PCs, including annotated peaks corresponding to **Supplementary Figure 2**, highlighting the driving factors for discriminating cancer features. **(c,f,I,l)** Confusion matrices and performance metrics derived from the ML analysis, including sensitivity and specificity.

between cancer and non-cancer samples. While the explicit interpretation for this observation remains unclear, this example highlights the benefits of the developed SERS method being relatively immune to the effect of isolation-dependent contaminants in cancer detection procedures.

The 1500-1515 cm^{-1} region is also prominent in all control samples isolated by DG, SEC and UC, but absent in both control and cancerous UC+SEC samples. Predominantly attributed to the vibrational modes from C=C conjugations, we foresee similar tendency to the aforementioned 1000-1040 cm^{-1} region; the chemical composition of EVs experiences changes in the diseased state. This may suggest that the unsaturated double bonds in various chemical structures become decimated by the acidic and hypoxic microenvironments of tumor cells. On the other hand, cancerous samples isolated by DG, SEC and UC share chemical features reported by the region 1540-1580 cm^{-1}. Within this region, there exists majorly protein-related signatures such as tryptophan and amide II vibrations. Again, it is a persistent finding regardless across the single isolation methods and possibly reports on the altered protein content of cancerous EVs.

DG (control) and SEC (control and cancerous) samples are mutually characterized by the region 1140-1160 cm^{-1} that can be assigned to multiple plausible structures: C-C vibrations in lipids, C-N amide bonds in proteins, or carotenoids. Similarly, control samples isolated by SEC and UC have mutual spectral features at 1445-1465 cm^{-1}, which is an established marker area for CH rocking in lipids and CH_2/CH_3 vibrations in lipids and proteins. These represent further examples whereby chemical changes between cancerous and control samples can be observed over different isolation platforms.

The most unique spectral feature that differentiates cancerous DG samples from the controls is the region at 1540-1580 cm^{-1} mainly reporting on proteins such as tryptophan and amide II vibrations. For SEC, the ranges 840-855 cm^{-1} (nucleic acids and *e.g.*, ring deformation in tyrosine) and 1550-1570 cm^{-1} (tryptophan, amide II) discern cancerous samples from the controls. The SEC isolated

samples have the most spectral areas in common as a whole. For UC, the regions 1405-1415 cm^{-1} (CH rocking in lipids) and 1580-1600 cm^{-1} (amide II and nucleic acids) separate cancerous samples from the non-cancer controls. Taken together, it is clear that overall diagnostic performance is largely very high across single isolation methods, the particular chemical differences driving each separation are not the same.

5.8 Discussion

Many studies employing EVs isolated from cell culture supernatant lack the additional biomolecules that exist within complex biofluids. The influence of these additional molecules and their assemblies could have important consequences in therapeutic and diagnostic EV research. Particularly when it comes to dosing studies, it is vital to know how many EVs are present versus other co-isolated biomolecules. Moreover, the diagnostic capabilities of an EV-based assay might even benefit from the additional information the co-isolated specimen can provide. Yet in many basic research settings, having a pure EV sample is the most beneficial for better understanding the fundamental biological functions and chemical structures of EVs. Moreover, modern drug discovery endeavors are increasingly aimed towards developing safe and effective EV nanoformulations for targeted therapies. Robustly producing highly pure EV preparations and assessing their level of purity, *e.g.*, by SERS are the cornerstones of such developmental steps. We show here that lipoprotein is being co-isolated with EVs to various extent based on isolation methodology, which can be assess using a label-free spectroscopic approach. The use of a combination of both density and sized-based isolation techniques would logically provide a purer EV population, but we found that in that case, diagnostic sensitivity is decreased in this cohort of patients.

Notably, the ML classifiers used here are minimally prone to observer-dependencies, inter- and intra-observer variabilities, and are operator-friendly for various types of classification schemes involving large spectral data sets. Overall, the performance of different ML strategies is predominantly

dependent on the data structure. Methods such as support vector machines (SVM) or learning vector quantization (LVQ) can be susceptible to overfitting for normally or multi-normally distributed data whilst conceivably performing better for more complex data structures. Signal analysis by PCA followed by LDA has been successfully applied to discriminate EVs in previous work.[145,271] In this limited dataset, LDA and QDA each performed better in some cases, and worse in others, suggesting that there is not a one-size-fits-all solution. Our future emphasis will be integrating several ML approaches into one overarching evaluation and comparing their capabilities in real clinical settings.

One notable feature of this study is the ability to carry out such an extensive comparison between isolation methods on reasonable volumes of clinical biofluids. The sample input volumes for many contemporary EV characterization methods, including proteomics and genomics analysis, electron microscopy, and Western blot, preclude its use in testing multiple isolation methods on a single clinical sample for downstream characterization. Therefore, many studies focus solely on EV samples derived from cell culture supernatant, limiting their clinical relevance. SERS, on the other hand, requires less than a few microliters of sample volume per measurement, permitting its applicability in such a comparison study and in clinical diagnostics platforms at large.

However, some limitations and caveats for these results remain. We analyzed a small and focused dataset from a specific family of cancers (head and neck), and it is not clear how generalizable our finds are to other cancers and disease types. Also, there are many other types of contaminants besides lipoprotein in human biofluids that can pollute SERS spectra, whose influence will need to be investigated in future studies. We showed that a dual isolation method can successfully remove lipoprotein present in the clinical samples, but in some case, lipoproteins can contribute to diagnostic information about an individual's disease state, thus are not always undesirable. In any case, the SERS platform provides enough accuracy to not be majorly influenced by contamination of differential

combinations of lipoprotein, indicating that clinical samples may not need to be subjected to rigorous isolation procedures for input into diagnostic platforms. Yet for such application, it is true that challenges remain, given that the SERS process itself if is inherently highly variable, with noted reproducibility issues and a high degree of user experience needed to analyze data. Beyond that, scaling up production of SERS substrates is challenging, often requiring expensive lithography equipment to ensure consistent signal acquisition. Future projects will focus on expanding to greater numbers of clinical samples and variety of cancers, examining the diagnostic influence of additional biomolecules beyond lipoproteins present in EV preps, and automating the SERS measurement process for successful implementation in a clinical setting.

5.9 Supplemental Information

Table S5.1: Chemical assignments for annotated peak regions in **Figures 4 – 8** in the main text, including literature references. When a specific peak of interest from our analysis was contained with a few (<5) inverse centimeters of a literature value, we replaced the specific value with a range rounded to the nearest value of "5" or "10" for ease of interpretation, given that our spectral resolution is within an error of 5 cm^{-1}.

Wavenumber region (cm^{-1})	**Chemical assignment**	**Reference**
720	Amino acids	[94]
790-795	Nucleic acids	[93,213]
840-855	Nucleic acids and e.g., ring deformation in tyrosine	[213]
900	Carbohydrate-related; proline/valine/glycogen	[155,264]
926	C-C ring stretching e.g., proline, nucleic acids	[213]
1005-1010	Symmetric ring breathing; phenylalanine	[94]
1025 – 1050	CH$_2$CH$_3$ bending, e.g., lipid	[92,94,96,265]
1120 – 1190	C-C, e.g., lipid; C-N amide in proteins	[92,94,96,97,265]
1149	Carotenoids	[265]
1165	Carbohydrate-related	[92]
1235	C-N stretching + N-H deformations; amide III proteins	[90]
1265 – 1280	Amide III protein and C=C fatty acid	[90,94]
1282	CH$_2$, CH$_3$ deformations; C-N stretching	[90]
1320 – 1360	CH$_2$CH$_3$ in nucleic acids	[90]
1376	CH$_3$ symmetric in lipid	[90]
1405 – 1440	CH rocking in lipid	[92]
1450 – 1465	CH$_2$/CH$_3$, lipid and protein	[257]
1480 – 1485	C-H, lipid and protein	[90]
1495 – 1515	Vibrations from C=C conjugations	[92]
1520 – 1565	Tryptophan	[90]
1545 – 1590	Amide II	[218][266]
1603	Cytosine and phenylalanine	[92]
1620	DAMP/C=C protein	[90]
1630-1650	Amide I, C=C	[95,208]
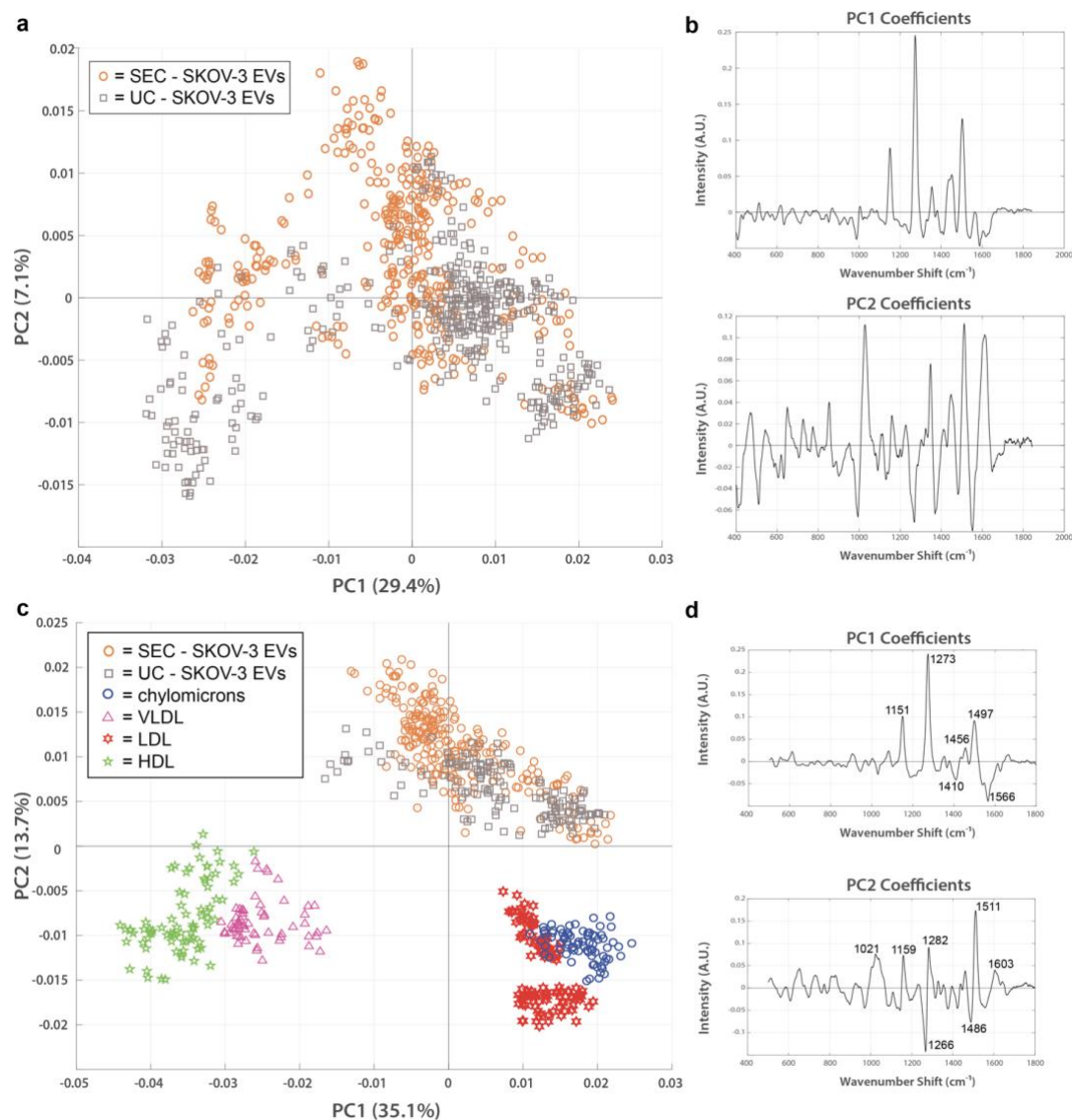
Figure S5.1: PCA analysis of EVs isolated from cell culture supernatant compared to lipoprotein standards. (a) EVs isolated from SKOV-3 cell culture supernatant are chemically similar to each other regardless of which isolation method is used. EVs isolated by SEC (orange) and UC (gray) heavily overlap in PC space without clear separation along their major principal components. (b) PC1 and PC2 loadings represent the greatest amount of chemical variation between samples in panel (a). (c) When analyzed with the lipoprotein standards, there is clear separation between the EVs and lipoprotein subpopulations, indicating a lack of chemical overlap between the species. (d) PC1 and PC2 loadings for panel (c). The positive peaks driving this separation indicate carbon-carbon and carbon-nitrogen stretching and deformations in proteins and lipids (1021 cm^{-1}, 1159 cm^{-1}, 1282 cm^{-1}), as well as unsaturated fatty acids (1511 cm^{-1}).
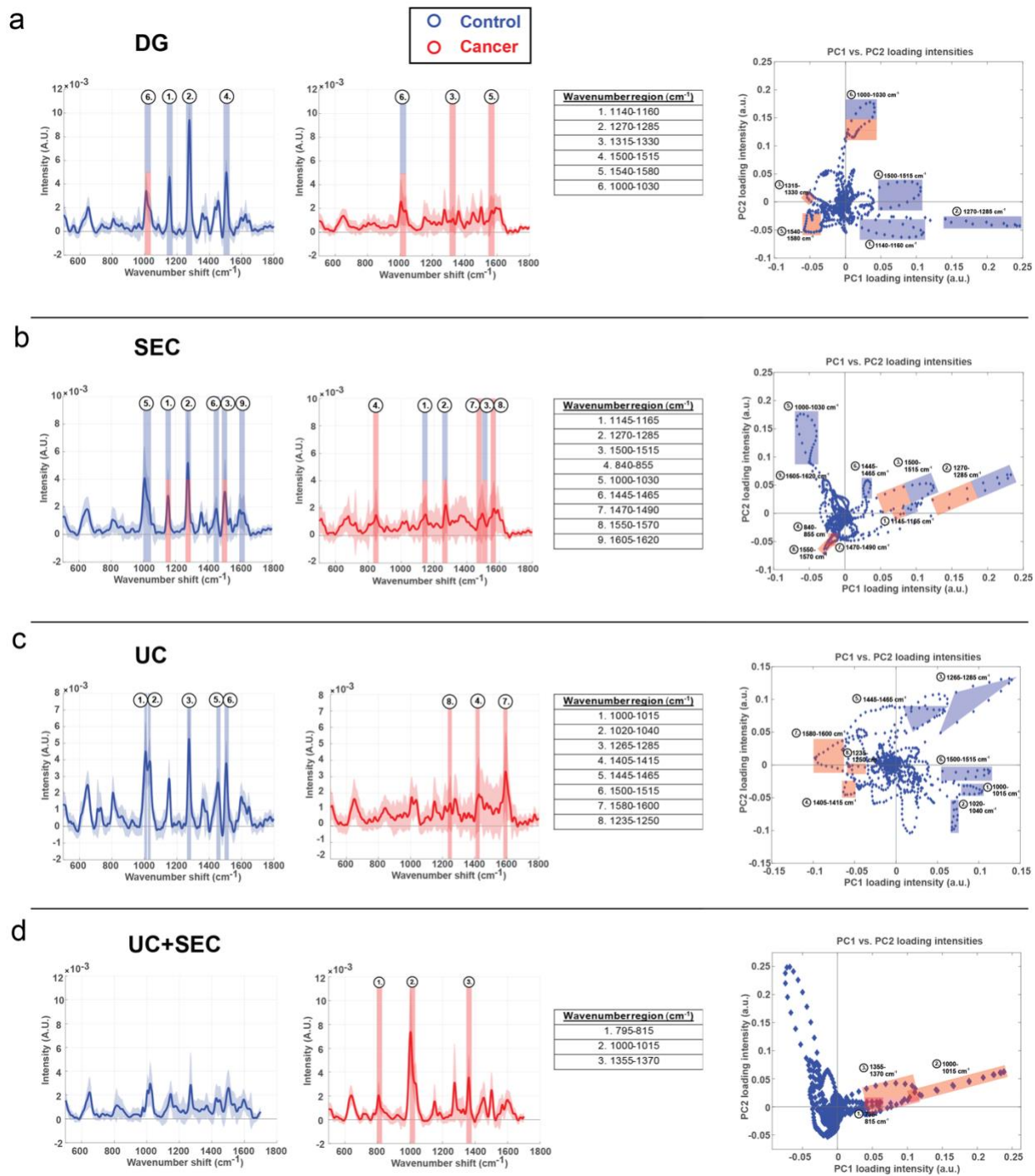
Figure S5.2: Mean and standard deviation of SERS spectra for EVs isolated from clinical samples. Spectral features for EVs isolated by either (a) DG, (b) SEC, (c) UC, (d) UC-SEC. Blue color denotes EVs isolated from non-cancerous control patients and red represents EVs from head and neck cancer patients. The prominent spectral regions identified by the PCA are color-coded by showing blue/red color for unique or blue-red for shared spectral features across cancer and non-cancer samples. As a visual guide, the PC1 versus PC2 loading intensities are displayed on the right-hand side of each panel. Influential spectral areas are annotated with 1-9 for each isolation method using outward-extending loops for ease of matching to the loadings. Peaks/bands providing negligible separation information are excluded.

5.10 Conclusions

Here we have conducted a study using label-free and non-destructive SERS measurements to assess the level of lipoprotein contamination across clinical samples isolated in several ways. We found that the type of lipoproteins co-isolated with a given EV preparation varied depending upon the technique that was used. EVs isolated by SEC grouped more consistently at the same locations as chylomicrons and VLDL/LDL, while EVs isolated by UC and DG shared more overlap with each other and HDL, indicative of their relative extent of contamination by those lipoprotein types. A protocol of subsequent UC and SEC largely eliminated lipoprotein contamination as shown by PC analysis of SERS spectra. Therefore, if striving for purer EV samples to use in research experiments, a dual isolation method may be the most effective at removing these distinct contaminating components. We also devised four different ML approaches in order to evaluate the cancer detection and diagnostics capabilities of the studied SERS platform. In terms of cancer detection, neither the isolation method used, nor the ML model greatly affected the sensitivity and specificity to distinguish between cancerous and noncancerous samples, which in most cases was greater than 97%. In terms of cancer diagnostics, the best overall performance (accuracy = 98.3%) was achieved using the DG isolation method and a PCA-QDA discriminant classifier with PC1-PC3 scores as input features. However, SEC and UC isolations also achieved accuracies of 97.8% and 98%, respectively. Taken together, our SERS platform was sensitive enough to tease out cancer-specific signatures that remained unaffected by the presence of additional co-isolated biomolecules, showing that the label free diagnostic ability was effective across many different sample preparations.

Chapter 6: Homogenous high enhancement surface-enhanced Raman scattering (SERS) substrates by simple hierarchical tuning of gold nanofoams

Context: Here we focus on the development of useful SERS materials that can be translated to clinical use. We developed gold nanofoams that were simple and quick to create while maintaining high Raman enhancement and easily integrating into simple filters. This work shows the promise of such in-house synthesized materials to overcome the obstacles current commercial SERS substrates face in their clinical translation.

6.1 Introduction

Anisotropic metallic nanomaterials, including nanorods, nanowires, nanostars, nanourchins, and nanofoams, have gained traction in a wide variety of applications due to their unique chemical and physical properties.[272] These versatile materials exhibit high chemical stability and biocompatibility and can be readily tuned for enhanced near-infrared (NIR) optical absorption with large extinction cross-sections. As such, they have been broadly applied in catalysis[273], electrochemistry[274], and sensing of chemical warfare agents or environmental pollutants.[275] Uses in biomedical platforms as photothermal agents, drug delivery carriers, and biosensing materials[276–278] have also been shown.

Compared to the other anisotropic nanomaterials, applications of nanofoams have lagged, in part due to their synthetic and structural complexity compared to particle formulations. Nanofoams are porous nanomaterials typically created from copper,[279] silver,[280] or gold.[281,282] They are most commonly fabricated by chemical etching of biphasic mixtures of metals in the presence of strong acids that de-alloy the sample to leave behind a porous phase.[283] Other fabrication methods employ biopolymers in combination with autoclave heat treatments to form networks after hydrothermal synthesis[284] or use halide ions to induce aggregation of gold nanoparticles (AuNPs) to form 3D networks.[285] More complex methods utilize electrodeposition and sintering.[286] Each

of these has various limitations, either relying on dangerous precursors with high environmental hazards (e.g., concentrated nitric acid[283]) or featuring complex procedures resulting in nanofoams that are difficult to structurally tune. For example, control over pore size and tortuosity are important for biosensing applications, such as concurrent point-of-use filtration and sensing via optical readout, yet current methods are unable to easily tune these parameters.[283]

A central application of nanofoams where precise synthetic control is desired for effective biosensing readout, as enabled by their NIR optical activity, is surface-enhanced Raman scattering (SERS). SERS is an attractive biosensing tool, as it is non-destructive, label-free, highly sensitive, provides a detailed chemical fingerprint of the sample, and is not influenced by water, meaning it can be performed in aqueous solutions such as wastewater or complex human biofluids.[287] SERS is an ultrasensitive extension of spontaneous Raman scattering. While inherently weak, nanoscale anisotropic metallic architectures, including nanofoams, can dramatically enhance the Raman signal via the SERS effect.[287] A SERS/Raman spectra is comprised of peaks corresponding to numerous vibrational and rotational modes arising from a given chemical sample, providing sensitive and specific information about which molecules are present.[288] This information has been broadly applied in biosensing to detect and diagnose diseases, such as cancer,[289] diabetes,[290] cardiovascular diseases,[291] and neurological diseases.[292]

One of the main obstacles to clinical translation of SERS is the nature of commonly used substrates, the best of which are typically created with expensive, specialized lithography equipment to pattern delicate nanostructures onto microscale planar surfaces.[287] It remains a grand challenge to rapidly and cost-effectively synthesize highly tunable hierarchically-ordered macroscale substrates with nanoscale SERS active features. Current tactics to generate such materials employ large-scale solution-phase synthesized anisotropic nanomaterials like nanorods and nanourchins deposited onto surfaces to form SERS active substrates.[293] Other shapes such as nanostars[294], nanocubes,[295]

and nanotriangles,[296] typically made from silver, have also been used. Yet these approaches are difficult to reproduce, often synthetically complex (necessitating several steps of inorganic chemical reactions and purification), and do not result in tortuous materials (e.g., foams) that could be used for in-line filtration. Additionally, nanoparticle deposition on planar surfaces often results in heterogeneous drying patterns with large spot-to-spot enhancement variation. Quantitative analysis of analytes using heterogeneous substrates is challenging since one cannot readily determine whether signal-intensity fluctuations are a result of analyte concentration or rather distribution and quality of "hot spots" on the substrate. There is a need to develop solution-phase synthesized macroscale nanofoams comprised of plasmonic metals for homogenous SERS activity and sensing.

Here we introduce a new gold nanofoam (AuNF) material with nanoscale features endowing high, homogenous SERS enhancement and with a tunable porous structure for potential in-line filtration and sensing applications. These AuNFs are easily synthesized via a rapid, green, one-pot, four-ingredient mixture at room temperature. Critically, our new synthetic scheme (Fig 1) allows for control over the macro-, micro-, and nano-scale features. Highly tunable microscale pore sizes are controlled by the starting concentration of the two starting ingredients, a gold salt, and a citrate reducing agent. Nanoscale roughening is achieved via a subsequent gold deposition step and sonication. Macroscale structure is achieved by drop-drying as-synthesized AuNFs onto a paper filter. The resulting roughened nanofoam (RNF) assembly has high and homogenous Raman enhancement factors approaching and even surpassing lithographically produced commercial substrates.

6.2 Development and synthesis of gold nanofoams

We developed the AuNF synthesis scheme (**Figure 6.1a**) using a one-pot aqueous chemical reaction, mixing gold (III) chloride with trisodium citrate dihydrate in a round bottom flask at room temperature, as adapted from a recent report.[282] The effective microscale pore size and nanofeatures could be tuned by varying the ratios of the two reagents ($R = C_{citrate}/C_{gold}$). Typical experiments used

an R=12 ratio of citrate to gold. Due to the slow reduction of the gold salt by the moderate citrate reducing agent, several intermediate structures are formed over the course of 6 h, each of which can be isolated by quenching the reaction via centrifugation and subsequent washing in ultra-pure water (**Figure 6.1b**). The reaction starts as a pale-yellow color that turns clear within a few seconds of stirring. After ~45 min the solution turned gray and an intermediate structure resembling nanotadpoles is obtained.[282] After 4 h, integrated nanowire networks form as tadpoles coalesce. As the reaction proceeds to 6 h, the gold structures continue to grow and fuse, finally creating a three-dimensional nanofoam structure. UV-VIS spectra were obtained at each of the intermediate time points to track the AuNF evolution (**Figure 6.1b**). As the foams continue to grow, they lose the
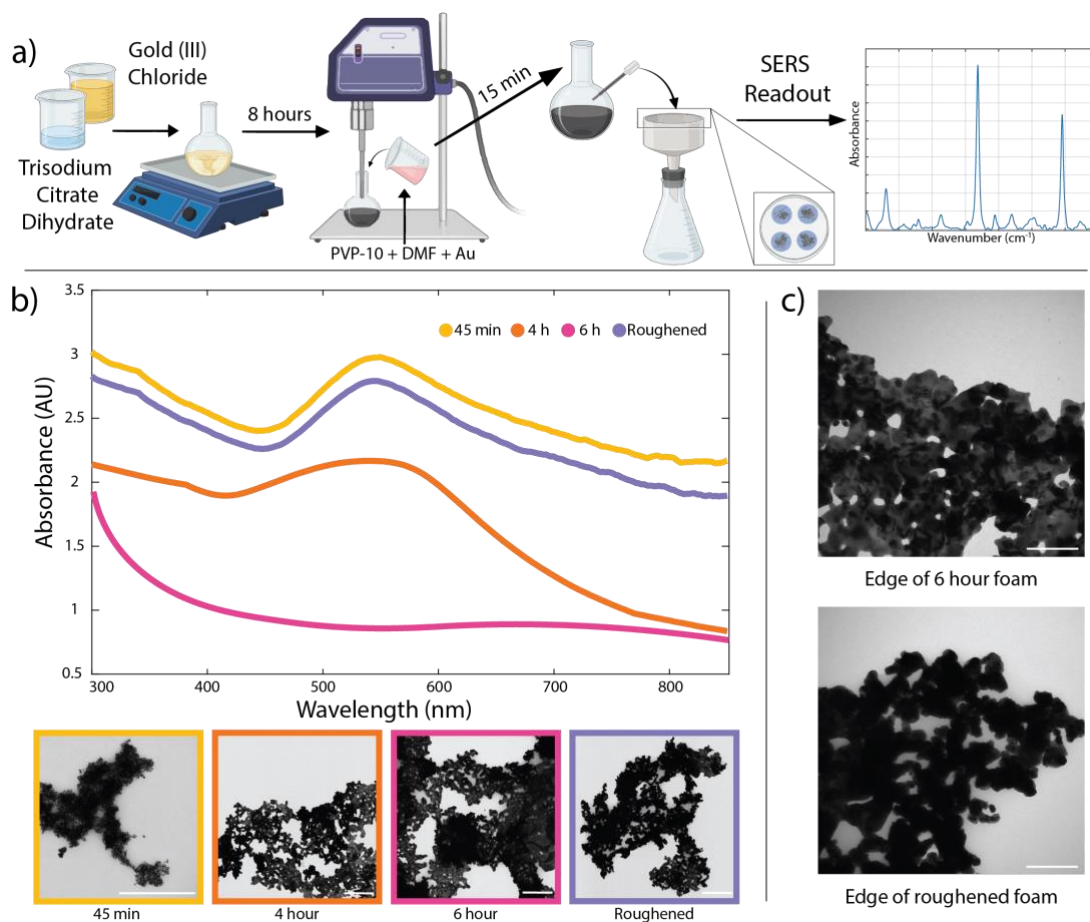
Figure 6.8. a) Overview of hierarchically tuned nanofoam synthesis and deposition onto filter paper. b) UV-vis spectra and corresponding TEM images of nanofoams at time points 45 min, 4 h, 6 h, and after chemical roughening. Scale bar is 500 nm for all images. c) TEM images of the edges of normal foams at the 6 h timepoint (top) and roughened nanofoams (bottom), scale bar 100 nm.

nanofeatures that give rise to the characteristic absorbance peak (520 nm) and gain more broad features indicative of elongated rods and wires. If allowed to continue reacting (~8 h) highly porous black foams precipitate out of the solution, which can be isolated by decanting the liquid and drying it under air.

While the emergence of microscale porosity during nanofoam evolution gives rise to useful and desired tortuosity, the nanoscale dimensions that enable SERS enhancement coarsen and thus are lost. To re-roughen the AuNFs, a solution of PVP-10 and gold (III) chloride in DMF was prepared and added to the AuNF seed solution at the 6 h mark (when foam networks were developed but not yet precipitated), and then probe ultrasonicated until the solution turned blue (~15 min). This color change indicates the presence of urchin-like features, forming a new material we refer to as roughened nanofoams (RNFs) (**Figure 6.1c**).
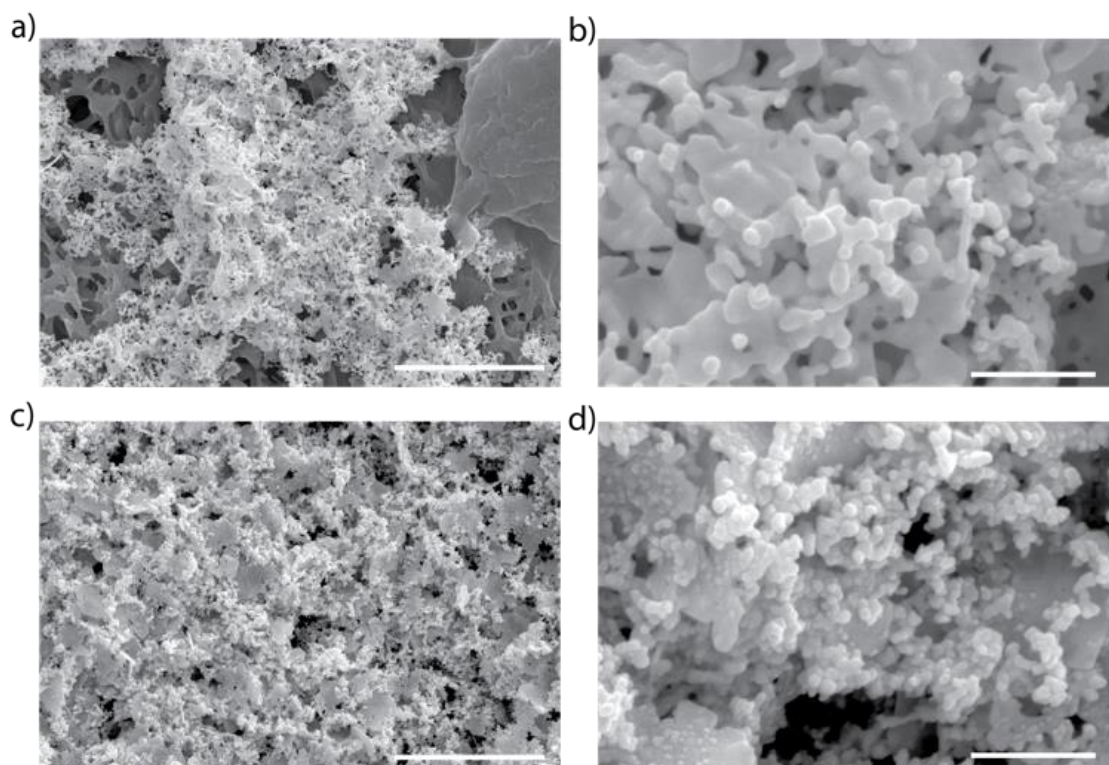
Figure 6.9. SEM images of (a,b) 6 h AuNFs and (c,d) RNFs at magnifications of 20kx (left panels, scale bar is 4 µm) and 100kx (right panels, scale bar is 500 nm). Following chemical roughening, the emergence of high density, ~20-50 nm nanoscale features is apparent.

6.3 Integration of nanofoams into filters and raster scanning for surface enhancement testing

AuNFs or RNFs were each deposited dropwise onto filter paper to form a substrate of several packed layers of foams. Scanning electron microscopy (SEM) images indicate the emergence of clear nanoscale features on the foams (**Figure 6.2**), showing the effectiveness of our chemical roughening procedure. Further, we measured the reappearance of the AuNP absorbance peak using UV-VIS spectroscopy (**Figure 6.1b**) indicating that the smaller nanofeatures that give rise to SERS enhancement are once again ubiquitous throughout the substrate.

To examine this further, we compared the SERS activity of AuNFs with RNFs using the common reporter molecule 4-mercaptobenzoic acid (4-MBA).[297] Filters for each substrate were generated and incubated with a solution of 4-MBA. We chose 4-MBA as a Raman standard because of the well-characterized interaction of its terminal thiol group with gold surfaces, which provides a straightforward method to approximate the surface coverage of our substrates.[297] More than 100 SERS spectra collected across several spots on each filter were collected, averaged, and used to compute the SERS enhancement factor (EF) by using the equation:

$$EF = \frac{I_{SERS}}{N_{SERS}} \times \frac{N_{RS}}{I_{RS}}$$

where I_{SERS} is the SERS signal of a chosen frequency, I_{RS} is the spontaneous Raman signal at that same frequency, N_{SERS} is the number of molecules excited in SERS and N_{RS} is the number of molecules excited in spontaneous Raman (i.e., 4-MBA measured under the identical optical conditions but without any foams).[297]

Figure 6.3 shows representative SERS spectra (**Figure 6.3a**) for the AuNFs and RNFs, where it is apparent that the RNFs are highly homogenous from spot to spot. Fig 3b-3e plot the SEM images and spectral maps at the chosen I_{SERS} frequency of 1077 cm^{-1} for the AuNF and RNF substrates, as

well as two commercially produced substrates (Ocean Optics and Hamamatsu). EFs were calculated

by estimating N_{SERS} according to the percentage of SERS active surface, using the topological surface

area by SEM analysis and the molecular surface area of 4-MBA. RNFs exhibited an impressive EF of

2.0×10^9 compared to AuNF EF of 7.3×10^8. Hamamatsu substrates had an EF of 4.0×10^9 and
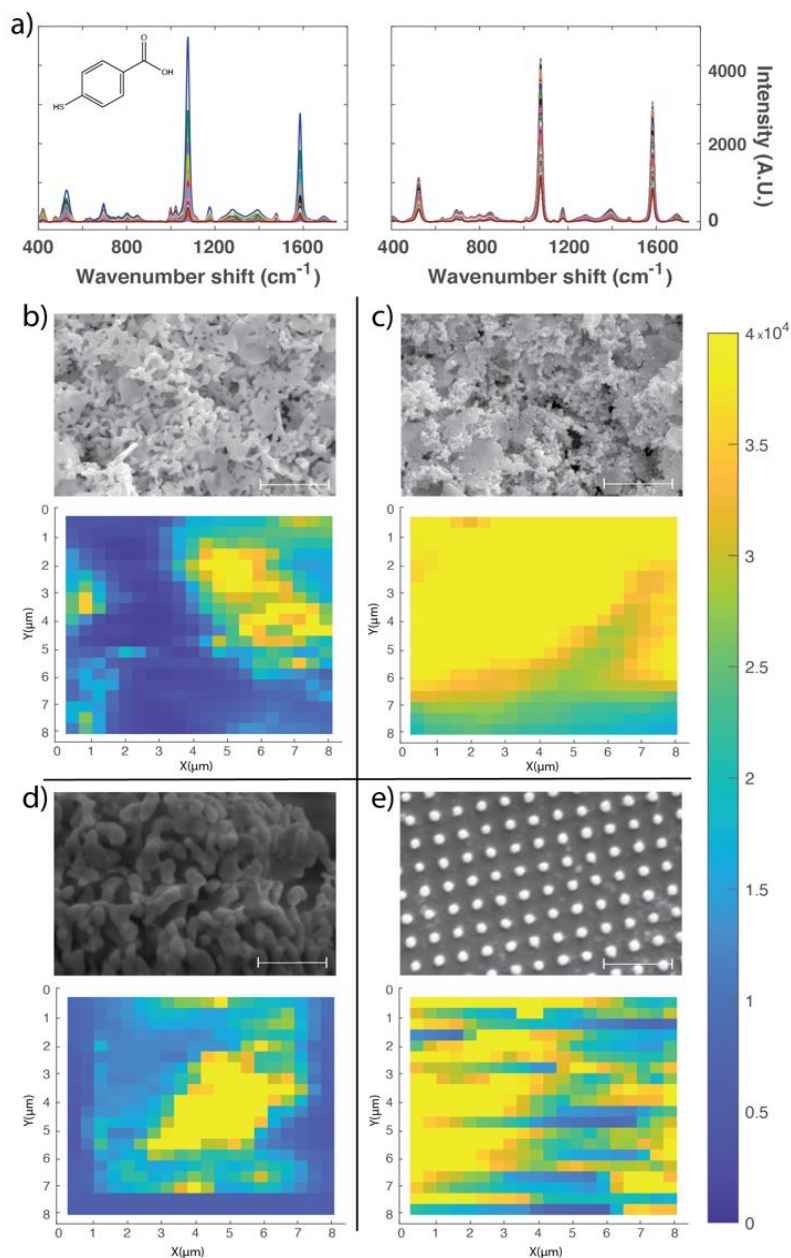
Figure 6.3. Raman scanning of various SERS substrates. Each raster scan represents an 8μm by 8μm area with a step size of 400 nm. a) Representative spectra of 4-MBA for AuNFs (left) and RNFs (right). SEM image and raster scan intensity at 1077cm^{-1} for b) AuNFs, c) chemically roughened RNFs, and commercial d) Ocean Optics and e) Hamamatsu SERS substrates. All scale bars are 1 μm.

Ocean Optics substrates an EF of 5.8×10^9. Hence, the RNFs show nearly an order of magnitude increase compared to the AuNF and comparable EF to lithographically fabricated commercial substrates. Rasterized Raman scanning reveals that the RNFs exhibit high spot-to-spot homogeneity of SERS signal across its surface (**Figure 6.3c**), besting commercial gold nanoparticle (**Figure 6.3d**) and lithographically fabricated substrates (**Figure 6.3e**).

6.4 Simulations of nanofoams show enhancement hotspots

Finite-difference time-domain (FDTD) simulation was performed to further evaluate the SERS EF provided by the AuNFs and RNFs.[298] The topological structure of the substrates as obtained by the SEM imaging (**Figure 6.4**) is used as the model for 3D construction. Local E field was calculated via FDTD simulation at the wavelength of 785 nm used in this work. EF was approximated as $\left(\frac{E}{E_0}\right)^4$ where E is the local electric field and E_0 is the input source electric field.[299] Since standard SEM is limited in resolving 3D morphological structure, an alternative topological model more closely aligned with the morphological nature of the AuNFs and RNFs was generated
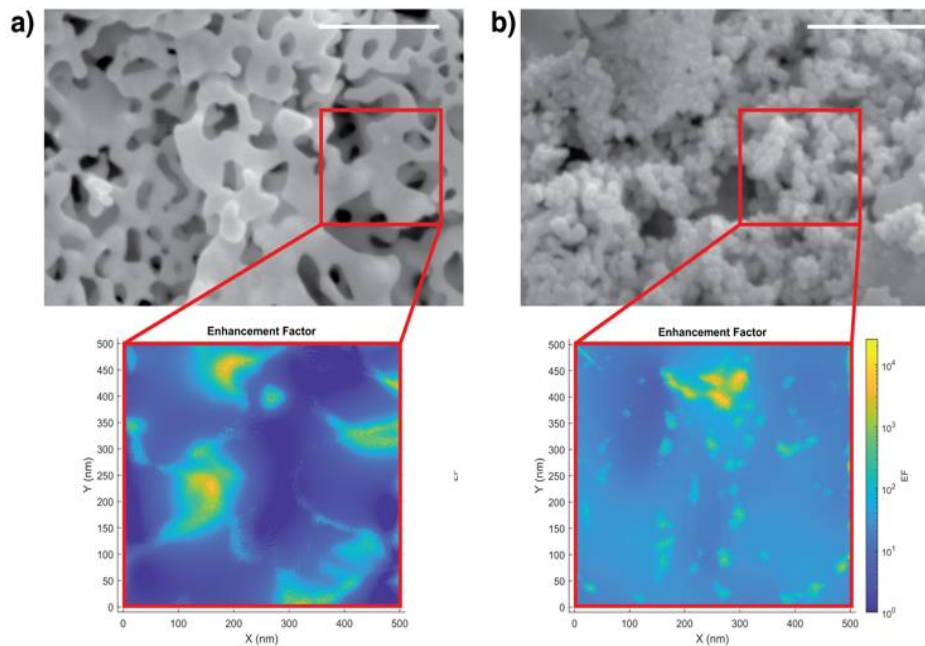
Figure 6.4. FTDT simulation of electromagnetic enhancement. Topological features extracted from SEM images of AuNFs (a) and RNFs (b) were used to model the local EF of the substrates. RNFs feature a homogenously increased EF throughout the substrate (insets represent roughly the optical focal area during scanning). Scale bar = 500 nm.

within a 500 nm x 500 nm simulation region, approximating the focal volume of optical measurement (see Supplemental Information). Here, RNFs exhibit an order of magnitude higher average enhancement factor compared to AuNFs, which agrees with the experimental results.

6.5 Supplemental Information
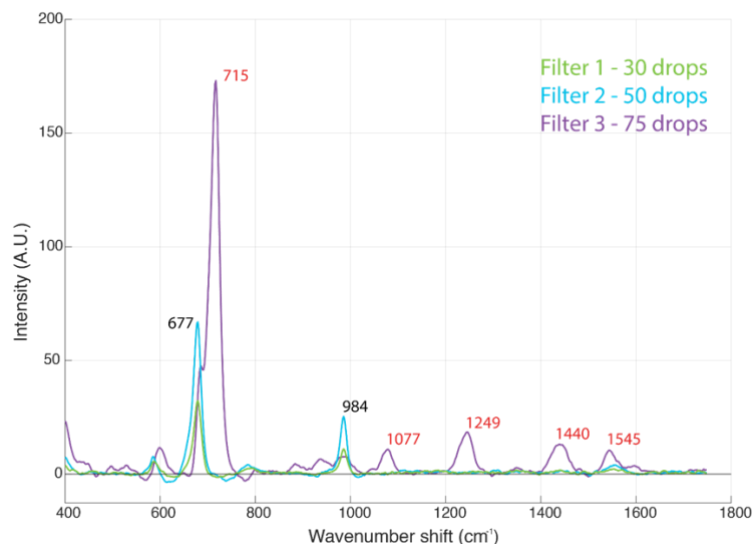
Figure S6.1: Nanofoam buildup on filter paper with 100 mM melamine dropped on to their surfaces. The green spectrum represents 30 drops of nanofoam solution, blue spectrum is 50 drops, and purple spectrum is 75 drops of nanofoams. After 75 drops multiple new peaks appear (noted in red text) as compared to the sub-75 drop filters (black text). These new peaks are indicative of melamine reporter molecule[300], demonstrating adequate buildup of the nanofoams on the filters.
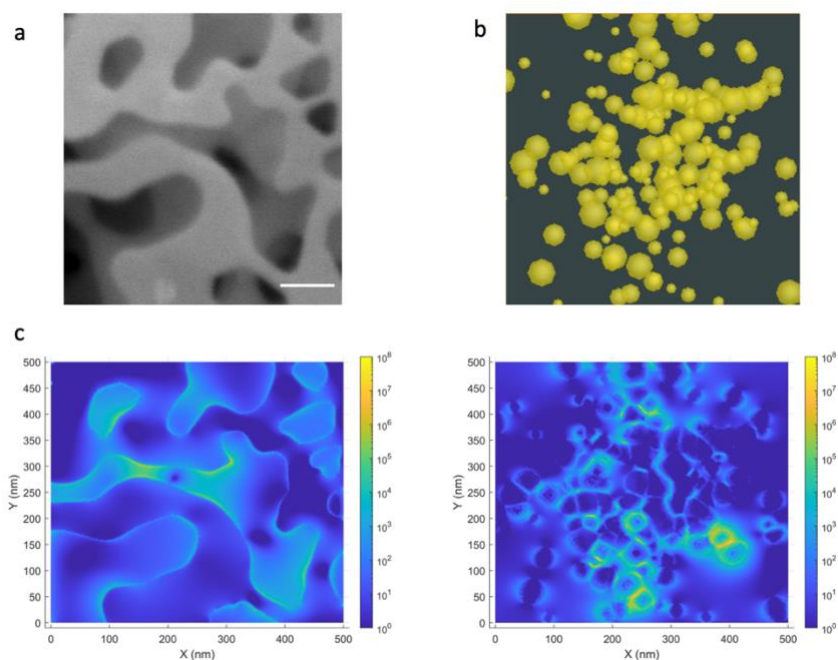
Figure S6.2: a. SEM image of the model AuNF structure. Scale bar = 100 nm. b. RNF structure modeled as a collection of 200 randomly distributed Au spheres ranging between 15 nm and 45 nm. C. EF distribution via FDTD simulation. Left, alternative AuNF structure. Right, alternative RNF structure.

6.6 Conclusions

In this study, we generated porous AuNFs and developed a straightforward chemical roughening approach to further improve the nanostructure with respect to SERS enhancement. The resulting RNFs provided an increased EF with sensitive chemical SERS readout while increasing the signal homogeneity and providing a larger number of consistent hotspots throughout the material. These inexpensive and easily fabricated RNFs are comparable in EF to more expensive and complex lithographically produced commercial SERS substrates. Our results are an exciting step in the direction of increasing the efficacy of SERS biosensing by generating simple, robust, and reproducible SERS materials that may be applied to sensing applications.

Chapter 7: Summary and Future Directions

Despite its immense value in preclinical work, clinical adoption of Raman as a diagnostic tool has lagged. The premise of this dissertation and a theme that permeates throughout the Carney Lab is the validation and development of features needed for a practical, implementable Raman platform for the clinic. The current clinical diagnostic standards offer information that is useful for monitoring of disease progression and treatment recommendations from clinicians, but they are hindered by some potentially unfixable issues such as high levels of specialized training, invasiveness, or the need for large physical space. They will remain in place as the gold standard until new techniques are validated and proven to overcome these limitations of long wait times for results, specialized training for interpretation of results, and cost of testing and equipment that often falls back on the patient.

We have shown that metabolites related to cancer can be identified in Raman spectra and further show a higher prevalence in cancer samples, validating that Raman is sensitive to the same metabolites found in GC-MS measurements. We further were able to provide robust evidence that our Raman platform can separate cancer from control in a plethora of biofluid sources. As an extension we provided evidence that novel data augmentation of stitching multiple biofluids together can increase diagnostic capabilities (on par with GC-MS) and furthermore provide a more comprehensive view of a patient's state of health. The results produced in this area are a powerful step in validating Raman as a robust diagnostic tool as well and developing a method to simultaneously have a more wholistic view of the disease state of an individual.

This dissertation also houses an immense amount of work done applying the extension of SERS. It is not surprising to note that chemical information provided by SERS has a high level of important features and reduces some of the limitations Raman currently has that have hindered its clinical adoption. SERS increases the sensitivity of the platform by quickly producing and analyzing chemical signatures and allows for ultra-fast readout of highly robust data that can be translated into

diagnostic information. We were able to develop a method for reducing the inherent heterogeneity seen with biological samples as well as reproducibly reveal chemical signals that directly correlated to cancer presence. We also revealed that important diagnostic features are present in the glycocalyx of isolated EVs, given that enzymatic cleavage of extraluminal domains yielded a significant loss of diagnostic sensitivity (i.e. ability to identify true positives). This will be a critical feature to examine in future work.

Another important theme found throughout this work was optimization of EV isolation and measurement parameters. To this end, we uncovered differences in populations of co-isolated biomolecules (residing in both the same size range and density range as our EVs) that changed based on the isolation method used. It is our recommendation to groups working on specific dosing studies to employ a protocol of UC followed by SEC to largely eliminate the lipoprotein contamination. Moreover, we devised multiple machine-learning approaches to decipher the cancer diagnostic potential of the SERS platform and found that regardless of the model used, our platform was sensitive enough to ignore the influence of these co-isolated biomolecules. This showed that we can tease out cancer-specific signals that are unaffected by additional co-isolates, strengthening the case to bring a SERS platform into the clinic. Biofluids are complex by nature and the time required to produce a pure population of EVs for analysis would negate the use of the technique from true clinical adoption. With this study specifically we showed that we can produce a high sensitivity of over 97%, indicating that we do not need particularly pure samples and proving again that our platform could have true clinical benefit.

One of the biggest hurdles SERS faces stems from the materials needed to produce the effect. Commercial substrates are too expensive for single use. SERS-active nanomaterials can be produced in larger quantities but are harder to control in terms of homogeneity of the readout signal. Our work in developing more useful SERS materials is a step in the direction of addressing the unmet need. The

nanofoam material provides good surface-area for biomolecule interaction and has the nanofeatures to assist in high SERS enhancement. They have a robust and consistent level of hotspots present throughout the material that match those of the microfabricated commercially available substrates, and they are quick and inexpensive to produce in comparison. Additionally, they have stable shelf lives of over 6 months and retain their high enhancement throughout that time. The results from this preliminary synthesis work provides an exciting step in increasing the efficacy of SERS biosensing by creating simple and reproducible SERS materials that can be integrated into point-of-use applications.

7.1 Future directions for validating Raman and SERS and a clinical biosensing tool

To truly take Raman into the clinic, more work will need to be done to validate the chemical signatures and diagnostic ability of the platform, largely by examining bigger cohorts of patients, as well as multi-site validation and verification studies to increase statical power and reduce variation in the system. Other components for adoption include miniaturization of the instrument components (while maintaining performance), automation of scanning and signal processing, and development of a robust signature library that can be used to glean useful specific diagnostic information indicative of mechanism of disease. If these issues can be addressed in a methodical manner, Raman could feasibly be used as the new standard of cancer diagnostics. It could even be expanded to encompass other diseases, eventually being used as a general health screening tool to assist in early-stage identification of many different disorders before they develop to a critical point where intervention yields sub-optimal results.

Automation of SERS is challenging, largely due to a lack of consensus as to the spectral features that broadly correlate with disease state. Projects that build on my work presented here are already underway in the lab, including testing for specific SERS signatures is underway in the hopes of identifying the particular spectral regions that indicate ideal regions for measurements. Our measurements now currently rely on an expert user manually probing random locations, taking

measurements, analyzing the data, and deeming it to be "SERS-active enough" prior to collection of data, a process which increases the time of operation as well as introduces bias into the measurements. Instead, classification of specific peaks could help ease these burdens. Once specific biological and chemical features are identified and correlated with each other scanning can be automated with a machine learning algorithm that is taught to seek out the specific features. While scanning, as the program detects the pre-selected peaks, it can stop and take the necessary measurements before continuing with the scanning. Identification of these specific peaks is no small task. To ensure conserved peaks are being identified, both cancerous and noncancerous samples are being tested across the multiple SERS substrates. Large surface area scans will be compared, and similar features will be identified in the hopes of recognizing some sort of useable distinct peaks as markers for "good" SERS locations for measurements. This work will help automate the scanning parameters, reducing the level of training needed for the person operating the eventual clinical platform.

In order to push Raman in the direction as a general health screening tool, work must be done to develop and build up a large library of robust clinical data. Resources needed to accomplish this goal would be access to a large number of biofluid sources (ranging from blood to saliva and other fluids) from multiple different hospitals from patients in different disease states (i.e., cancer, diabetes, cardiovascular disease, etc.) in order to test and capture inevitable heterogeneity from samples. Thousands of Raman measurements will be performed on the biofluid samples to produce powerful spectral standards correlated to the given disease. These can then be compiled into a database and used as reference database to further guide artificial intelligence-based methods for automation and screening.

7.2 Future directions for development of SERS materials

Another thrust for the continuation of the work outlined in this dissertation is the synthesis and development of more SERS-active materials. It is critical for clinical translation to produce reliable

and inexpensive materials that can be easily incorporated into the diagnostic platform. In terms of the nanofoams specifically, more work can be done to optimize the physical parameters and tune them to the sample. For instance, we found that the pore size in the foams is dependent on the ratio of gold to citrate. Creating foams with differing pore sizes could have strong implications for filtering capabilities and increase detection for specific biomolecule populations. Specifically relating to EVs, pores could be made to trap EVs while letting smaller particles through and blocking larger particles on the outside. The foams could then be interrogated by the Raman system for specific EV readout. This type of application would cut down significantly on isolation times and allow for fast and easy selection based on size.

Another step for a higher level of specificity could come from additional surface modifications of the materials. EVs (and other biomolecules of interest) have distinct surface proteins that can be targeted for pulldown. There are chemical techniques that allow for the functionalization of antibodies to gold materials, meaning the nanofoams and other products can be fitted with antibodies that target the specific surface proteins of interest. This could have impact in areas such as cancer diagnostics for HNC and OvCa that lack the early-stage biomarkers. Once cancerous Raman signals are validated, SERS materials can be outfitted with antibodies looking for those specific signatures and used as a method of targeted pulldown and subsequent biosensing for the unique cancer populations. To add another layer of complexity, biomolecules themselves can be tagged with a linker that contains its own distinct Raman tag (present in higher wavenumbers outside of the fingerprint region). This would also increase specificity by allowing selection of spots that have a biological signature as well as the discrete Raman tag peak.

7.3 Future work for extracellular vesicles

The results from work in this dissertation help highlight the potential diagnostic capabilities of EVs from clinical biofluids. However, there are some limitations of their use that need to be further

studied and improved upon. The high heterogeneity of the isolated population may not be an issue in some settings, but there is an increased acceptance that small EVs (typically around 30 nm) are more important in the context of cancer progression and monitoring. To that end, more work should be done to develop better ways of selecting very specific populations of these vesicles. Once the size selection becomes more specific, meticulous testing of the distinct populations will need to be done to address the biological and chemical differences between them. These results will then need to be correlated to other information such as their ability to report on the disease state.

Current work is being done to tag EVs with Raman-tagged antibodies. This can help with probing of specific populations that are selected based on surface features. For instance, HER2, CA125, and EPCAM are all biomarkers that have some relevance to OvCa. Developing antibodies with distinct Raman tags will allow us to flag the EVs expressing these proteins. While searching for spots to probe, the Raman tag can be used to show which spots are important for measurements and which can be ignored. A feature like this could also assist in the automation of scanning, reducing the burden on the user to locate these specific spots. The protocol for tagging the EVs with antibodies needs to be optimized to ensure a high enough number are successfully labelled before analysis. This work has further implications in multiplexing ability since each antibody can be associated with a different Raman tag and therefore show robust colocalization of different surface proteins once they are analyzed using the Raman platform.

References

[1]   D.L. Longo, L.Q.M.M. Chow, Head and Neck Cancer, N. Engl. J. Med. 382 (2020) 60–72. http://www.nejm.org/doi/10.1056/NEJMra1715715 (accessed May 10, 2021).

[2]   J.D. Cramer, B. Burtness, Q.T. Le, R.L. Ferris, The changing therapeutic landscape of head and neck cancer, Nat. Rev. Clin. Oncol. 2019 1611. 16 (2019) 669–683. https://doi.org/10.1038/s41571-019-0227-z.

[3]   F. Bray, J. Ferlay, I. Soerjomataram, R.L. Siegel, L.A. Torre, A. Jemal, Global cancer statistics 2018: GLOBOCAN estimates of incidence and mortality worldwide for 36 cancers in 185 countries, CA. Cancer J. Clin. 68 (2018) 394–424. https://doi.org/10.3322/caac.21492.

[4]   S. Lheureux, C. Gourley, I. Vergote, A.M. Oza, Epithelial ovarian cancer, Lancet. 393 (2019) 1240–1253. https://doi.org/10.1016/S0140-6736(18)32552-2.

[5]   L.A. Torre, B. Trabert, C.E. DeSantis, K.D. Miller, G. Samimi, C.D. Runowicz, M.M. Gaudet, A. Jemal, R.L. Siegel, Ovarian cancer statistics, 2018, CA. Cancer J. Clin. 68 (2018) 284–296. https://doi.org/10.3322/CAAC.21456.

[6]   Diagnosing Leukemia: Blood Tests, Biopsies & Other Test Results | CTCA, (n.d.). https://www.cancercenter.com/cancer-types/leukemia/diagnosis-and-detection (accessed June 15, 2022).

[7]   How Cancer Is Diagnosed - NCI, (n.d.). https://www.cancer.gov/about-cancer/diagnosis-staging/diagnosis (accessed June 15, 2022).

[8]   P. Charkhchi, C. Cybulski, J. Gronwald, F.O. Wong, S.A. Narod, M.R. Akbari, Ca125 and ovarian cancer: A comprehensive review, Cancers (Basel). 12 (2020) 1–29. https://doi.org/10.3390/CANCERS12123730.

[9]   S. Sakamoto, W. Putalun, S. Vimolmangkang, W. Phoolcharoen, Y. Shoyama, H. Tanaka, S. Morimoto, Enzyme-linked immunosorbent assay for the quantitative/qualitative analysis of plant secondary metabolites, J. Nat. Med. 72 (2018) 32. https://doi.org/10.1007/S11418-017-1144-Z.

[10]   R.B. Corcoran, B.A. Chabner, Application of Cell-free DNA Analysis to Cancer Treatment, N. Engl. J. Med. 379 (2018) 1754–1765. https://doi.org/10.1056/NEJMRA1706174/SUPPL_FILE/NEJMRA1706174_DISCLOSURES.PDF.

[11]   C. V Raman, F.R.S.[Plate, A new radiation*, Indian J. Phys. 2 (1928) 387–398.

[12]   T.H. Kauffmann, N. Kokanyan, M.D. Fontana, Use of Stokes and anti-Stokes Raman scattering for new applications, J. Raman Spectrosc. 50 (2019) 418–424. https://doi.org/10.1002/JRS.5523.

[13]   K. Eberhardt, C. Stiebing, C. Matthäus, M. Schmitt, J. Popp, Advantages and limitations of Raman spectroscopy for molecular diagnostics: an update, Https://Doi.Org/10.1586/14737159.2015.1036744. 15 (2015) 773–787. https://doi.org/10.1586/14737159.2015.1036744.

[14]   M. Fleischmann, P.J. Hendra, A.J. McQuillan, Raman spectra of pyridine adsorbed at a silver electrode, Chem. Phys. Lett. 26 (1974) 163–166. https://doi.org/10.1016/0009-2614(74)85388-1.

[15]   D.L. Jeanmaire, R.P. Van Duyne, Surface raman spectroelectrochemistry: Part I. Heterocyclic, aromatic, and aliphatic amines adsorbed on the anodized silver electrode, J. Electroanal. Chem. Interfacial Electrochem. 84 (1977) 1–20. https://doi.org/10.1016/S0022-0728(77)80224-6.

[16]   S. Schlücker, Surface-Enhanced Raman Spectroscopy: Concepts and Chemical Applications, Angew. Chemie Int. Ed. 53 (2014) 4756–4795. https://doi.org/10.1002/ANIE.201205748.

[17]   A. Campion, P. Kambhampati, Surface-enhanced Raman scattering, Chem. Soc. Rev. 27 (1998) 241–250. https://doi.org/10.1039/A827241Z.

[18]   S. Mohan, A. Chandrasekar, B. Subramanian, Surface Enhanced Raman Scattering Studies of Silver-gold Normal and Inverted Core-shell Nanostructures on their Efficiency of Detecting Molecules, Procedia Eng. 92 (2014) 19–25. https://doi.org/10.1016/J.PROENG.2013.10.005.

[19]   P.A. Mosier-Boss, Review of SERS substrates for chemical sensing, Nanomaterials. 7 (2017). https://doi.org/10.3390/NANO7060142.

[20]   B. Sharma, M. Fernanda Cardinal, S.L. Kleinman, N.G. Greeneltch, R.R. Frontiera, M.G. Blaber, G.C.

Schatz, R.P. Van Duyne, High-performance SERS substrates: Advances and challenges, MRS Bull. 38 (2013) 615–624. https://doi.org/10.1557/MRS.2013.161.

[21]   H. Ko, S. Singamaneni, V. V. Tsukruk, Nanostructured Surfaces and Assemblies as SERS Media, Small. 4 (2008) 1576–1599. https://doi.org/10.1002/SMLL.200800337.

[22]   S. Fateixa, H.I.S. Nogueira, T. Trindade, Hybrid nanostructures for SERS: materials development and chemical detection, Phys. Chem. Chem. Phys. 17 (2015) 21046–21071. https://doi.org/10.1039/C5CP01032B.

[23]   B. Sharma, R.R. Frontiera, A.I. Henry, E. Ringe, R.P. Van Duyne, SERS: Materials, applications, and the future, Mater. Today. 15 (2012) 16–25. https://doi.org/10.1016/S1369-7021(12)70017-2.

[24]   S. Schlücker, J. Homola, Sebastian Schlücker (Ed.): Surface enhanced Raman spectroscopy: analytical, biophysical and life science applications, Anal. Bioanal. Chem. 2011 4018. 401 (2011) 2329–2330. https://doi.org/10.1007/S00216-011-5321-8.

[25]   H. Yockell-Lelièvre, F. Lussier, J.F. Masson, Influence of the Particle Shape and Density of Self-Assembled Gold Nanoparticle Sensors on LSPR and SERS, J. Phys. Chem. C. 119 (2015) 28577–28585. https://doi.org/10.1021/ACS.JPCC.5B09570.

[26]   Z. Zhu, H. Meng, W. Liu, X. Liu, J. Gong, X. Qiu, L. Jiang, D. Wang, Z. Tang, Superstructures and SERS Properties of Gold Nanocrystals with Different Shapes, Angew. Chemie Int. Ed. 50 (2011) 1593–1596. https://doi.org/10.1002/ANIE.201005493.

[27]   Y. Yang, S. Matsubara, L. Xiong, T. Hayakawa, M. Nogami, Solvothermal synthesis of multiple shapes of silver nanoparticles and their SERS properties, J. Phys. Chem. C. 111 (2007) 9095–9104. https://doi.org/10.1021/JP068859B/SUPPL_FILE/JP068859BSI20070508_043435.PDF.

[28]   J. Kim, Y. Jang, N.J. Kim, H. Kim, G.C. Yi, Y. Shin, M.H. Kim, S. Yoon, Study of Chemical Enhancement Mechanism in Non-plasmonic Surface Enhanced Raman Spectroscopy (SERS), Front. Chem. 7 (2019) 582. https://doi.org/10.3389/FCHEM.2019.00582/BIBTEX.

[29]   X. Yu, H. Cai, W. Zhang, X. Li, N. Pan, Y. Luo, X. Wang, J.G. Hou, Tuning chemical enhancement of SERS by controlling the chemical reduction of graphene oxide nanosheets, ACS Nano. 5 (2011) 952–958. https://doi.org/10.1021/NN102291J/SUPPL_FILE/NN102291J_SI_001.PDF.

[30]   X.X. Han, R.S. Rodriguez, C.L. Haynes, Y. Ozaki, B. Zhao, Surface-enhanced Raman spectroscopy, Nat. Rev. Methods Prim. 2022 11. 1 (2022) 1–17. https://doi.org/10.1038/s43586-021-00083-6.

[31]   A. Pollap, P. Świt, Recent Advances in Sandwich SERS Immunosensors for Cancer Detection, Int. J. Mol. Sci. 2022, Vol. 23, Page 4740. 23 (2022) 4740. https://doi.org/10.3390/IJMS23094740.

[32]   O. Guselnikova, H. Lim, H.-J. Kim, S.H. Kim, A. Gorbunova, M. Eguchi, P. Postnikov, T. Nakanishi, T. Asahi, J. Na, Y. Yamauchi, O. Guselnikova, M. Eguchi, Y. Yamauchi, A. Gorbunova, P. Postnikov, H. Lim, J. Na, S.H. Kim, H.-J. Kim, T. Nakanishi, T. Asahi, New Trends in Nanoarchitectured SERS Substrates: Nanospaces, 2D Materials, and Organic Heterostructures, Small. (2022) 2107182. https://doi.org/10.1002/SMLL.202107182.

[33]   M.L. Coluccio, G. Das, F. Mecarini, F. Gentile, A. Pujia, L. Bava, R. Tallerico, P. Candeloro, C. Liberale, F. De Angelis, E. Di Fabrizio, Silver-based surface enhanced Raman scattering (SERS) substrate fabrication using nanolithography and site selective electroless deposition, Microelectron. Eng. 86 (2009) 1085–1088. https://doi.org/10.1016/J.MEE.2008.12.061.

[34]   M. Green, F.M. Liu, SERS Substrates Fabricated by Island Lithography: The Silver/Pyridine System, J. Phys. Chem. B. 107 (2003) 13015–13021. https://doi.org/10.1021/JP030751Y/ASSET/IMAGES/MEDIUM/JP030751YE00009.GIF.

[35]   V. Suresh, L. Ding, A.B. Chew, F.L. Yap, Fabrication of Large-Area Flexible SERS Substrates by Nanoimprint Lithography, ACS Appl. Nano Mater. 1 (2018) 886–893. https://doi.org/10.1021/ACSANM.7B00295/ASSET/IMAGES/LARGE/AN-2017-00295K_0007.JPEG.

[36]   L. Mikac, M. Ivanda, M. Gotić, T. Mihelj, L. Horvat, Synthesis and characterization of silver colloidal nanoparticles with different coatings for SERS application, J. Nanoparticle Res. 16 (2014) 1–13. https://doi.org/10.1007/S11051-014-2748-9/FIGURES/9.

[37]   J. Xie, Q. Zhang, J.Y. Lee, D.I.C. Wang, The synthesis of SERS-active gold nanoflower tags for in vivo applications, ACS Nano. 2 (2008) 2473–2480.

https://doi.org/10.1021/NN800442Q/SUPPL_FILE/NN800442Q_SI_001.PDF.

[38] I. Nabiev, I. Chourpa, M. Manfait, Applications of Raman and surface-enhanced Raman scattering spectroscopy in medicine, J. Raman Spectrosc. 25 (1994) 13–23. https://doi.org/10.1002/JRS.1250250104.

[39] C. Krafft, Bioanalytical applications of Raman spectroscopy, Anal. Bioanal. Chem. 378 (2004) 60–62. https://doi.org/10.1007/S00216-003-2266-6/FIGURES/2.

[40] G. Fini, Applications of Raman spectroscopy to pharmacy, J. Raman Spectrosc. 35 (2004) 335–337. https://doi.org/10.1002/JRS.1161.

[41] S. Cîntǎ Pînzaru, I. Pavel, N. Leopold, W. Kiefer, Identification and characterization of pharmaceuticals using Raman and surface-enhanced Raman scattering, J. Raman Spectrosc. 35 (2004) 338–346. https://doi.org/10.1002/JRS.1153.

[42] S. Fortin, B. Song, C. Burbage, Quantifying and identifying microplastics in the effluent of advanced wastewater treatment systems using Raman microspectroscopy, Mar. Pollut. Bull. 149 (2019) 110579. https://doi.org/10.1016/J.MARPOLBUL.2019.110579.

[43] A. Ianoul, T. Coleman, S.A. Asher, UV resonance raman spectroscopic detection of nitrate and nitrite in wastewater treatment processes, Anal. Chem. 74 (2002) 1458–1461. https://doi.org/10.1021/AC010863Q/ASSET/IMAGES/LARGE/AC010863QF00006.JPEG.

[44] H. Tang, C. Zhu, G. Meng, N. Wu, Review—Surface-Enhanced Raman Scattering Sensors for Food Safety and Environmental Monitoring, J. Electrochem. Soc. 165 (2018) B3098–B3118. https://doi.org/10.1149/2.0161808JES/XML.

[45] D.W. Li, W.L. Zhai, Y.T. Li, Y.T. Long, Recent progress in surface enhanced Raman spectroscopy for the detection of environmental pollutants, Microchim. Acta. 181 (2014) 23–43. https://doi.org/10.1007/S00604-013-1115-3/FIGURES/10.

[46] J. Lin, J. Lin, Z. Huang, P. Lu, J. Wang, X. Wang, R. Chen, RAMAN SPECTROSCOPY OF HUMAN HEMOGLOBIN FOR DIABETES DETECTION, Http://Dx.Doi.Org/10.1142/S179354581350051X. 7 (2014). https://doi.org/10.1142/S179354581350051X.

[47] H.W. Han, X.L. Yan, R.X. Dong, G. Ban, K. Li, Analysis of serum from type II diabetes mellitus and diabetic complication using surface-enhanced Raman spectra (SERS), Appl. Phys. B 2008 944. 94 (2008) 667–672. https://doi.org/10.1007/S00340-008-3299-5.

[48] S. Mabbott, S.C. Fernandes, M. Schechinger, G.L. Cote, K. Faulds, C.R. Mace, D. Graham, Detection of cardiovascular disease associated miR-29a using paper-based microfluidics and surface enhanced Raman scattering, Analyst. 145 (2020) 983–991. https://doi.org/10.1039/C9AN01748H.

[49] A. Chaichi, A. Prasad, M. Ranjan Gartia, Raman Spectroscopy and Microscopy Applications in Cardiovascular Diseases: From Molecules to Organs, Biosens. 2018, Vol. 8, Page 107. 8 (2018) 107. https://doi.org/10.3390/BIOS8040107.

[50] C.D. Syme, E.W. Blanch, C. Holt, R. Jakes, M. Goedert, L. Hecht, L.D. Barron, A Raman optical activity study of rheomorphism in caseins, synucleins and tau, Eur. J. Biochem. 269 (2002) 148–156. https://doi.org/10.1046/J.0014-2956.2001.02633.X.

[51] D. Kurouski, R.P. Van Duyne, I.K. Lednev, Exploring the structure and formation mechanism of amyloid fibrils by Raman spectroscopy: a review, Analyst. 140 (2015) 4967–4980. https://doi.org/10.1039/C5AN00342C.

[52] T.D. Payne, A.S. Moody, A.L. Wood, P.A. Pimiento, J.C. Elliott, B. Sharma, Raman spectroscopy and neuroscience: from fundamental understanding to disease diagnostics and imaging, Analyst. 145 (2020) 3461–3480. https://doi.org/10.1039/D0AN00083C.

[53] T. Vo-Dinh, L.R. Allain, D.L. Stokes, Cancer gene detection using surface-enhanced Raman scattering (SERS), J. Raman Spectrosc. 33 (2002) 511–516. https://doi.org/10.1002/jrs.883.

[54] S. Feng, R. Chen, J. Lin, J. Pan, Y. Wu, Y. Li, J. Chen, H. Zeng, Gastric cancer detection based on blood plasma surface-enhanced Raman spectroscopy excited by polarized laser light, Biosens. Bioelectron. 26 (2011) 3167–3174. https://doi.org/10.1016/j.bios.2010.12.020.

[55] S. Feng, D. Lin, J. Lin, B. Li, Z. Huang, G. Chen, W. Zhang, L. Wang, J. Pan, R. Chen, H. Zeng, Blood plasma surface-enhanced Raman spectroscopy for non-invasive optical detection of cervical

cancer, Analyst. 138 (2013) 3967–3974. https://doi.org/10.1039/c3an36890d.

[56]   S. Feng, R. Chen, J. Lin, J. Pan, G. Chen, Y. Li, M. Cheng, Z. Huang, J. Chen, H. Zeng Haishan, Nasopharyngeal cancer detection based on blood plasma surface-enhanced Raman spectroscopy and multivariate analysis, Biosens. Bioelectron. 25 (2010) 2414–2419. https://doi.org/10.1016/j.bios.2010.03.033.

[57]   X. Wang, X. Qian, J.J. Beitler, Z.G. Chen, F.R. Khuri, M.M. Lewis, H.J.C. Shin, S. Nie, D.M. Shin, Detection of circulating tumor cells in human peripheral blood using surface-enhanced raman scattering nanoparticles, Cancer Res. 71 (2011) 1526–1532. https://doi.org/10.1158/0008-5472.CAN-10-3069.

[58]   X. Li, Spectral analysis of human saliva for detection of lung cancer using surface-enhanced Raman spectroscopy, J. Biomed. Opt. 17 (2012) 037003. https://doi.org/10.1117/1.jbo.17.3.037003.

[59]   V. Moisoiu, S.D. Iancu, A. Stefancu, T. Moisoiu, B. Pardini, M.P. Dragomir, N. Crisan, L. Avram, D. Crisan, I. Andras, D. Fodor, L.F. Leopold, C. Socaciu, Z. Bálint, C. Tomuleasa, F. Elec, N. Leopold, SERS liquid biopsy: An emerging tool for medical diagnosis, Colloids Surfaces B Biointerfaces. 208 (2021) 112064. https://doi.org/10.1016/J.COLSURFB.2021.112064.

[60]   L. Avram, A. Stefancu, D. Crisan, N. Leopold, V. Donca, E. Buzdugan, R. Craciun, D. Andras, I. Coman, Recent advances in surface-enhanced Raman spectroscopy based liquid biopsy for colorectal cancer (Review), Exp. Ther. Med. 20 (2020) 1–1. https://doi.org/10.3892/ETM.2020.9342.

[61]   Y. Zhang, X. Mi, X. Tan, R. Xiang, Recent Progress on Liquid Biopsy Analysis using Surface-Enhanced Raman Spectroscopy, Theranostics. 9 (2019). /pmc/articles/PMC6376192/ (accessed June 4, 2020).

[62]   C. Alix-Panabières, K. Pantel, Liquid Biopsy: From Discovery to Clinical Application, Cancer Discov. 11 (2021) 858–873. https://doi.org/10.1158/2159-8290.CD-20-1311.

[63]   G. Poulet, J. Massias, V. Taly, Liquid Biopsy: General Concepts, Acta Cytol. 63 (2019) 449–455. https://doi.org/10.1159/000499337.

[64]   M. Mathieu, L. Martin-Jaular, G. Lavieu, C. Théry, Specificities of secretion and uptake of exosomes and other extracellular vesicles for cell-to-cell communication, Nature Publishing Group, 2019. https://doi.org/10.1038/s41556-018-0250-9.

[65]   M. Yáñez-Mó, P.R.-M.R.M. Siljander, Z. Andreu, A. Bedina Zavec, F.E. Borràs, E.I. Buzas, K. Buzas, E. Casal, F. Cappello, J. Carvalho, E. Colás, A. Cordeiro-Da Silva, S. Fais, J.M. Falcon-Perez, I.M. Ghobrial, B. Giebel, M. Gimona, M. Graner, I. Gursel, M. Gursel, N.H.H.H. Heegaard, A. Hendrix, P. Kierulf, K. Kokubun, M. Kosanovic, V. Kralj-Iglic, E.-M.M. Krämer-Albers, S. Laitinen, C. Lässer, T. Lener, E. Ligeti, A. Linē, G. Lipps, A. Llorente, J. Lötvall, M. Manček-Keber, A. Marcilla, M. Mittelbrunn, I. Nazarenko, E.N.M. Nolte-'t Hoen, T.A. Nyman, L. O'Driscoll, M. Olivan, C. Oliveira, É. Pállinger, H.A. del Portillo, J. Reventós, M. Rigau, E. Rohde, M. Sammar, F. Sánchez-Madrid, N. Santarém, K. Schallmoser, M. Stampe Ostenfeld, W. Stoorvogel, R. Stukelj, S.G. Van Der Grein, M. Helena Vasconcelos, M.H.M.M. Wauben, O. De Wever, A.B. Zavec, F.E. Borràs, E.I. Buzas, K. Buzas, E. Casal, F. Cappello, J. Carvalho, E. Colás, A. Cordeiro-Da Silva, S. Fais, J.M. Falcon-Perez, I.M. Ghobrial, B. Giebel, M. Gimona, M. Graner, I. Gursel, M. Gursel, N.H.H.H. Heegaard, A. Hendrix, P. Kierulf, K. Kokubun, M. Kosanovic, V. Kralj-Iglic, E.-M.M. Krämer-Albers, S. Laitinen, C. Lässer, T. Lener, E. Ligeti, A. Line, G. Lipps, A. Llorente, J. Lötvall, M. Manček-Keber, A. Marcilla, M. Mittelbrunn, I. Nazarenko, E.N.M. Nolte-'t Hoen, T.A. Nyman, L. O'Driscoll, M. Olivan, C. Oliveira, É. Pállinger, H.A. del Portillo, J. Reventós, M. Rigau, E. Rohde, M. Sammar, F. Sánchez-Madrid, N. Santarém, K. Schallmoser, M.S. Ostenfeld, W. Stoorvogel, R. Stukelj, S.G. Van Der Grein, M. Helena Vasconcelos, M.H.M.M. Wauben, O. De Wever, A. Bedina Zavec, F.E. Borràs, E.I. Buzas, K. Buzas, E. Casal, F. Cappello, J. Carvalho, E. Colás, A. Cordeiro-Da Silva, S. Fais, J.M. Falcon-Perez, I.M. Ghobrial, B. Giebel, M. Gimona, M. Graner, I. Gursel, M. Gursel, N.H.H.H. Heegaard, A. Hendrix, P. Kierulf, K. Kokubun, M. Kosanovic, V. Kralj-Iglic, E.-M.M. Krämer-Albers, S. Laitinen, C. Lässer, T. Lener, E. Ligeti, A. Linē, G. Lipps, A. Llorente, J. Lötvall, M. Manček-Keber, A. Marcilla, M. Mittelbrunn, I. Nazarenko, E.N.M. Nolte-'t Hoen, T.A. Nyman, L. O'Driscoll, M. Olivan, C. Oliveira, É. Pállinger, H.A. del Portillo, J. Reventós, M. Rigau, E. Rohde, M. Sammar, F. Sánchez-Madrid, N. Santarém, K. Schallmoser, M. Stampe Ostenfeld, W. Stoorvogel, R.

Stukelj, S.G. Van Der Grein, M. Helena Vasconcelos, M.H.M.M. Wauben, O. De Wever, Biological properties of extracellular vesicles and their physiological functions, 4 (2015). https://www.tandfonline.com/doi/full/10.3402/jev.v4.27066 (accessed June 4, 2020).

[66] G.D. Kusuma, M. Barabadi, J.L. Tan, D.A.V. Morton, J.E. Frith, R. Lim, To protect and to preserve: Novel preservation strategies for extracellular vesicles, Front. Pharmacol. 9 (2018) 1199. https://doi.org/10.3389/FPHAR.2018.01199/BIBTEX.

[67] A. Bakhshian Nik, J.D. Hutcheson, E. Aikawa, Extracellular Vesicles As Mediators of Cardiovascular Calcification, Front. Cardiovasc. Med. 4 (2017) 78. https://doi.org/10.3389/FCVM.2017.00078/BIBTEX.

[68] A. Fleury, M.C. Martinez, S. Le Lay, Extracellular vesicles as therapeutic tools in cardiovascular diseases, Front. Immunol. 5 (2014) 370. https://doi.org/10.3389/FIMMU.2014.00370/BIBTEX.

[69] S. Fu, Y. Zhang, Y. Li, L. Luo, Y. Zhao, Y. Yao, Extracellular vesicles in cardiovascular diseases, Cell Death Discov. 2020 61. 6 (2020) 1–9. https://doi.org/10.1038/s41420-020-00305-y.

[70] J.L. Welton, S. Loveless, T. Stone, C. von Ruhland, N.P. Robertson, A. Clayton, Cerebrospinal fluid extracellular vesicle enrichment for protein biomarker discovery in neurological disease; multiple sclerosis, J. Extracell. Vesicles. 6 (2017). https://doi.org/10.1080/20013078.2017.1369805/SUPPL_FILE/ZJEV_A_1369805_SM9616.ZIP.

[71] C.D. Fowler, A.F. Hill, Extracellular Vesicles and Neurodegenerative Diseases, J. Neurosci. 39 (2019) 9269–9273. https://doi.org/10.1523/JNEUROSCI.0147-18.2019.

[72] B.D. Chan, W.Y. Wong, M.M.L. Lee, W.C.S. Cho, B.K. Yee, Y.W. Kwan, W.C.S. Tai, Exosomes in Inflammation and Inflammatory Disease, Proteomics. 19 (2019) 1800149. https://doi.org/10.1002/PMIC.201800149.

[73] E.I. Buzas, B. György, G. Nagy, A. Falus, S. Gay, Emerging role of extracellular vesicles in inflammatory diseases, Nat. Rev. Rheumatol. 2014 106. 10 (2014) 356–364. https://doi.org/10.1038/nrrheum.2014.19.

[74] M. Salih, R. Zietse, E.J. Hoorn, Urinary extracellular vesicles and the kidney: biomarkers and beyond, Am. J. Physiol. Physiol. 306 (2014) F1251–F1259. https://doi.org/10.1152/ajprenal.00128.2014.

[75] P.G. Moon, J.E. Lee, Y.E. Cho, S.J. Lee, J.H. Jung, Y.S. Chae, H.I. Bae, Y.B. Kim, I.S. Kim, H.Y. Park, M.C. Baek, Identification of developmental endothelial locus-1 on circulating extracellular vesicles as a novel biomarker for early breast cancer detection, Clin. Cancer Res. 22 (2016) 1757–1766. https://doi.org/10.1158/1078-0432.CCR-15-0654.

[76] M. Nawaz, F. Fatima, I. Nazarenko, K. Ekström, I. Murtaza, M. Anees, A. Sultan, L. Neder, G. Camussi, H. Valadi, J.A. Squire, T. Kislinger, Extracellular vesicles in ovarian cancer: applications to tumor biology, immunotherapy and biomarker discovery, Expert Rev. Proteomics. 13 (2016) 395–409. https://doi.org/10.1586/14789450.2016.1165613.

[77] L. Sadovska, J. Eglitis, A. Line, Extracellular vesicles as biomarkers and therapeutic targets in breast cancer, Anticancer Res. 35 (2015) 6379–6390.

[78] S. Klein-Scory, M.M. Tehrani, C. Eilert-Micus, K.A. Adamczyk, N. Wojtalewicz, M. Schnölzer, S.A. Hahn, W. Schmiegel, I. Schwarte-Waldhoff, New insights in the composition of extracellular vesicles from pancreatic cancer cells: implications for biomarkers and functions, Proteome Sci. 12 (2014) 50. https://doi.org/10.1186/s12953-014-0050-5.

[79] G. Szabo, F. Momen-Heravi, Extracellular vesicles in liver disease and potential as biomarkers and therapeutic targets, Nat. Rev. Gastroenterol. Hepatol. 14 (2017) 455–466. https://doi.org/10.1038/nrgastro.2017.71.

[80] J.S. Redzic, T.H. Ung, M.W. Graner, Glioblastoma extracellular vesicles: Reservoirs of potential biomarkers, Pharmgenomics. Pers. Med. 7 (2014) 65–77. https://doi.org/10.2147/PGPM.S39768.

[81] A. Hoshino, B. Costa-Silva, T.L. Shen, G. Rodrigues, A. Hashimoto, M. Tesic Mark, H. Molina, S. Kohsaka, A. Di Giannatale, S. Ceder, S. Singh, C. Williams, N. Soplop, K. Uryu, L. Pharmer, T. King, L. Bojmar, A.E. Davies, Y. Ararso, T. Zhang, H. Zhang, J. Hernandez, J.M. Weiss, V.D. Dumont-Cole, K. Kramer, L.H. Wexler, A. Narendran, G.K. Schwartz, J.H. Healey, P. Sandstrom, K. Jørgen Labori, E.H. Kure, P.M. Grandgenett, M.A. Hollingsworth, M. De Sousa, S. Kaur, M. Jain, K. Mallya, S.K. Batra, W.R. Jarnagin, M.S. Brady, O. Fodstad, V. Muller, K. Pantel, A.J. Minn, M.J. Bissell, B.A.

Garcia, Y. Kang, V.K. Rajasekhar, C.M. Ghajar, I. Matei, H. Peinado, J. Bromberg, D. Lyden, Tumour exosome integrins determine organotropic metastasis, 527 (2015) 329–335. https://doi.org/10.1038/nature15756.

[82]   A. Ang´, A. Bobrie, C. Théry, T. Théry, Exosomes and communication between tumours and the immune system: are all exosomes equal?, Biochem. Soc. Trans. 41 (2013) 263–267. https://doi.org/10.1042/BST20120245.

[83]   B.A. Aguado, G.G. Bushnell, S.S. Rao, J.S. Jeruss, L.D. Shea, Engineering the pre-metastatic niche, Nat. Biomed. Eng. 2017 16. 1 (2017) 1–12. https://doi.org/10.1038/s41551-017-0077.

[84]   M. Nawaz, N. Shah, B.R. Zanetti, M. Maugeri, R.N. Silvestre, F. Fatima, L. Neder, H. Valadi, Extracellular Vesicles and Matrix Remodeling Enzymes: The Emerging Roles in Extracellular Matrix Remodeling, Progression of Diseases and Tissue Repair, Cells 2018, Vol. 7, Page 167. 7 (2018) 167. https://doi.org/10.3390/CELLS7100167.

[85]   S.A. Melo, H. Sugimoto, J.T. O'Connell, N. Kato, A. Villanueva, A. Vidal, L. Qiu, E. Vitkin, L.T. Perelman, C.A. Melo, A. Lucci, C. Ivan, G.A. Calin, R. Kalluri, Cancer Exosomes Perform Cell-Independent MicroRNA Biogenesis and Promote Tumorigenesis, Cancer Cell. 26 (2014) 707–721. https://doi.org/10.1016/J.CCELL.2014.09.005.

[86]   C. Théry, K.W. Witwer, E. Aikawa, M.J. Alcaraz, J.D. Anderson, R. Andriantsitohaina, A. Antoniou, T. Arab, F. Archer, G.K. Atkin-Smith, D.C. Ayre, J.M. Bach, D. Bachurski, H. Baharvand, L. Balaj, S. Baldacchino, N.N. Bauer, A.A. Baxter, M. Bebawy, C. Beckham, A. Bedina Zavec, A. Benmoussa, A.C. Berardi, P. Bergese, E. Bielska, C. Blenkiron, S. Bobis-Wozowicz, E. Boilard, W. Boireau, A. Bongiovanni, F.E. Borràs, S. Bosch, C.M. Boulanger, X. Breakefield, A.M. Breglio, M. Brennan, D.R. Brigstock, A. Brisson, M.L.D. Broekman, J.F. Bromberg, P. Bryl-Górecka, S. Buch, A.H. Buck, D. Burger, S. Busatto, D. Buschmann, B. Bussolati, E.I. Buzás, J.B. Byrd, G. Camussi, D.R.F. Carter, S. Caruso, L.W. Chamley, Y.T. Chang, A.D. Chaudhuri, C. Chen, S. Chen, L. Cheng, A.R. Chin, A. Clayton, S.P. Clerici, A. Cocks, E. Cocucci, R.J. Coffey, A. Cordeiro-da-Silva, Y. Couch, F.A.W. Coumans, B. Coyle, R. Crescitelli, M.F. Criado, C. D'Souza-Schorey, S. Das, P. de Candia, E.F. De Santana, O. De Wever, H.A. del Portillo, T. Demaret, S. Deville, A. Devitt, B. Dhondt, D. Di Vizio, L.C. Dieterich, V. Dolo, A.P. Dominguez Rubio, M. Dominici, M.R. Dourado, T.A.P. Driedonks, F. V. Duarte, H.M. Duncan, R.M. Eichenberger, K. Ekström, S. EL Andaloussi, C. Elie-Caille, U. Erdbrügger, J.M. Falcón-Pérez, F. Fatima, J.E. Fish, M. Flores-Bellver, A. Försönits, A. Frelet-Barrand, F. Fricke, G. Fuhrmann, S. Gabrielsson, A. Gámez-Valero, C. Gardiner, K. Gärtner, R. Gaudin, Y.S. Gho, B. Giebel, C. Gilbert, M. Gimona, I. Giusti, D.C.I. Goberdhan, A. Görgens, S.M. Gorski, D.W. Greening, J.C. Gross, A. Gualerzi, G.N. Gupta, D. Gustafson, A. Handberg, R.A. Haraszti, P. Harrison, H. Hegyesi, A. Hendrix, A.F. Hill, F.H. Hochberg, K.F. Hoffmann, B. Holder, H. Holthofer, B. Hosseinkhani, G. Hu, Y. Huang, V. Huber, S. Hunt, A.G.E. Ibrahim, T. Ikezu, J.M. Inal, M. Isin, A. Ivanova, H.K. Jackson, S. Jacobsen, S.M. Jay, M. Jayachandran, G. Jenster, L. Jiang, S.M. Johnson, J.C. Jones, A. Jong, T. Jovanovic-Talisman, S. Jung, R. Kalluri, S. ichi Kano, S. Kaur, Y. Kawamura, E.T. Keller, D. Khamari, E. Khomyakova, A. Khvorova, P. Kierulf, K.P. Kim, T. Kislinger, M. Klingeborn, D.J. Klinke, M. Kornek, M.M. Kosanović, Á.F. Kovács, E.M. Krämer-Albers, S. Krasemann, M. Krause, I. V. Kurochkin, G.D. Kusuma, S. Kuypers, S. Laitinen, S.M. Langevin, L.R. Languino, J. Lannigan, C. Lässer, L.C. Laurent, G. Lavieu, E. Lázaro-Ibáñez, S. Le Lay, M.S. Lee, Y.X.F. Lee, D.S. Lemos, M. Lenassi, A. Leszczynska, I.T.S. Li, K. Liao, S.F. Libregts, E. Ligeti, R. Lim, S.K. Lim, A. Linē, K. Linnemannstöns, A. Llorente, C.A. Lombard, M.J. Lorenowicz, Á.M. Lörincz, J. Lötvall, J. Lovett, M.C. Lowry, X. Loyer, Q. Lu, B. Lukomska, T.R. Lunavat, S.L.N. Maas, H. Malhi, A. Marcilla, J. Mariani, J. Mariscal, E.S. Martens-Uzunova, L. Martin-Jaular, M.C. Martinez, V.R. Martins, M. Mathieu, S. Mathivanan, M. Maugeri, L.K. McGinnis, M.J. McVey, D.G. Meckes, K.L. Meehan, I. Mertens, V.R. Minciacchi, A. Möller, M. Møller Jørgensen, A. Morales-Kastresana, J. Morhayim, F. Mullier, M. Muraca, L. Musante, V. Mussack, D.C. Muth, K.H. Myburgh, T. Najrana, M. Nawaz, I. Nazarenko, P. Nejsum, C. Neri, T. Neri, R. Nieuwland, L. Nimrichter, J.P. Nolan, E.N.M. Nolte-'t Hoen, N. Noren Hooten, L. O'Driscoll, T. O'Grady, A. O'Loghlen, T. Ochiya, M. Olivier, A. Ortiz, L.A. Ortiz, X. Osteikoetxea, O. Ostegaard, M. Ostrowski, J. Park, D.M. Pegtel, H. Peinado, F. Perut, M.W. Pfaffl, D.G. Phinney, B.C.H. Pieters, R.C. Pink, D.S. Pisetsky, E.

Pogge von Strandmann, I. Polakovicova, I.K.H. Poon, B.H. Powell, I. Prada, L. Pulliam, P. Quesenberry, A. Radeghieri, R.L. Raffai, S. Raimondo, J. Rak, M.I. Ramirez, G. Raposo, M.S. Rayyan, N. Regev-Rudzki, F.L. Ricklefs, P.D. Robbins, D.D. Roberts, S.C. Rodrigues, E. Rohde, S. Rome, K.M.A. Rouschop, A. Rughetti, A.E. Russell, P. Saá, S. Sahoo, E. Salas-Huenuleo, C. Sánchez, J.A. Saugstad, M.J. Saul, R.M. Schiffelers, R. Schneider, T.H. Schøyen, A. Scott, E. Shahaj, S. Sharma, O. Shatnyeva, F. Shekari, G.V. Shelke, A.K. Shetty, K. Shiba, P.R.M. Siljander, A.M. Silva, A. Skowronek, O.L. Snyder, R.P. Soares, B.W. Sódar, C. Soekmadji, J. Sotillo, P.D. Stahl, W. Stoorvogel, S.L. Stott, E.F. Strasser, S. Swift, H. Tahara, M. Tewari, K. Timms, S. Tiwari, R. Tixeira, M. Tkach, W.S. Toh, R. Tomasini, A.C. Torrecilhas, J.P. Tosar, V. Toxavidis, L. Urbanelli, P. Vader, B.W.M. van Balkom, S.G. van der Grein, J. Van Deun, M.J.C. van Herwijnen, K. Van Keuren-Jensen, G. van Niel, M.E. van Royen, A.J. van Wijnen, M.H. Vasconcelos, I.J. Vechetti, T.D. Veit, L.J. Vella, É. Velot, F.J. Verweij, B. Vestad, J.L. Viñas, T. Visnovitz, K. V. Vukman, J. Wahlgren, D.C. Watson, M.H.M. Wauben, A. Weaver, J.P. Webber, V. Weber, A.M. Wehman, D.J. Weiss, J.A. Welsh, S. Wendt, A.M. Wheelock, Z. Wiener, L. Witte, J. Wolfram, A. Xagorari, P. Xander, J. Xu, X. Yan, M. Yáñez-Mó, H. Yin, Y. Yuana, V. Zappulli, J. Zarubova, V. Žėkas, J. ye Zhang, Z. Zhao, L. Zheng, A.R. Zheutlin, A.M. Zickler, P. Zimmermann, A.M. Zivkovic, D. Zocco, E.K. Zuba-Surma, Minimal information for studies of extracellular vesicles 2018 (MISEV2018): a position statement of the International Society for Extracellular Vesicles and update of the MISEV2014 guidelines, J. Extracell. Vesicles. 7 (2018) 1535750. https://doi.org/10.1080/20013078.2018.1535750.

[87]   T. Rojalin, B. Phong, H. Koster, R.P.R.P. Carney, Nanoplasmonic approaches for sensitive detection and molecular characterization of extracellular vesicles, Frontiers Media S.A., 2019. https://doi.org/10.3389/fchem.2019.00279.

[88]   R.J. Lobb, M. Becker, S. Wen Wen, C.S.F. Wong, A.P. Wiegmans, A. Leimgruber, A. Möller, Optimized exosome isolation protocol for cell culture supernatant and human plasma, J. Extracell. Vesicles. 4 (2015) 27031. https://doi.org/10.3402/jev.v4.27031.

[89]   F. Momen-Heravi, Isolation of Extracellular Vesicles by Ultracentrifugation, Methods Mol. Biol. 1660 (2017) 25–32. https://doi.org/10.1007/978-1-4939-7253-1_3.

[90]   A.N. Böing, E. van der Pol, A.E. Grootemaat, F.A.W. Coumans, A. Sturk, R. Nieuwland, Single-step isolation of extracellular vesicles by size-exclusion chromatography, J. Extracell. Vesicles. 3 (2014) 23430. https://doi.org/10.3402/jev.v3.23430.

[91]   T. Rojalin, H.J. Koster, J. Liu, R.R. Mizenko, D. Tran, S. Wachsmann-Hogiu, R.P. Carney, Hybrid Nanoplasmonic Porous Biomaterial Scaffold for Liquid Biopsy Diagnostics Using Extracellular Vesicles, ACS Sensors. (2020). https://doi.org/10.1021/acssensors.0c00953.

[92]   S. Stremersch, M. Marro, B. El Pinchasik, P. Baatsen, A. Hendrix, S.C. De Smedt, P. Loza-Alvarez, A.G. Skirtach, K. Raemdonck, K. Braeckmans, Identification of individual exosome-like vesicles by surface enhanced raman spectroscopy, Small. 12 (2016) 3292–3301. https://doi.org/10.1002/smll.201600393.

[93]   Z.J. Smith, C. Lee, T. Rojalin, R.P. Carney, S. Hazari, A. Knudson, K. Lam, H. Saari, E.L. Ibañez, T. Viitala, T. Laaksonen, M. Yliperttula, S. Wachsmann-Hogiu, Single exosome study reveals subpopulations distributed among cell lines with variability related to membrane content, J. Extracell. Vesicles. 4 (2015). https://doi.org/10.3402/jev.v4.28533.

[94]   K. Sivashanmugam, W.-L.L. Huang, C.-H.C.-C.C.C.H. Lin, J.-D. Der Liao, C.-H.C.-C.C.C.H. Lin, W.-C.C. Su, T.-C.C. Wen, Bimetallic nanoplasmonic gap-mode SERS substrate for lung normal and cancer-derived exosomes detection, J. Taiwan Inst. Chem. Eng. 80 (2017) 149–155. https://doi.org/10.1016/j.jtice.2017.09.026.

[95]   R.P. Carney, S. Hazari, T. Rojalin, A. Knudson, T. Gao, Y. Tang, R. Liu, T. Viitala, M. Yliperttula, K.S. Lam, Targeting Tumor-Associated Exosomes with Integrin-Binding Peptides, Adv. Biosyst. 1 (2017). https://doi.org/10.1002/adbi.201600038.

[96]   J.W. Chan, D. Motton, J.C. Rutledge, N.L. Keim, T. Huser, Raman Spectroscopic Analysis of Biochemical Changes in Individual Triglyceride-Rich Lipoproteins in the Pre- and Postprandial State, Anal. Chem. 77 (2005) 5870–5876. https://doi.org/10.1021/ac050692f.

[97]   J. Park, M. Hwang, B. Choi, H. Jeong, J. Jung, H.K. Kim, S. Hong, J. Park, Y. Choi, Exosome

Classification by Pattern Analysis of Surface-Enhanced Raman Spectroscopy Data for Lung Cancer Diagnosis, Anal. Chem. 89 (2017) 6695–6701. https://doi.org/10.1021/acs.analchem.7b00911.

[98] L. König, S. Kasimir-Bauer, A.K. Bittner, O. Hoffmann, B. Wagner, L.F. Santos Manvailer, R. Kimmig, P.A. Horn, V. Rebmann, Elevated levels of extracellular vesicles are associated with therapy failure and disease progression in breast cancer patients undergoing neoadjuvant chemotherapy, Oncoimmunology. 7 (2017) e1376153. https://doi.org/10.1080/2162402X.2017.1376153.

[99] D. Osti, M. Del Bene, G. Rappa, M. Santos, V. Matafora, C. Richichi, S. Faletti, G. V. Beznoussenko, A. Mironov, A. Bachi, L. Fornasari, D. Bongetta, P. Gaetani, F. DiMeco, A. Lorico, G. Pelicci, Clinical significance of extracellular vesicles in plasma from glioblastoma patients, Clin. Cancer Res. 25 (2019) 266–276. https://doi.org/10.1158/1078-0432.CCR-18-1941.

[100] D. Tannetta, G. Collett, M. Vatish, C. Redman, I. Sargent, Syncytiotrophoblast extracellular vesicles – Circulating biopsies reflecting placental health, Placenta. 52 (2017) 134–138. https://doi.org/10.1016/j.placenta.2016.11.008.

[101] M. Zhao, D. Mi, B.E. Ferdows, Y. Li, R. Wang, J. Li, D. Patel, N. Kong, S. Shi, W. Tao, State-of-the-art nanotechnologies for the detection, recovery, analysis and elimination of liquid biopsy components in cancer, Nano Today. 42 (2022) 101361. https://doi.org/10.1016/J.NANTOD.2021.101361.

[102] J. Plou, P.S. Valera, I. García, C.D.L. De Albuquerque, A. Carracedo, L.M. Liz-Marzán, Prospects of Surface-Enhanced Raman Spectroscopy for Biomarker Monitoring toward Precision Medicine, ACS Photonics. 9 (2022) 333–350. https://doi.org/10.1021/ACSPHOTONICS.1C01934/ASSET/IMAGES/LARGE/PH1C01934_0007.JPEG.

[103] C. Fan, N. Zhao, K. Cui, G. Chen, Y. Chen, W. Wu, Q. Li, Y. Cui, R. Li, Z. Xiao, Ultrasensitive Exosome Detection by Modularized SERS Labeling for Postoperative Recurrence Surveillance, ACS Sensors. 6 (2021) 3241. https://doi.org/10.1021/ACSSENSORS.1C00890/ASSET/IMAGES/LARGE/SE1C00890_0005.JPEG.

[104] O. Fiehn, Metabolomics by Gas Chromatography-Mass Spectrometry: Combined Targeted and Untargeted Profiling, Curr. Protoc. Mol. Biol. 114 (2016). https://doi.org/10.1002/0471142727.MB3004S114.

[105] O. Fiehn, G. Wohlgemuth, M. Scholz, T. Kind, D.Y. Lee, Y. Lu, S. Moon, B. Nikolau, Quality control for plant metabolomics: reporting MSI-compliant studies, Plant J. 53 (2008) 691–704. https://doi.org/10.1111/J.1365-313X.2007.03387.X.

[106] Z. Lai, H. Tsugawa, G. Wohlgemuth, S. Mehta, M. Mueller, Y. Zheng, A. Ogiwara, J. Meissen, M. Showalter, K. Takeuchi, T. Kind, P. Beal, M. Arita, O. Fiehn, Identifying metabolites by integrating metabolome databases with mass spectrometry cheminformatics, Nat. Methods. 15 (2018) 53–56. https://doi.org/10.1038/NMETH.4512.

[107] Z.M. Zhang, S. Chen, Y.Z. Liang, Baseline correction using adaptive iteratively reweighted penalized least squares, Analyst. 135 (2010) 1138–1146. https://doi.org/10.1039/b922045c.

[108] P.H.C. Eilers, A perfect smoother, Anal. Chem. 75 (2003) 3631–3636. https://doi.org/10.1021/ac034173t.

[109] G. Midekessa, K. Godakumara, J. Ord, J. Viil, F. Lättekivi, K. Dissanayake, S. Kopanchuk, A. Rinken, A. Andronowska, S. Bhattacharjee, T. Rinken, A. Fazeli, Zeta Potential of Extracellular Vesicles: Toward Understanding the Attributes that Determine Colloidal Stability, ACS Omega. 5 (2020) 16701–16710. https://doi.org/10.1021/ACSOMEGA.0C01582.

[110] Early Detection and Treatment of Head & Neck Cancers, Early Detect. Treat. Head Neck Cancers. (2021). https://doi.org/10.1007/978-3-030-69852-2.

[111] J.C. Davis, L. Furstenthal, A.A. Desai, T. Norris, S. Sutaria, E. Fleming, P. Ma, The microeconomics of personalized medicine: today's challenge and tomorrow's promise, Nat. Rev. Drug Discov. 8 (2009) 279–286. https://doi.org/10.1038/NRD2825.

[112] K.H. Yu, M. Snyder, Omics profiling in precision oncology, Mol. Cell. Proteomics. 15 (2016) 2525–2536. https://doi.org/10.1074/mcp.O116.059253.

[113] E.A. Vucic, K.L. Thu, K. Robison, L.A. Rybaczyk, R. Chari, C.E. Alvarez, W.L. Lam, Translating

cancer "omics" to improved outcomes, Genome Res, 2012.
https://pubmed.ncbi.nlm.nih.gov/22301133/ (accessed May 12, 2021).

[114] E.G. Armitage, C. Barbas, Metabolomics in cancer biomarker discovery: Current trends and future perspectives, J. Pharm. Biomed. Anal. 87 (2014) 1–11. https://doi.org/10.1016/j.jpba.2013.08.041.

[115] R.L. McCreery, Raman Spectroscopy for Chemical Analysis , John Wiley & Sons, INC., New York, 2005.
https://books.google.com/books?hl=en&lr=&id=qY4MI0Zln1YC&oi=fnd&pg=PR5&dq=raman+spectroscopy&ots=ne-bwQ2-ZL&sig=jokmYSEgLe4UBPcCafgoIynu85I#v=onepage&q=raman spectroscopy&f=false (accessed May 25, 2021).

[116] D. Lazaro-Pacheco, A.M. Shaaban, S. Rehman, I. Rehman, Raman spectroscopy of breast cancer, Appl. Spectrosc. Rev. 55 (2020) 439–475. https://doi.org/10.1080/05704928.2019.1601105.

[117] G. Wang, R.J. Lipert, M. Jain, S. Kaur, S. Chakraboty, M.P. Torres, S.K. Batra, R.E. Brand, M.D. Porter, Detection of the potential pancreatic cancer marker MUC4 in serum using surface-enhanced Raman scattering, 83 (2011) 2554–2561. https://pubs.acs.org/sharingguidelines (accessed May 25, 2021).

[118] H. Lui, J. Zhao, D. McLean, H. Zeng, Real-time raman spectroscopy for in vivo skin cancer diagnosis, Cancer Res. 72 (2012) 2491–2500. https://doi.org/10.1158/0008-5472.CAN-11-4061.

[119] X. Li, T. Yang, S. Li, D. Wang, Y. Song, S. Zhang, Raman spectroscopy combined with principal component analysis and k nearest neighbour analysis for non-invasive detection of colon cancer, Laser Phys. 26 (2016) 035702. https://doi.org/10.1088/1054-660X/26/3/035702.

[120] M.S. Bergholt, W. Zheng, K. Lin, K.Y. Ho, M. Teh, K.G. Yeoh, J.B. Yan So, Z. Huang, In vivo diagnosis of gastric cancer using Raman endoscopy and ant colony optimization techniques, Int. J. Cancer. 128 (2011) 2673–2680. https://doi.org/10.1002/ijc.25618.

[121] Q. Zheng, J. Li, L. Yang, B. Zheng, J. Wang, N. Lv, J. Luo, F.L. Martin, D. Liu, J. He, Raman spectroscopy as a potential diagnostic tool to analyse biochemical alterations in lung cancer, Analyst. 145 (2020) 385–392. https://doi.org/10.1039/c9an02175b.

[122] S. Khan, R. Ullah, S. Javaid, S. Shahzad, H. Ali, M. Bilal, M. Saleem, M. Ahmed, Raman Spectroscopy Combined with Principal Component Analysis for Screening Nasopharyngeal Cancer in Human Blood Sera, Appl. Spectrosc. 71 (2017) 2497–2503. https://doi.org/10.1177/0003702817723928.

[123] S. Khan, R. Ullah, S. Shahzad, S. Javaid, A. Khan, Optical screening of nasopharyngeal cancer using Raman spectroscopy and support vector machine, Optik (Stuttg). 157 (2018) 565–570. https://doi.org/10.1016/j.ijleo.2017.11.097.

[124] A. Malik, A. Sahu, S.P. Singh, A. Deshmukh, P. Chaturvedi, D. Nair, S. Nair, C. Murali Krishna, In vivo Raman spectroscopy–assisted early identification of potential second primary/recurrences in oral cancers: An exploratory study, Head Neck. 39 (2017) 2216–2223. https://doi.org/10.1002/hed.24884.

[125] S. Holler, B. Haig, M.J. Donovan, M. Sobrero, B.A. Miles, A monolithic microsphere-fiber probe for spatially resolved Raman spectroscopy: Application to head and neck squamous cell carcinomas, Rev. Sci. Instrum. 89 (2018) 034301. https://doi.org/10.1063/1.5011771.

[126] M.-J.J. Jeng, M. Sharma, L. Sharma, T.-Y.Y. Chao, S.-F.F. Huang, L.-B.B. Chang, S.-L.L. Wu, L. Chow, Raman Spectroscopy Analysis for Optical Diagnosis of Oral Cancer Detection, J. Clin. Med. 8 (2019) 1313. /pmc/articles/PMC6780219/ (accessed January 5, 2021).

[127] S.A. Mian, C. Yorucu, M.S. Ullah, I.U. Rehman, H.E. Colley, Raman spectroscopy can discriminate between normal, dysplastic and cancerous oral mucosa: a tissue-engineering approach, J. Tissue Eng. Regen. Med. 11 (2017) 3253–3262. https://doi.org/10.1002/term.2234.

[128] S. Holler, E. Mansley, C. Mazzeo, M.J. Donovan, M. Sobrero, B.A. Miles, Raman spectroscopy of head and neck cancer: Separation of malignant and healthy tissue using signatures outside the "Fingerprint" region, Biosensors. 7 (2017) 20. https://doi.org/10.3390/bios7020020.

[129] J. Du, Y. Su, C. Qian, D. Yuan, K. Miao, D. Lee, A.H.C. Ng, R.S. Wijker, A. Ribas, R.D. Levine, J.R. Heath, L. Wei, Raman-guided subcellular pharmaco-metabolomics for metastatic melanoma cells, Nat. Commun. 11 (2020) 1–16. https://doi.org/10.1038/s41467-020-18376-x.

[130] A. Falamas, C.I. Faur, S. Ciupe, M. Chirila, H. Rotaru, M. Hedesiu, S. Cinta Pinzaru, Rapid and noninvasive diagnosis of oral and oropharyngeal cancer based on micro-Raman and FT-IR spectra of

saliva, Spectrochim. Acta - Part A Mol. Biomol. Spectrosc. 252 (2021) 119477. https://doi.org/10.1016/j.saa.2021.119477.

[131] Q. Zhan, Y.Y. Li, Y. Yuan, J. Liu, Y.Y. Li, The accuracy of Raman spectroscopy in the detection and diagnosis of oral cancer: A systematic review and meta-analysis, 2020. https://onlinelibrary.wiley.com/doi/full/10.1002/jrs.5940 (accessed May 10, 2021).

[132] H. Yan, M. Yu, J. Xia, L. Zhu, T. Zhang, Z. Zhu, Tongue squamous cell carcinoma discrimination with Raman spectroscopy and convolution neural networks, Vib. Spectrosc. 103 (2019) 102938. https://doi.org/10.1016/j.vibspec.2019.102938.

[133] S.F. El-Mashtoly, K. Gerwert, Diagnostics and Therapy Assessment Using Label-Free Raman Imaging, Anal. Chem. 94 (2022) 120–142. https://doi.org/10.1021/ACS.ANALCHEM.1C04483/ASSET/IMAGES/LARGE/AC1C04483_00 10.JPEG.

[134] C. Ciobanu, K.J.I. Ember, B.J. Nyíri, S. Rajan, V. Chauhan, F. Leblond, S. Murugkar, Potential of Raman Spectroscopy for Blood-Based Biopsy, IEEE Instrum. Meas. Mag. 25 (2022) 62–68. https://doi.org/10.1109/MIM.2022.9693451.

[135] M.Y. Sha, H. Xu, M.J. Natan, R. Cromer, Surface-Enhanced Raman Scattering Tags for Rapid and Homogeneous Detection of Circulating Tumor Cells in the Presence of Human Whole Blood, J. Am. Chem. Soc. 130 (2008) 17214–17215. https://doi.org/10.1021/ja804494m.

[136] M.L. Gillison, A.K. Chaturvedi, W.F. Anderson, C. Fakhry, Epidemiology of human papillomavirus-positive head and neck squamous cell carcinoma, J. Clin. Oncol. 33 (2015) 3235–3242. https://doi.org/10.1200/JCO.2015.61.6995.

[137] D.G. Pfister, S. Spencer, D.M. Brizel, B. Burtness, P.M. Busse, J.J. Caudell, A.J. Cmelak, A.D. Colevas, F. Dunphy, D.W. Eisele, J. Gilbert, M.L. Gillison, R.I. Haddad, B.H. Haughey, W.L. Hicks, Y.J. Hitchcock, A. Jimeno, M.S. Kies, W.M. Lydiatt, E. Maghami, R. Martins, T. McCaffrey, L.K. Mell, B.B. Mittal, H.A. Pinto, J.A. Ridge, C.P. Rodriguez, S. Samant, D.E. Schuller, J.P. Shah, R.S. Weber, G.T. Wolf, F. Worden, S.S. Yom, N.R. McMillian, M. Hughes, Head and neck cancers, version 2.2014, JNCCN J. Natl. Compr. Cancer Netw. 12 (2014) 1454–1487. https://doi.org/10.6004/jnccn.2014.0142.

[138] K. Malek, F. Ahmmed, D.P. Killeen, K.C. Gordon, S.J. Fraser-Miller, Rapid Quantitation of Adulterants in Premium Marine Oils by Raman and IR Spectroscopy: A Data Fusion Approach, Mol. 2022, Vol. 27, Page 4534. 27 (2022) 4534. https://doi.org/10.3390/MOLECULES27144534.

[139] E. Gibbons, R. Léveillé, K. Berlo, Data fusion of laser-induced breakdown and Raman spectroscopies: Enhancing clay mineral identification, Spectrochim. Acta Part B At. Spectrosc. 170 (2020) 105905. https://doi.org/10.1016/J.SAB.2020.105905.

[140] C. Robert, W. Jessep, J.J. Sutton, T.M. Hicks, M. Loeffen, M. Farouk, J.F. Ward, W.E. Bain, C.R. Craigie, S.J. Fraser-Miller, K.C. Gordon, Evaluating low- mid- and high-level fusion strategies for combining Raman and infrared spectroscopy for quality assessment of red meat, Food Chem. 361 (2021) 130154. https://doi.org/10.1016/J.FOODCHEM.2021.130154.

[141] C. Márquez, M.I. López, I. Ruisánchez, M.P. Callao, FT-Raman and NIR spectroscopy data fusion strategy for multivariate qualitative analysis of food fraud, Talanta. 161 (2016) 80–86. https://doi.org/10.1016/J.TALANTA.2016.08.003.

[142] O. Ryabchykov, J. Popp, T. Bocklitz, Fusion of MALDI spectrometric imaging and Raman spectroscopic data for the analysis of biological samples, Front. Chem. 6 (2018) 257. https://doi.org/10.3389/FCHEM.2018.00257/BIBTEX.

[143] X.H. Yang, Y. Jing, S. Wang, F. Ding, X.X. Zhang, S. Chen, L. Zhang, Q.G. Hu, Y.H. Ni, Integrated Non-targeted and Targeted Metabolomics Uncovers Amino Acid Markers of Oral Squamous Cell Carcinoma, Front. Oncol. 10 (2020) 426. https://doi.org/10.3389/FONC.2020.00426/BIBTEX.

[144] S.G. Musharraf, N. Shahid, S.M.A. Naqvi, M. Saleem, A.J. Siddiqui, A. Ali, Metabolite Profiling of Preneoplastic and Neoplastic Lesions of Oral Cavity Tissue Samples Revealed a Biomarker Pattern, Sci. Reports 2016 61. 6 (2016) 1–8. https://doi.org/10.1038/srep38985.

[145] A. Gualerzi, S. Niada, C. Giannasi, S. Picciolini, C. Morasso, R. Vanna, V. Rossella, M. Masserini, M. Bedoni, F. Ciceri, M.E. Bernardo, A.T. Brini, F. Gramatica, Raman spectroscopy uncovers

biochemical tissue-related features of extracellular vesicles from mesenchymal stromal cells, Sci. Rep. 7 (2017) 1–11. https://doi.org/10.1038/s41598-017-10448-1.

[146] M. Moreno, L. Raniero, E.Â.L. Arisawa, A.M. do Espírito Santo, E.A.P. dos Santos, R.A. Bitar, A.A. Martin, Raman spectroscopy study of breast disease, Theor. Chem. Acc. 125 (2010) 329–334. https://doi.org/10.1007/S00214-009-0698-6/FIGURES/5.

[147] L. Ståhle, S. Wold, Partial least squares analysis with cross-validation for the two-class problem: A Monte Carlo study, J. Chemom. 1 (1987) 185–196. https://doi.org/10.1002/CEM.1180010306.

[148] J. Kim, H.J. Park, J.H. Kim, B. Chang, H.K. Park, Label-free detection for a DNA methylation assay using Raman spectroscopy, Chin. Med. J. (Engl). 130 (2017) 1961–1967. https://doi.org/10.4103/0366-6999.211874.

[149] A. Bankapur, E. Zachariah, S. Chidangil, M. Valiathan, D. Mathur, Raman Tweezers Spectroscopy of Live, Single Red and White Blood Cells, PLoS One. 5 (2010) e10427. https://doi.org/10.1371/JOURNAL.PONE.0010427.

[150] A. Gualerzi, S.A.A. Kooijmans, S. Niada, S. Picciolini, A.T. Brini, G. Camussi, M. Bedoni, Raman spectroscopy as a quick tool to assess purity of extracellular vesicle preparations and predict their functionality, J. Extracell. Vesicles. 8 (2019). https://doi.org/10.1080/20013078.2019.1568780.

[151] L. Xue, B. Yan, Y. Li, Y. Tan, X. Luo, M. Wang, Surface-enhanced Raman spectroscopy of blood serum based on gold nanoparticles for tumor stages detection and histologic grades classification of oral squamous cell carcinoma, Int. J. Nanomedicine. 13 (2018) 4977–4986. https://doi.org/10.2147/IJN.S167996.

[152] L. Ma, Z. Zhang, X. Li, Non-invasive disease diagnosis using surface-enhanced Raman spectroscopy of urine and saliva, Https://Doi.Org/10.1080/05704928.2018.1562938. 55 (2019) 197–219. https://doi.org/10.1080/05704928.2018.1562938.

[153] D. Chaturvedi, S.A. Balaji, V.K. Bn, F. Ariese, S. Umapathy, A. Rangarajan, Different Phases of Breast Cancer Cells: Raman Study of Immortalized, Transformed, and Invasive Cells, Biosens. 2016, Vol. 6, Page 57. 6 (2016) 57. https://doi.org/10.3390/BIOS6040057.

[154] R. Galli, S. Tamosaityte, M. Koch, K.H. Sitoci-Ficici, R. Later, O. Uckermann, R. Beiermeister, M. Gelinsky, G. Schackert, M. Kirsch, E. Koch, G. Steiner, Raman-based imaging uncovers the effects of alginate hydrogel implants in spinal cord injury, Https://Doi.Org/10.1117/12.2183165. 9536 (2015) 114–121. https://doi.org/10.1117/12.2183165.

[155] E. Witkowska, D. Korsak, A. Kowalska, A. Janeczek, A. Kamińska, Strain-level typing and identification of bacteria – a novel approach for SERS active plasmonic nanostructures, Anal. Bioanal. Chem. 410 (2018) 5019–5031. https://doi.org/10.1007/s00216-018-1153-0.

[156] K. Sitarz, K. Czamara, S. Szostek, A. Kaczor, The impact of HPV infection on human glycogen and lipid metabolism – a review, Biochim. Biophys. Acta - Rev. Cancer. 1877 (2022) 188646. https://doi.org/10.1016/J.BBCAN.2021.188646.

[157] X. Chen, D. Yu, Metabolomics study of oral cancers, Metabolomics. 15 (2019) 22. https://doi.org/10.1007/s11306-019-1483-8.

[158] R. Kasiappan, P. Kamarajan, Y.L. Kapila, Metabolomics in head and neck cancer: A summary of findings, in: Transl. Syst. Med. Oral Dis., Elsevier, 2019: pp. 119–135. https://doi.org/10.1016/B978-0-12-813762-8.00005-0.

[159] R. Taware, K. Taunk, J.A.M. Pereira, R. Dhakne, N. Kannan, D. Soneji, J.S. Câmara, H.A. Nagarajaram, S. Rapole, Investigation of urinary volatomic alterations in head and neck cancer: a non-invasive approach towards diagnosis and prognosis, Metabolomics. 13 (2017) 111. https://doi.org/10.1007/s11306-017-1251-6.

[160] Ł. Boguszewicz, A. Bieleń, J.D. Jarczewski, M. Ciszek, A. Skorupa, K. Składowski, M. Sokół, Molecular response to induction chemotherapy and its correlation with treatment outcome in head and neck cancer patients by means of NMR-based metabolomics, BMC Cancer. 21 (2021) 410. https://doi.org/10.1186/s12885-021-08137-4.

[161] K. Jelonek, A. Krzywon, P. Jablonska, E.M. Slominska, R.T. Smolenski, J. Polanska, T. Rutkowski, J. Mrochem-Kwarciak, K. Skladowski, P. Widlak, Systemic effects of radiotherapy and concurrent chemo-radiotherapy in head and neck cancer patients—comparison of serum metabolome profiles,

Metabolites. 10 (2020) 60. https://doi.org/10.3390/metabo10020060.

[162] A. Wojakowska, A. Zebrowska, A. Skowronek, T. Rutkowski, K. Polanski, P. Widlak, L. Marczak, M. Pietrowska, Metabolic profiles of whole serum and serum-derived exosomes are different in head and neck cancer patients treated by radiotherapy, J. Pers. Med. 10 (2020) 1–14. https://doi.org/10.3390/jpm10040229.

[163] Boguszewicz, A. Bieleń, J. Mrochem-Kwarciak, A. Skorupa, M. Ciszek, A. Heyda, A. Wygoda, A. Kotylak, K. Składowski, M. Sokół, NMR-based metabolomics in real-time monitoring of treatment induced toxicity and cachexia in head and neck cancer: a method for early detection of high risk patients, Metabolomics. 15 (2019) 110. https://doi.org/10.1007/s11306-019-1576-4.

[164] M. Grimaldi, A. Palisi, G. Rossi, I. Stillitano, F. Faiella, P. Montoro, M. Rodriquez, R. Palladino, A.M. D'Ursi, R. Romano, Saliva of patients affected by salivary gland tumour: An NMR metabolomics analysis, J. Pharm. Biomed. Anal. 160 (2018) 436–442. https://doi.org/10.1016/j.jpba.2018.08.015.

[165] M. Sugimoto, Salivary metabolomics for cancer detection, Expert Rev. Proteomics. 17 (2020) 639–648. https://doi.org/10.1080/14789450.2020.1846524.

[166] J.Y. Wu, C. Yi, H.R. Chung, D.J. Wang, W.C. Chang, S.Y. Lee, C.T. Lin, Y.C. Yang, W.C.V. Yang, Potential biomarkers in saliva for oral squamous cell carcinoma, Oral Oncol. 46 (2010) 226–231. https://doi.org/10.1016/j.oraloncology.2010.01.007.

[167] D.J. Patil, C.B. More, Salivary metabolomics – A diagnostic and biologic signature for oral cancer, J. Oral Maxillofac. Surgery, Med. Pathol. (2021). https://doi.org/10.1016/j.ajoms.2021.02.003.

[168] A. Falamas, C.I. Faur, M. Baciut, H. Rotaru, M. Chirila, S. Cinta Pinzaru, M. Hedesiu, Raman Spectroscopic Characterization of Saliva for the Discrimination of Oral Squamous Cell Carcinoma, Anal. Lett. 54 (2021) 57–69. https://doi.org/10.1080/00032719.2020.1719129.

[169] G. Calado, I. Behl, A. Daniel, H.J. Byrne, F.M. Lyng, Raman spectroscopic analysis of saliva for the diagnosis of oral cancer: A systematic review, Transl. Biophotonics. 1 (2019) e201900001. https://doi.org/10.1002/tbio.201900001.

[170] S. TANAKA, M. MACHINO, S. AKITA, Y. YOKOTE, H. SAKAGAMI, Changes in Salivary Amino Acid Composition During Aging, In Vivo (Brooklyn). 24 (2010).

[171] I. Takeda, C. Stretch, P. Barnaby, K. Bhatnager, K. Rankin, H. Fub, A. Weljie, N. Jha, C. Slupsky, Understanding the human salivary metabolome, NMR Biomed. 22 (2009) 577–584. https://doi.org/10.1002/nbm.1369.

[172] N. Kawanishi, N. Hoshi, S. Masahiro, A. Enomoto, S. Ota, M. Kaneko, T. Soga, M. Tomita, K. Kimoto, Effects of inter-day and intra-day variation on salivary metabolomic profiles, Clin. Chim. Acta. 489 (2019) 41–48. https://doi.org/10.1016/j.cca.2018.11.030.

[173] M. Cooke, N. Leeves, C. White, Time profile of putrescine, cadaverine, indole and skatole in human saliva, Arch. Oral Biol. 48 (2003) 323–327. https://doi.org/10.1016/S0003-9969(03)00015-3.

[174] J. Ferlay, I. Soerjomataram, R. Dikshit, S. Eser, C. Mathers, M. Rebelo, D.M. Parkin, D. Forman, F. Bray, Cancer incidence and mortality worldwide: sources, methods and major patterns in GLOBOCAN 2012, Int. J. Cancer. 136 (2015) E359–E386. https://doi.org/10.1002/IJC.29210.

[175] J. Ferlay, M. Colombet, I. Soerjomataram, C. Mathers, D.M. Parkin, M. Piñeros, A. Znaor, F. Bray, Estimating the global cancer incidence and mortality in 2018: GLOBOCAN sources and methods, Int. J. Cancer. 144 (2019) 1941–1953. https://doi.org/10.1002/IJC.31937.

[176] E.G. Robertson, G. Baxter, Tumour seeding following percutaneous needle biopsy: the real story!, Clin. Radiol. 66 (2011) 1007–1014. https://doi.org/10.1016/J.CRAD.2011.05.012.

[177] M. Gerlinger, A.J. Rowan, S. Horswell, J. Larkin, D. Endesfelder, E. Gronroos, P. Martinez, N. Matthews, A. Stewart, P. Tarpey, I. Varela, B. Phillimore, S. Begum, N.Q. McDonald, A. Butler, D. Jones, K. Raine, C. Latimer, C.R. Santos, M. Nohadani, A.C. Eklund, B. Spencer-Dene, G. Clark, L. Pickering, G. Stamp, M. Gore, Z. Szallasi, J. Downward, P.A. Futreal, C. Swanton, Intratumor heterogeneity and branched evolution revealed by multiregion sequencing, N. Engl. J. Med. 366 (2012) 883–892. https://doi.org/10.1056/NEJMOA1113205.

[178] C. Alix-Panabieres, K. Pantel, Circulating tumor cells: liquid biopsy of cancer, Clin. Chem. 59 (2013) 110–118. https://doi.org/10.1373/CLINCHEM.2012.194258.

[179] E. Crowley, F. Di Nicolantonio, F. Loupakis, A. Bardelli, Liquid biopsy: monitoring cancer-genetics in

the blood, Nat. Rev. Clin. Oncol. 10 (2013) 472–484.
https://doi.org/10.1038/NRCLINONC.2013.110.

[180] G. De Rubis, S. Rajeev Krishnan, M. Bebawy, Liquid Biopsies in Cancer Diagnosis, Monitoring, and Prognosis, Trends Pharmacol. Sci. 40 (2019) 172–186. https://doi.org/10.1016/J.TIPS.2019.01.006.

[181] M.R. Speicher, K. Pantel, Tumor signatures in the blood, Nat. Biotechnol. 32 (2014) 441–443. https://doi.org/10.1038/NBT.2897.

[182] E. Heitzer, S. Perakis, J.B. Geigl, M.R. Speicher, The potential of liquid biopsies for the early detection of cancer, NPJ Precis. Oncol. 1 (2017). https://doi.org/10.1038/S41698-017-0039-5.

[183] G. Raposo, W. Stoorvogel, Extracellular vesicles: Exosomes, microvesicles, and friends, J. Cell Biol. 200 (2013) 373–383. https://doi.org/10.1083/jcb.201211138.

[184] S. Fais, L. O'Driscoll, F.E. Borras, E. Buzas, G. Camussi, F. Cappello, J. Carvalho, A. Cordeiro Da Silva, H. Del Portillo, S. El Andaloussi, T. Ficko Trček, R. Furlan, A. Hendrix, I. Gursel, V. Kralj-Iglic, B. Kaeffer, M. Kosanovic, M.E. Lekka, G. Lipps, M. Logozzi, A. Marcilla, M. Sammar, A. Llorente, I. Nazarenko, C. Oliveira, G. Pocsfalvi, L. Rajendran, G. Raposo, E. Rohde, P. Siljander, G. Van Niel, M.H. Vasconcelos, M. Yáñez-Mó, M.L. Yliperttula, N. Zarovni, A.B. Zavec, B. Giebel, Evidence-Based Clinical Use of Nanoscale Extracellular Vesicles in Nanomedicine, ACS Nano. 10 (2016) 3886–3899. https://doi.org/10.1021/acsnano.5b08015.

[185] A Raman spectroscopic study of glasses in the system CaO-MgO-SiO 2 | Semantic Scholar, (n.d.). https://www.semanticscholar.org/paper/A-Raman-spectroscopic-study-of-glasses-in-the-2-McMillan/ac33062bea9a2b8c3098df9b44fb87ec155de8dc (accessed June 23, 2022).

[186] P. Barcellos-de-Souza, V. Gori, F. Bambi, P. Chiarugi, Tumor microenvironment: bone marrow-mesenchymal stem cells as key players, Biochim. Biophys. Acta. 1836 (2013) 321–335. https://doi.org/10.1016/J.BBCAN.2013.10.004.

[187] H. Zhao, A. Achreja, E. Iessi, M. Logozzi, D. Mizzoni, R. Di Raimo, D. Nagrath, S. Fais, The key role of extracellular vesicles in the metastatic process, Biochim. Biophys. Acta - Rev. Cancer. 1869 (2018) 64–77. https://doi.org/10.1016/j.bbcan.2017.11.005.

[188] A. Becker, B.K. Thakur, J.M. Weiss, H.S. Kim, H. Peinado, D. Lyden, Extracellular Vesicles in Cancer: Cell-to-Cell Mediators of Metastasis, Cancer Cell. 30 (2016) 836–848. https://doi.org/10.1016/J.CCELL.2016.10.009.

[189] X. Li, X. Wang, The emerging roles and therapeutic potential of exosomes in epithelial ovarian cancer, Mol. Cancer. 16 (2017) 92. https://doi.org/10.1186/s12943-017-0659-y.

[190] M. He, J. Crow, M. Roth, Y. Zeng, A.K. Godwin, Integrated immunoisolation and protein analysis of circulating exosomes using microfluidic technology, Lab Chip. 14 (2014) 3773–3780. https://doi.org/10.1039/c4lc00662c.

[191] P.C. Lee, D. Meisel, Adsorption and surface-enhanced Raman of dyes on silver and gold sols, J. Phys. Chem. 86 (1982) 3391–3395. https://doi.org/10.1021/J100214A025/ASSET/J100214A025.FP.PNG_V03.

[192] S.G. Kruglik, F. Royo, J.M. Guigner, L. Palomo, O. Seksek, P.Y. Turpin, I. Tatischeff, J.M. Falcón-Pérez, Raman tweezers microspectroscopy of circa 100 nm extracellular vesicles, Nanoscale. 11 (2019) 1661–1679. https://doi.org/10.1039/C8NR04677H.

[193] C. Krafft, K. Wilhelm, A. Eremin, S. Nestel, N. von Bubnoff, W. Schultze-Seemann, J. Popp, I. Nazarenko, A specific spectral signature of serum and plasma-derived extracellular vesicles for cancer screening, Nanomedicine Nanotechnology, Biol. Med. 13 (2017) 835–841. https://doi.org/10.1016/j.nano.2016.11.016.

[194] I. Tatischeff, E. Larquet, J.M. Falcón-Pérez, P.Y. Turpin, S.G. Kruglik, Fast characterisation of cell-derived extracellular vesicles by nanoparticles tracking analysis, cryo-electron microscopy, and Raman tweezers microspectroscopy, J. Extracell. Vesicles. 1 (2012). https://doi.org/10.3402/jev.v1i0.19179.

[195] J. Langer, D.J. de Aberasturi, J. Aizpurua, R.A. Alvarez-Puebla, B. Auguié, J.J. Baumberg, G.C. Bazan, S.E.J. Bell, A. Boisen, A.G. Brolo, J. Choo, D. Cialla-May, V. Deckert, L. Fabris, K. Faulds, F. Javier García de Abajo, R. Goodacre, D. Graham, A.J. Haes, C.L. Haynes, C. Huck, T. Itoh, M. Käll, J. Kneipp, N.A. Kotov, H. Kuang, E.C. Le Ru, H.K. Lee, J.F. Li, X.Y. Ling, S.A. Maier, T. Mayerhöfer, M. Moskovits, K. Murakoshi, J.M. Nam, S. Nie, Y. Ozaki, I. Pastoriza-Santos, J. Perez-Juste, J. Popp,

A. Pucci, S. Reich, B. Ren, G.C. Schatz, T. Shegai, S. Schlücker, L.L. Tay, K. George Thomas, Z.Q. Tian, R.P. van Duyne, T. Vo-Dinh, Y. Wang, K.A. Willets, C. Xu, H. Xu, Y. Xu, Y.S. Yamamoto, B. Zhao, L.M. Liz-Marzán, Present and Future of Surface-Enhanced Raman Scattering, ACS Nano. 14 (2020) 28–117. https://doi.org/10.1021/ACSNANO.9B04224.

[196] J.A. Jackman, A. Rahim Ferhan, N.J. Cho, Nanoplasmonic sensors for biointerfacial science, Chem. Soc. Rev. 46 (2017) 3615–3660. https://doi.org/10.1039/C6CS00494F.

[197] A.R. Ferhan, J.A. Jackman, J.H. Park, N.J. Cho, Nanoplasmonic sensors for detecting circulating cancer biomarkers, Adv. Drug Deliv. Rev. 125 (2018) 48–77. https://doi.org/10.1016/J.ADDR.2017.12.004.

[198] L. Guerrini, R.A. Alvarez-Puebla, No Title, 2019. /pmc/articles/PMC6627759/ (accessed June 4, 2020).

[199] L. Polavarapu, L.M. Liz-Marzán, Towards low-cost flexible substrates for nanoplasmonic sensing, Phys. Chem. Chem. Phys. 15 (2013) 5288–5300. https://doi.org/10.1039/C2CP43642F.

[200] A. Korkmaz, M. Kenton, G. Aksin, M. Kahraman, S. Wachsmann-Hogiu, Inexpensive and Flexible SERS Substrates on Adhesive Tape Based on Biosilica Plasmonic Nanocomposites, ACS Appl. Nano Mater. 1 (2018) 5316–5326. https://doi.org/10.1021/acsanm.8b01336.

[201] S. John, Strong localization of photons in certain disordered dielectric superlattices, Phys. Rev. Lett. 58 (1987) 2486. https://doi.org/10.1103/PhysRevLett.58.2486.

[202] E. Yablonovitch, Inhibited spontaneous emission in solid-state physics and electronics, Phys. Rev. Lett. 58 (1987) 2059–2062. https://doi.org/10.1103/PHYSREVLETT.58.2059/FIGURE/1/THUMB.

[203] X. Xu, D. Hasan, L. Wang, S. Chakravarty, R.T. Chen, D.L. Fan, A.X. Wang, Guided-mode-resonance-coupled plasmonic-active SiO2 nanotubes for surface enhanced Raman spectroscopy, Appl. Phys. Lett. 100 (2012) 191114. https://doi.org/10.1063/1.4714710.

[204] C. Liu, Z. Wang, E. Li, Z. Liang, S. Chakravarty, X. Xu, A.X. Wang, R.T. Chen, D. Fan, Electrokinetic Manipulation Integrated Plasmonic-Photonic Hybrid Raman Nanosensors with Dually Enhanced Sensitivity, ACS Sensors. 2 (2017) 346–353. https://doi.org/10.1021/ACSSENSORS.6B00586/SUPPL_FILE/SE6B00586_SI_001.PDF.

[205] X. Kong, Y. Xi, P. Le Duff, X. Chong, E. Li, F. Ren, G.L. Rorrer, A.X. Wang, Detecting explosive molecules from nanoliter solution: A new paradigm of SERS sensing on hydrophilic photonic crystal biosilica, Biosens. Bioelectron. 88 (2017) 63–70. https://doi.org/10.1016/J.BIOS.2016.07.062.

[206] X. Kong, K. Squire, E. Li, P. Leduff, G.L. Rorrer, S. Tang, B. Chen, C.P. Mckay, R. Navarro-Gonzalez, A.X. Wang, Chemical and Biological Sensing Using Diatom Photonic Crystal Biosilica With In-Situ Growth Plasmonic Nanoparticles, IEEE Trans. Nanobioscience. 15 (2016) 828. https://doi.org/10.1109/TNB.2016.2636869.

[207] F. Ren, J. Campbell, G.L. Rorrer, A.X. Wang, Surface-Enhanced Raman Spectroscopy Sensors From Nanobiosilica With Self-Assembled Plasmonic Nanoparticles, IEEE J. Sel. Top. Quantum Electron. 20 (2014). https://doi.org/10.1109/JSTQE.2014.2301016.

[208] H. Im, H. Shao, Y. Il Park, V.M. Peterson, C.M. Castro, R. Weissleder, H. Lee, Label-free detection and molecular profiling of exosomes with a nano-plasmonic sensor, Nat. Biotechnol. 32 (2014) 490–495. https://doi.org/10.1038/NBT.2886.

[209] Y. Ma, L. Jiang, Y. Mei, R. Song, D. Tian, H. Huang, Colorimetric sensing strategy for mercury(ii) and melamine utilizing cysteamine-modified gold nanoparticles, Analyst. 138 (2013) 5338–5343. https://doi.org/10.1039/c3an00690e.

[210] A. Kudelski, W. Hill, Raman Study on the Structure of Cysteamine Monolayers on Silver, Langmuir. 15 (1999) 3162–3168. https://doi.org/10.1021/LA9811463.

[211] X. Jiang, M. Yang, Y. Meng, W. Jiang, J. Zhan, Cysteamine-modified silver nanoparticle aggregates for quantitative sers sensing of pentachlorophenol with a portable Raman spectrometer, ACS Appl. Mater. Interfaces. 5 (2013) 6902–6908. https://doi.org/10.1021/AM401718P/SUPPL_FILE/AM401718P_SI_001.PDF.

[212] P.L. Stiles, J.A. Dieringer, N.C. Shah, R.P. Van Duyne, Surface-Enhanced Raman Spectroscopy, Http://Dx.Doi.Org/10.1146/Annurev.Anchem.1.031207.112814. 1 (2008) 601–626.

https://doi.org/10.1146/ANNUREV.ANCHEM.1.031207.112814.

[213] K.A. Willets, Surface-enhanced Raman scattering (SERS) for probing internal cellular structure and dynamics, Anal. Bioanal. Chem. 394 (2009) 85–94. https://doi.org/10.1007/s00216-009-2682-3.

[214] P. Zhang, L. Wang, Y. Fang, D. Zheng, T. Lin, H. Wang, Label-Free Exosomal Detection and Classification in Rapid Discriminating Different Cancer Types Based on Specific Raman Phenotypes and Multivariate Statistical Analysis, Molecules. 24 (2019). https://doi.org/10.3390/MOLECULES24162947.

[215] H. Shin, H. Jeong, J. Park, S. Hong, Y. Choi, Correlation between Cancerous Exosomes and Protein Markers Based on Surface-Enhanced Raman Spectroscopy (SERS) and Principal Component Analysis (PCA), ACS Sensors. 3 (2018) 2637–2643. https://doi.org/10.1021/acssensors.8b01047.

[216] F. Royo, U. Cossío, A. Ruiz De Angulo, J. Llop, J.M. Falcon-Perez, Modification of the glycosylation of extracellular vesicles alters their biodistribution in mice, Nanoscale. 11 (2019) 1531–1537. https://doi.org/10.1039/C8NR03900C.

[217] M.J. Seo, G.W. Kim, P.V. Tsalu, S.W. Moon, J.W. Ha, Role of chemical interface damping for tuning chemical enhancement in resonance surface-enhanced Raman scattering of plasmonic gold nanorods, Nanoscale Horizons. 5 (2020) 345–349. https://doi.org/10.1039/C9NH00524B.

[218] J. Webber, A. Clayton, How pure are your vesicles?, J. Extracell. Vesicles. 2 (2013). https://doi.org/10.3402/jev.v2i0.19861.

[219] J.P. Mitchell, J. Court, M.D. Mason, Z. Tabi, A. Clayton, Increased exosome production from tumour cell cultures using the Integra CELLine Culture System, J. Immunol. Methods. 335 (2008) 98–105. https://doi.org/10.1016/J.JIM.2008.03.001.

[220] R. Mitra, G.L. O'Neil, I.C. Harding, M.J. Cheng, S.A. Mensah, E.E. Ebong, Glycocalyx in Atherosclerosis-Relevant Endothelium Function and as a Therapeutic Target, Curr. Atheroscler. Rep. 19 (2017). https://doi.org/10.1007/S11883-017-0691-9.

[221] Z. Varga, B. Fehér, D. Kitka, A. Wacha, A. Bóta, S. Berényi, V. Pipich, J.L. Fraikin, Size Measurement of Extracellular Vesicles and Synthetic Liposomes: The Impact of the Hydration Shell and the Protein Corona, Colloids Surfaces B Biointerfaces. 192 (2020) 111053. https://doi.org/10.1016/J.COLSURFB.2020.111053.

[222] B.J. Kennedy, S. Spaeth, M. Dickey, K.T. Carron, Determination of the Distance Dependence and Experimental Effects for Modified SERS Substrates Based on Self-Assembled Monolayers Formed Using Alkanethiols, J. Phys. Chem. B. 103 (1999) 3640–3646. https://doi.org/10.1021/JP984454I.

[223] C.R. Shurer, J.C.H. Kuo, L.D.M. Roberts, J.G. Gandhi, M.J. Colville, T.A. Enoki, H. Pan, J. Su, J.M. Noble, M.J. Hollander, J.P. O'Donnell, R. Yin, K. Pedram, L. Möckl, L.F. Kourkoutis, W.E. Moerner, C.R. Bertozzi, G.W. Feigenson, H.L. Reesink, M.J. Paszek, Physical Principles of Membrane Shape Regulation by the Glycocalyx, Cell. 177 (2019) 1757-1770.e21. https://doi.org/10.1016/J.CELL.2019.04.017.

[224] L. Paolini, F. Orizio, S. Busatto, A. Radeghieri, R. Bresciani, P. Bergese, E. Monti, Exosomes Secreted by HeLa Cells Shuttle on Their Surface the Plasma Membrane-Associated Sialidase NEU3, Biochemistry. 56 (2017) 6401–6408. https://doi.org/10.1021/ACS.BIOCHEM.7B00665.

[225] V. Muralidharan-Chari, J.W. Clancy, A. Sedgwick, C. D'Souza-Schorey, Microvesicles: mediators of extracellular communication during cancer progression, J. Cell Sci. 123 (2010) 1603–1611. https://doi.org/10.1242/JCS.064386.

[226] S. Zong, L. Wang, C. Chen, J. Lu, D. Zhu, Y. Zhang, Z. Wang, Y. Cui, Facile detection of tumor-derived exosomes using magnetic nanobeads and SERS nanoprobes, Anal. Methods. 8 (2016) 5001–5008. https://doi.org/10.1039/C6AY00406G.

[227] E. Trovato, V. Di Felice, R. Barone, Extracellular vesicles: Delivery vehicles of myokines, Front. Physiol. 10 (2019) 522. https://doi.org/10.3389/fphys.2019.00522.

[228] C. Frühbeis, S. Helmig, S. Tug, P. Simon, E.M. Krämer-Albers, Physical exercise induces rapid release of small extracellular vesicles into the circulation, J. Extracell. Vesicles. 4 (2015). https://doi.org/10.3402/JEV.V4.28239.

[229] R. Linares, S. Tan, C. Gounou, N. Arraud, A.R. Brisson, High-speed centrifugation induces aggregation of extracellular vesicles, J. Extracell. Vesicles. 4 (2015) 29509.

https://doi.org/10.3402/jev.v4.29509.

[230] S.S. Pinho, C.A. Reis, Glycosylation in cancer: mechanisms and clinical implications, Nat. Rev. Cancer 2015 159. 15 (2015) 540–555. https://doi.org/10.1038/nrc3982.

[231] T. Vagner, A. Chin, J. Mariscal, S. Bannykh, D.M. Engman, D. Di Vizio, Protein Composition Reflects Extracellular Vesicle Heterogeneity, Proteomics. 19 (2019) 1800167. https://doi.org/10.1002/pmic.201800167.

[232] L.J. Vella, A.F. Hill, L. Cheng, Focus on extracellular vesicles: Exosomes and their role in protein trafficking and biomarker potential in Alzheimer's and Parkinson's disease, Int. J. Mol. Sci. 17 (2016) 173. https://doi.org/10.3390/ijms17020173.

[233] A. Gámez-Valero, S.I. Lozano-Ramos, I. Bancu, R. Lauzurica-Valdemoros, F.E. Borràs, Urinary extracellular vesicles as source of biomarkers in kidney diseases, Front. Immunol. 6 (2015) 6. https://doi.org/10.3389/fimmu.2015.00006.

[234] T.A.P. Driedonks, E.N.M. Nolte-T'Hoen, Circulating Y-RNAs in extracellular vesicles and ribonucleoprotein complexes; Implications for the immune system, Front. Immunol. 10 (2019). https://doi.org/10.3389/fimmu.2018.03164.

[235] E.N. Hoen, T. Cremer, R.C. Gallo, L.B. Margolis, Extracellular vesicles and viruses: Are they close relatives?, Proc. Natl. Acad. Sci. U. S. A. 113 (2016) 9155–9161. https://doi.org/10.1073/pnas.1605146113.

[236] Z. Onódi, C. Pelyhe, C. Terézia Nagy, G.B. Brenner, L. Almási, Á. Kittel, M. Manček-Keber, P. Ferdinandy, E.I. Buzás, Z. Giricz, Isolation of High-Purity Extracellular Vesicles by the Combination of Iodixanol Density Gradient Ultracentrifugation and Bind-Elute Chromatography From Blood Plasma, Front. Physiol. 9 (2018). https://doi.org/10.3389/fphys.2018.01479.

[237] J.B. Simonsen, What are we looking at? Extracellular vesicles, lipoproteins, or both?, Circ. Res. 121 (2017) 920–922. https://doi.org/10.1161/CIRCRESAHA.117.311767.

[238] B.W. Sódar, Á. Kittel, K. Pálóczi, K. V. Vukman, X. Osteikoetxea, K. Szabó-Taylor, A. Németh, B. Sperlágh, T. Baranyai, Z. Giricz, Z. Wiener, L. Turiák, L. Drahos, É. Pállinger, K. Vékey, P. Ferdinandy, A. Falus, E.I. Buzás, Low-density lipoprotein mimics blood plasma-derived exosomes and microvesicles during isolation and detection, Sci. Rep. 6 (2016). https://doi.org/10.1038/srep24316.

[239] N. Karimi, A. Cvjetkovic, S.C. Jang, R. Crescitelli, M.A. Hosseinpour Feizi, R. Nieuwland, J. Lötvall, C. Lässer, Detailed analysis of the plasma extracellular vesicle proteome after separation from lipoproteins, Cell. Mol. Life Sci. 75 (2018) 2873–2886. https://doi.org/10.1007/s00018-018-2773-4.

[240] Y. Yuana, J. Levels, A. Grootemaat, A. Sturk, R. Nieuwland, Co-isolation of extracellular vesicles and high-density lipoproteins using density gradient ultracentrifugation, J. Extracell. Vesicles. 3 (2014) 23262. https://doi.org/10.3402/jev.v3.23262.

[241] P.D. Robbins, Extracellular vesicles and aging, Stem Cell Investig. 4 (2017) 98–98. https://doi.org/10.21037/sci.2017.12.03.

[242] E.H. Koritzinsky, J.M. Street, R.R. Chari, D.M. Glispie, T.R. Bellomo, A.M. Aponte, R.A. Star, P.S.T. Yuen, Circadian variation in the release of small extracellular vesicles can be normalized by vesicle number or TSG101, Am. J. Physiol. Physiol. 317 (2019) F1098–F1110. https://doi.org/10.1152/ajprenal.00568.2017.

[243] C. Frühbeis, S. Helmig, S. Tug, P. Simon, E.-M. Krämer-Albers, Physical exercise induces rapid release of small extracellular vesicles into the circulation, J. Extracell. Vesicles. 4 (2015) 28239. https://doi.org/10.3402/jev.v4.28239.

[244] Q. Fu, Y. Li, H. Jiang, Z. Shen, R. Gao, Y. He, Y. Liu, K. Xu, T. Yang, Hepatocytes derived extracellular vesicles from high-fat diet induced obese mice modulate genes expression and proliferation of islet β cells, Biochem. Biophys. Res. Commun. 516 (2019) 1159–1166. https://doi.org/10.1016/j.bbrc.2019.06.124.

[245] K.R. Feingold, C. Grunfeld, Introduction to Lipids and Lipoproteins, 2000. http://www.ncbi.nlm.nih.gov/pubmed/26247089 (accessed January 23, 2020).

[246] T. Baranyai, K. Herczeg, Z. Onódi, I. Voszka, K. Módos, N. Marton, G. Nagy, I. Mäger, M.J. Wood, S. El Andaloussi, Z. Pálinkás, V. Kumar, P. Nagy, Á. Kittel, E.I. Buzás, P. Ferdinandy, Z. Giricz,

Isolation of exosomes from blood plasma: Qualitative and quantitative comparison of ultracentrifugation and size exclusion chromatography methods, PLoS One. 10 (2015). https://doi.org/10.1371/journal.pone.0145686.

[247] A. Bobrie, M. Colombo, S. Krumeich, G. Raposo, C. Théry, Diverse subpopulations of vesicles secreted by different intracellular mechanisms are present in exosome preparations obtained by differential ultracentrifugation, J. Extracell. Vesicles. 1 (2012). https://doi.org/10.3402/jev.v1i0.18397.

[248] M.I. Zonneveld, A.R. Brisson, M.J.C. van Herwijnen, S. Tan, C.H.A. van de Lest, F.A. Redegeld, J. Garssen, M.H.M. Wauben, E.N.M. Nolte-'t Hoen, Recovery of extracellular vesicles from human breast milk is influenced by sample collection and vesicle isolation procedures, J. Extracell. Vesicles. 3 (2014) 24215. https://doi.org/10.3402/jev.v3.24215.

[249] A. Cvjetkovic, J. Lötvall, C. Lässer, The influence of rotor type and centrifugation time on the yield and purity of extracellular vesicles, J. Extracell. Vesicles. 3 (2014). https://doi.org/10.3402/jev.v3.23111.

[250] A. Gámez-Valero, M. Monguió-Tortajada, L. Carreras-Planella, M. Franquesa, K. Beyer, F.E. Borràs, Size-Exclusion Chromatography-based isolation minimally alters Extracellular Vesicles' characteristics compared to precipitating agents, Sci. Rep. 6 (2016). https://doi.org/10.1038/srep33641.

[251] E.A. Mol, M.-J. Goumans, P.A. Doevendans, J.P.G. Sluijter, P. Vader, Higher functionality of extracellular vesicles isolated using size-exclusion chromatography compared to ultracentrifugation, Nanomedicine Nanotechnology, Biol. Med. 13 (2017) 2061–2065. https://doi.org/10.1016/j.nano.2017.03.011.

[252] K. Kneipp, A.S. Haka, H. Kneipp, K. Badizadegan, N. Yoshizawa, C. Boone, K.E. Shafer-Peltier, J.T. Motz, R.R. Dasari, M.S. Feld, Surface-Enhanced Raman Spectroscopy in Single Living Cells Using Gold Nanoparticles, Appl. Spectrosc. 56 (2002) 150–154. https://doi.org/10.1366/0003702021954557.

[253] H. Shin, D. Seo, Y. Choi, Extracellular Vesicle Identification Using Label-Free Surface-Enhanced Raman Spectroscopy: Detection and Signal Analysis Strategies, Molecules. 25 (2020). https://doi.org/10.3390/molecules25215209.

[254] D. Mahl, J. Diendorf, W. Meyer-Zaika, M. Epple, Possibilities and limitations of different analytical methods for the size determination of a bimodal dispersion of metallic nanoparticles, Colloids Surfaces A Physicochem. Eng. Asp. 377 (2011) 386–392. https://doi.org/10.1016/j.colsurfa.2011.01.031.

[255] R.A. Dragovic, C. Gardiner, A.S. Brooks, D.S. Tannetta, D.J.P. Ferguson, P. Hole, B. Carr, C.W.G. Redman, A.L. Harris, P.J. Dobson, P. Harrison, I.L. Sargent, Sizing and phenotyping of cellular vesicles using Nanoparticle Tracking Analysis, Nanomedicine Nanotechnology, Biol. Med. 7 (2011) 780–788. https://doi.org/10.1016/j.nano.2011.04.003.

[256] N. Arraud, R. Linares, S. Tan, C. Gounou, J.-M. Pasquet, S. Mornet, A.R. Brisson, Extracellular vesicles from blood plasma: determination of their morphology, size, phenotype and concentration, J. Thromb. Haemost. 12 (2014) 614–627. https://doi.org/10.1111/jth.12554.

[257] Y. Yuana, R.I. Koning, M.E. Kuil, P.C.N. Rensen, A.J. Koster, R.M. Bertina, S. Osanto, Cryo-electron microscopy of extracellular vesicles in fresh plasma, J. Extracell. Vesicles. 2 (2013) 21494. https://doi.org/10.3402/jev.v2i0.21494.

[258] G.G. Daaboul, P. Gagni, L. Benussi, P. Bettotti, M. Ciani, M. Cretich, D.S. Freedman, R. Ghidoni, A.Y. Ozkumur, C. Piotto, D. Prosperi, B. Santini, M.S. Ünlü, M. Chiari, Digital Detection of Exosomes by Interferometric Imaging, Sci. Rep. 6 (2016). https://doi.org/10.1038/srep37246.

[259] A. Kudelski, W. Hill, Raman study on the structure of cysteamine monolayers on silver, Langmuir. 15 (1999) 3162–3168. https://doi.org/10.1021/la9811463.

[260] J.G. Boucher, T. Nguyen, D.L. Sparks, Lipoprotein electrostatic properties regulate hepatic lipase association and activity, Biochem. Cell Biol. 85 (2007) 696–708. https://doi.org/10.1139/O07-137.

[261] D.L. Sparks, M. Phillips, Quantitative measurement of lipoprotein surface charge by agarose gel electrophoresis., Undefined. (1992).

[262] A. Ricciardi, G. Piuri, M. Della Porta, S. Mazzucchelli, A. Bonizzi, M. Truffi, M. Sevieri, R. Allevi, F.

Corsi, R. Cazzola, C. Morasso, Raman spectroscopy characterization of the major classes of plasma lipoproteins, Vib. Spectrosc. 109 (2020) 103073. https://doi.org/10.1016/j.vibspec.2020.103073.

[263] H. Abdi, L.J. Williams, Principal component analysis, Wiley Interdiscip. Rev. Comput. Stat. 2 (2010) 433–459. https://doi.org/10.1002/wics.101.

[264] S. Mert, E. Özbek, A. Ötünçtemur, M. Çulha, Kidney tumor staging using surface-enhanced Raman scattering, J. Biomed. Opt. 20 (2015) 047002. https://doi.org/10.1117/1.jbo.20.4.047002.

[265] G. Lajos, D. Jancura, P. Miskovsky, J. V. García-Ramos, S. Sanchez-Cortes, Interaction of the Photosensitizer Hypericin with Low-Density Lipoproteins and Phosphatidylcholine: A Surface-Enhanced Raman Scattering and Surface-Enhanced Fluorescence Study, J. Phys. Chem. C. 113 (2009) 7147–7154. https://doi.org/10.1021/jp8112528.

[266] W. Lee, A. Nanou, L. Rikkert, F.A.W. Coumans, C. Otto, L.W.M.M. Terstappen, H.L. Offerhaus, Label-Free Prostate Cancer Detection by Characterization of Extracellular Vesicles Using Raman Spectroscopy, Anal. Chem. 90 (2018) 11290–11296. https://doi.org/10.1021/acs.analchem.8b01831.

[267] S. Lin, L. Quaroni, W.S. White, T. Cotton, G. Chumanov, Localization of carotenoids in plasma low-density lipoproteins studied by surface-enhanced resonance Raman spectroscopy, Biopolymers. 57 (2000) 249–256. https://doi.org/10.1002/1097-0282(2000)57:4<249::AID-BIP6>3.0.CO;2-1.

[268] M. Tang, L. Xia, D. Wei, S. Yan, C. Du, H.-L. Cui, Distinguishing Different Cancerous Human Cells by Raman Spectroscopy Based on Discriminant Analysis Methods, Appl. Sci. 7 (2017) 900. https://doi.org/10.3390/app7090900.

[269] S.J. Dixon, R.G. Brereton, Comparison of performance of five common classifiers represented as boundary methods: Euclidean Distance to Centroids, Linear Discriminant Analysis, Quadratic Discriminant Analysis, Learning Vector Quantization and Support Vector Machines, as dependent on data structure, Chemom. Intell. Lab. Syst. 95 (2009) 1–17. https://doi.org/10.1016/j.chemolab.2008.07.010.

[270] J.G. Kelly, J. Trevisan, A.D. Scott, P.L. Carmichael, H.M. Pollock, P.L. Martin-Hirsch, F.L. Martin, Biospectroscopy to metabolically profile biomolecular structure: A multistage approach linking computational analysis with biomarkers, J. Proteome Res. 10 (2011) 1437–1448. https://doi.org/10.1021/pr101067u.

[271] H. Zhang, A.C. Silva, W. Zhang, H. Rutigliano, A. Zhou, Raman Spectroscopy characterization extracellular vesicles from bovine placenta and peripheral blood mononuclear cells, PLoS One. 15 (2020) e0235214. https://doi.org/10.1371/journal.pone.0235214.

[272] G. Paramasivam, N. Kayambu, A.M. Rabel, A.K. Sundramoorthy, A. Sundaramurthy, Anisotropic noble metal nanoparticles: Synthesis, surface functionalization and applications in biosensing, bioimaging, drug delivery and theranostics, Acta Biomater. 49 (2017) 45–65. https://doi.org/10.1016/j.actbio.2016.11.066.

[273] A. Wittstock, J. Biener, M. Bäumer, Nanoporous gold: A new material for catalytic and sensor applications, Phys. Chem. Chem. Phys. 12 (2010) 12919–12930. https://doi.org/10.1039/c0cp00757a.

[274] K. Rong, L. Huang, H. Zhang, J. Zhai, Y. Fang, S. Dong, Electrochemical fabrication of nanoporous gold electrodes in a deep eutectic solvent for electrochemical detections, Chem. Commun. 54 (2018) 8853–8856. https://doi.org/10.1039/C8CC04454F.

[275] F. Dong, R.T. Koodali, H. Wang, W.K. Ho, Nanomaterials for environmental applications, J. Nanomater. 2014 (2014). https://doi.org/10.1155/2014/276467.

[276] J. Veselinovic, S. Almashtoub, E. Seker, Anomalous Trends in Nucleic Acid-Based Electrochemical Biosensors with Nanoporous Gold Electrodes, Anal. Chem. 91 (2019) 11923–11931. https://doi.org/10.1021/ACS.ANALCHEM.9B02686.

[277] F. Scaglione, E. Alladio, A. Damin, F. Turci, C. Baggiani, C. Giovannoli, S. Bordiga, L. Battezzati, P. Rizzi, Functionalized nanoporous gold as a new biosensor platform for ultra-low quantitative detection of human serum albumin, Sensors Actuators B Chem. 288 (2019) 460–468. https://doi.org/10.1016/J.SNB.2019.03.005.

[278] X.-Y. Lang, H.-Y. Fu, C. Hou, G.-F. Han, P. Yang, Y.-B. Liu, Q. Jiang, Nanoporous gold supported cobalt oxide microelectrodes as high-performance electrochemical biosensors, Nat. Commun. 2013 41. 4 (2013) 1–8. https://doi.org/10.1038/ncomms3169.

[279] H. Ke, A. Loaiza, A.G. Jimenez, D.F. Bahr, I. Mastorakos, A Multiscale Simulation Approach for the Mechanical Response of Copper/Nickel Nanofoams With Experimental Validation, J. Eng. Mater. Technol. 144 (2022). https://doi.org/10.1115/1.4051806.

[280] F.C. Durmus, J.M. Molina Jordá, J.M. MolinaJordá, Silver Foams with Hierarchical Porous Structures: From Manufacturing to Antibacterial Activity, ACS Appl. Mater. Interfaces. 13 (2021) 35865–35877. https://doi.org/10.1021/acsami.1c06057.

[281] B.C. Tappan, S.A.S. III, E. Dervishi, A.H. Mueller, B.L. Scott, C. Sheehan, E.P. Luther, J.P. Lichthardt, M.R. Dirmyer, Monolithic Nanoporous Gold Foams with Catalytic Activity for Chemical Vapor Deposition Growth of Carbon Nanostructures, ACS Appl. Mater. Interfaces. 13 (2020) 1204–1213. https://doi.org/10.1021/ACSAMI.0C17624.

[282] A. Jakhmola, M. Celentano, R. Vecchione, A. Manikas, E. Battista, V. Calcagno, P.A. Netti, Self-assembly of gold nanowire networks into gold foams: Production, ultrastructure and applications, Inorg. Chem. Front. 4 (2017) 1033–1041. https://doi.org/10.1039/c7qi00131b.

[283] V. Zielasek, B. Jürgens, C. Schulz, J. Biener, M.M. Biener, A. V. Hamza, M. Bäumer, Gold catalysts: Nanoporous gold foams, Angew. Chemie - Int. Ed. 45 (2006) 8241–8244. https://doi.org/10.1002/anie.200602484.

[284] S. Gao, H. Zhang, X. Wang, J. Yang, L. Zhou, C. Peng, D. Sun, M. Li, Unique gold sponges: biopolymer-assisted hydrothermal synthesis and potential applicationas surface-enhanced Raman scattering substrates, Nanotechnology. 16 (2005) 2530. https://doi.org/10.1088/0957-4484/16/11/012.

[285] Z. Z, L. H, Z. F, W. Y, G. Z, Z. L, L. J, Investigation of halide-induced aggregation of Au nanoparticles into spongelike gold, Langmuir. 30 (2014) 2648–2659. https://doi.org/10.1021/LA4046447.

[286] J. Malloy, A. Quintana, C.J. Jensen, K. Liu, Efficient and Robust Metallic Nanowire Foams for Deep Submicrometer Particulate Filtration, Nano Lett. 21 (2021) 2968–2974. https://doi.org/10.1021/ACS.NANOLETT.1C00050.

[287] D. Eustace, D. Graham, G. McNay, K. Faulds, W.E. Smith, Surface-Enhanced Raman Scattering (SERS) and Surface-Enhanced Resonance RamanScattering (SERRS): A Review of Applications, Appl. Spectrosc. Vol. 65, Issue 8, Pp. 825-837. 65 (2011) 825–837. https://doi.org/10.1366/11-06365.

[288] S.I.R.C. V Raman, Part 11.-the raman effect., (1929) 781–792.

[289] L. Guerrini, R.A. Alvarez-Puebla, Surface-Enhanced Raman Spectroscopy in Cancer Diagnosis, Prognosis and Monitoring, Cancers (Basel). 11 (2019) 625–633. https://doi.org/10.3390/CANCERS11060748.

[290] O. Lyandres, J.M. Yuen, N.C. Shah, R.P. VanDuyne, J.T. Walsh, M.R. Glucksberg, Progress toward an in vivo surface-enhanced Raman spectroscopy glucose sensor, Diabetes Technol. Ther. 10 (2008) 257–265. https://doi.org/10.1089/dia.2007.0288.

[291] X. Fu, Y. Wang, Y. Liu, H. Liu, L. Fu, J. Wen, J. Li, P. Wei, L. Chen, A graphene oxide/gold nanoparticle-based amplification method for SERS immunoassay of cardiac troponin I, Analyst. 144 (2019) 1582–1589. https://doi.org/10.1039/c8an02022a.

[292] A. Zengin, U. Tamer, T. Caykara, A SERS-based sandwich assay for ultrasensitive and selective detection of Alzheimer's tau protein, Biomacromolecules. 14 (2013) 3001–3009. https://doi.org/10.1021/bm400968x.

[293] F. Xu, W. Shang, G. Ma, Y. Zhu, M. Wu, Metal organic framework wrapped gold nanourchin assembled on filter membrane for fast and sensitive SERS analysis, Sensors Actuators B Chem. 326 (2021) 128968. https://doi.org/10.1016/J.SNB.2020.128968.

[294] Shuai He, Jefri Chua, E.K. Ming Tan, J.C. Yong Kah, Optimizing the SERS enhancement of a facile gold nanostar immobilized paper-based SERS substrate, RSC Adv. 7 (2017) 16264–16272. https://doi.org/10.1039/C6RA28450G.

[295] W.A. Tegegne, W.N. Su, A.B. Beyene, W.H. Huang, M.C. Tsai, B.J. Hwang, Flexible hydrophobic filter paper-based SERS substrate using silver nanocubes for sensitive and rapid detection of adenine, Microchem. J. 168 (2021) 106349. https://doi.org/10.1016/J.MICROC.2021.106349.

[296]   C. Wang, B. Liu, X. Dou, Silver nanotriangles-loaded filter paper for ultrasensitive SERS detection application benefited by interspacing of sharp edges, Sensors Actuators B Chem. 231 (2016) 357–364. https://doi.org/10.1016/J.SNB.2016.03.030.

[297]   S.E.J. Bell, G. Charron, E. Cortés, J. Kneipp, M.L. de la Chapelle, J. Langer, M. Procházka, V. Tran, S. Schlücker, Towards Reliable and Quantitative Surface-Enhanced Raman Scattering (SERS): From Key Parameters to Good Analytical Practice, Angew. Chemie - Int. Ed. 59 (2020) 5454–5462. https://doi.org/10.1002/anie.201908154.

[298]   H. Jung, M. Park, M. Kang, K.-H. Jeong, Silver nanoislands on cellulose fibers for chromatographic separation and ultrasensitive detection of small molecules, Light Sci. Appl. 2016 51. 5 (2016) e16009–e16009. https://doi.org/10.1038/lsa.2016.9.

[299]   E.C. Le Ru, P.G. Etchegoin, Rigorous justification of the |E|4 enhancement factor in Surface Enhanced Raman Spectroscopy, Chem. Phys. Lett. 423 (2006) 63–66. https://doi.org/10.1016/J.CPLETT.2006.03.042.

[300]   N.S. Chong, K.A. Smith, S. Setti, B.G. Ooi, Application of gold and silver colloidal nanoparticles for the surface-enhanced Raman spectrometric analysis of melamine and 4-aminobiphenyl, Int. J. Environ. Technol. Manag. 16 (2013) 3–20. https://doi.org/10.1504/IJETM.2013.050681.